Four wave mixing in III-V semiconductor photonic crystal cavities

Gabriel Marty

Thèse de doctorat

NNT: 2021UPASP045

université PARIS-SACLAY

Four wave mixing in III-V semiconductor photonic crystal cavities

Mélange à quatre ondes dans des cavités à cristaux photoniques en semiconducteur III-V

Thèse de doctorat de l'université Paris-Saclay

École doctorale n° 572, Ondes et Matière (EDOM)

Spécialité de doctorat: Physique

Unité de recherche: Université Paris-Saclay, CNRS, Centre de Nanosciences et de Nanotechnologies, 91120, Palaiseau, France

Référent: Faculté des sciences d'Orsay

Thèse présentée et soutenue à Paris-Saclay, le 29 juin 2021, par

Gabriel MARTY

Composition du jury:

Xavier CHECOURY	*Président du jury*
Professeur des Universités, Université Paris Saclay	
Philippe BOUCAUD	*Rapporteur et Examinateur*
Directeur de Recherche, CNRS-CRHEA	
Dario GERACE	*Rapporteur et Examinateur*
Professeur, Università di Pavia	
Christelle MONAT	*Examinateur*
Maîtresse de Conférences, Ecole Centrale Lyon	
Allard MOSK	*Examinateur*
Professeur, Universiteit Utrecht	

Direction de la thèse:

Alfredo DE ROSSI	*Directeur de thèse*
Ingénieur de recherche, Thales Research and Technology	
Fabrice RAINERI	*Co-directeur de thèse*
Maître de Conférences, Université de Paris	
Sylvain COMBRIE	*Co-encadrant*
Ingénieur de recherche, Thales Research and Technology	

A mes parents

Remerciements

Bien loin d'un travail solitaire, cette thèse fut une entreprise collective mêlant des expertises si diverses qu'une personne seule ne pouvait les maîtriser. La réussite de cette belle aventure scientifique reposait donc grandement sur la contribution de nombreuses personnes que je tenais à remercier ici.

En premier lieu, je remercie Dario Gerace, Philippe Boucaud, Allard Mosk, Christelle Monat et Xavier Checoury d'avoir accepté d'évaluer mes travaux de thèse, et pour l'intérêt qu'ils ont montré à ces réalisations.

Durant ma thèse, j'ai eu la chance de n'avoir pas un mais trois encadrants formidables, remarquablement complémentaires dans leur approche scientifique, et je mesure le privilège que cela a constitué. Il n'est pas anodin que leur collaboration soit si fructueuse dans tous les sujets auxquels ils s'attaquent, puisque ils mettent les doctorants dans de si bonnes conditions de réussite.

Pour commencer, je tiens à remercier Alfredo De Rossi puisque c'est lui qui, le premier, m'a proposé ce sujet lorsque je cherchais une thèse « comportant de l'optique non linéaire ». Directeur de thèse exemplaire, il a par la suite été d'une disponibilité extrême, et c'est grâce à son exigence, sa rigueur et sa passion que l'objectif si ambitieux de ce travail a été atteint. Je ne sais d'ailleurs toujours pas lequel de nous deux était le plus euphorique lors de la première observation de l'oscillation paramétrique, mais ce moment restera l'un des plus marquants de ma thèse.

Je souhaite également remercier mon co-directeur de thèse, Fabrice Raineri, qui m'a accueilli au C2N. J'ai pu compter sur son soutien moral et scientifique à chaque instant, pour me pousser à venir à bout de ce projet de thèse. Plus important encore, son optimisme et son enthousiasme pour la recherche, si communicatifs, ont eu raison de mon pessimisme prudent pour renouveler constamment l'ambition nécessaire à la réussite de ce travail.

Enfin, je remercie Sylvain Combrié, co-co-directeur officieux, pour avoir partagé son expertise précieuse à la fois dans le laboratoire d'optique et la salle blanche, et pour avoir été disponible sans réserve pour maniper ou échanger des idées.

Au-delà de l'aspect scientifique, je suis profondément reconnaissant pour la gentillesse et le soutien dont Alfredo, Fabrice et Sylvain ont constamment fait preuve à mon égard.

Au C2N, j'ai eu la chance d'intégrer une équipe de recherche vivante et

stimulante. Je remercie donc Dorian Sanchez, Quentin Chateiller, Francesco Manegatti, Léa Constans, Maxime Delmulle et Alexandre Bazin pour tous les bons moments autour d'un café ou d'un bain d'acide fluorhydrique. Je garde en particulier le souvenir d'un merveilleux voyage dans les vastes contrées de l'ouest américain.

Je remercie plus généralement tous les membres de l'équipe pour la bonne ambiance de travail et mes collègues doctorants et post-doctorants en particulier. Les trajets quotidiens jusqu'à Marcoussis puis Saclay étaient bien allégés grâce à la perspective de les retrouver. Merci donc à David Barral, Rui Zhu, Giuseppe Modica, Guilhem Madiot, Ivens Saber, Mathias Marconi, Bruno Garbin, John Bigeon et Anirudh Pammi.

Une thèse de nanophotonique expérimentale dépend grandement de la qualité des échantillons disponibles. Je remercie donc chaleureusement Isabelle Sagnes, Grégoire Baudoin et Konstantinos Pantzas pour les épitaxies de grandes qualité ainsi que les conseils pour le développement de procédés de fabrication. A Thales, je remercie également Gaëlle Lehoucq pour les épitaxies de GaInP.

Il régnait dans la salle blanche de Marcoussis une excellente ambiance de travail, détendue et collaborative qui a grandement facilité la réalisation de mes échantillons. A ce titre, je remercie plus particulièrement Stéphane Guilet, Alan Durnez, Sophie Bouchoule et Christophe Dupuis pour l'aide qu'ils m'ont procurée pendant mes étapes de fabrications.

Si j'ai pu me consacrer entièrement à ma recherche pendant ces années, c'est parce qu'il y avait en support une infrastructure efficace, malgré les difficultés liées au déménagement du laboratoire. Merci à Alain Péan et Medhi Idouhamd du service informatique ainsi que Joëlle Guitton et Marina Ferreira des services administratifs pour leur efficacité.

Si j'ai finalement découvert que je n'avais pas deux pieds gauches, c'est grâce au Club Nazionale de Nozay, qui retrouvera un jour sa gloire d'antan.

Je remercie également Daniel Dolfi et Arnaud Brignon pour m'avoir accueilli dans le groupe de recherche en physique de TRT. Un immense merci à Aude Martin pour m'avoir mis sur les bons rails. Merci aussi à Grégory Moille et Inès Ghorbel. Je remercie également tous les membres des laboratoires OTS et MNP pour les précieux échanges scientifiques et humains avec une pensée particulière pour Eric Lallier, François Gutty, Christian Larat et Arnaud Grisard qui m'ont encadré en stage de master et d'une certaine façon, par qui tout a commencé. Merci à Jérome Bourderionnet et Delphin Dodane pour les (multiples) emprunts

de source laser et Fabien Bretenaker pour l'emprunt (longue durée) du filtre.. Merci également à Dominique Papillon et Barbara Petit qui à présent profitent d'une retraite bien méritée.
Pour terminer, j'adresse un immense merci à mes proches qui m'entourent depuis de nombreuses années et dont la compagnie apporte un équilibre de vie indispensable. J'adresse une attention particulière à Sam et Eti, qui ont tant eu à cœur de me voir finir ce projet. Je profite également de cet avant-propos pour remercier ici mes sœurs, mes grands-parents et tout spécialement mes parents pour m'avoir encouragé à suivre la voie de mon choix, depuis si longtemps. Enfin, merci à Béa, d'avoir traversé avec moi cette aventure, et sans qui ces lignes n'auraient pu être écrites.

Synthèse en français

Un traitement tout optique du signal pourrait réduire considérablement la consommation d'énergie et augmenter le débit de données par rapport à son analogue électronique. Cette approche nécessite l'intégration de multiples systèmes photoniques sur une puce. Les composants qui exploitent les interactions paramétriques peuvent réaliser différentes fonctions comme la conversion de longueur d'onde, l'amplification, l'échantillonnage et la commutation ainsi que générer des états non classiques de la lumière pour l'information quantique. Les micro-résonateurs non-linéaires sont intéressants car ils permettent la réduction de l'empreinte sur puce du composant et de la puissance nécessaire pour activer les effets non-linéaires. Parmi eux, les cavités à cristaux photoniques (PhC) paraissent être particulièrement prometteuses du fait de leur capacité à confiner la lumière dans un volume proche celui permis par la limite de diffraction. Pourtant, elles souffrent de la difficulté de contrôler la dispersion de leurs modes résonants, ce qui explique que les efficacités non-linéaires observées sont restées bien inférieures aux maxima théoriques prévus pour ces structures. Partant des travaux réalisés précédemment au sein de l'équipe de recherche, l'objectif de ce travail de thèse consiste à exploiter pleinement le potentiel des cavités PhC non-linéaires.

Les cavités étudiées dans ce travail ont été conçues pour être l'analogue optique de l'oscillateur harmonique quantique. Lorsque les photons sont soumis à un potentiel parabolique, les modes résonants sont équispacés en fréquence, ce qui correspond à la règle de conservation de l'énergie requises pour les interactions paramétriques. Un tel potentiel parabolique a été construit par l'introduction d'un second réseau périodique inséré dans un guide d'onde à cristal photonique réalisé dans une membrane suspendue. Ce design, appelé bichromatique, engendre par effet Moiré une localisation des photons caractérisée par le potentiel d'André-Aubry. Ce potentiel peut être approximé près du centre de la cavité créée par une parabole. Cependant, la caractérisation linéaire des résonateurs à l'aide d'une méthode interférométrique montre que le désordre structurel induit une déviation par rapport aux fréquences visées supérieur à la largeur de raie des modes, qui possèdent des facteurs de qualité élevés, aux alentours de 2×10^5. Une étude statistique sur des dizaines de cavité montre que ce désordre est localisé, ce qui affecte chaque mode de la cavité dans une mesure différente. Puisque il est impossible de supprimer ce désordre intrinsèque aux fluctuations du procédé

de production, une technique de compensation post-fabrication est nécessaire. Pour résoudre ce problème, un procédé d'ajustement thermique qui exploite la répartition inhomogène de la distribution spatiale des modes électromagnétiques est introduit. L'idée est de tirer parti de la structure des modes de Hermite-Gauss de l'oscillateur harmonique, dont l'énergie est concentrée dans des lobes aux extrémités du mode. Lorsqu'une certaine énergie est injectée dans un mode via un laser de pompe, un gradient de température se forme dans la cavité superposé au premier ordre avec la distribution d'énergie électromagnétique. En conséquence, les modes adjacents verront leur fréquence se décaler par effet thermo-optique, mais d'une quantité propre à chaque mode. Ce procédé permet donc de changer la fréquence de chaque mode individuellement, et de mettre de façon systématique la cavité en configuration triplement résonnante. Cette technique d'ajustement est employée pour observer du mélange à quatre ondes stimulé et spontané avec des efficacités record. L'oscillation paramétrique dans une cavité PhC est démontrée pour la première fois dans un échantillon avec des facteurs de qualité plus élevés.

Une seconde plateforme est développée, basée sur l'intégration hybride d'une cavité PhC sur un circuit en silicium, avec une empreinte sur puce réduite et une excellente capacité d'intégration. Un mélange à quatre ondes efficace est encore une fois observé en utilisant le même procédé d'ajustement que précédemment.

Publication List

- Gabriel Marty, Sylvain Combrié, Alfredo De Rossi, and Fabrice Raineri. "Hybrid InGaP nanobeam on silicon photonics for efficient four wave mixing." APL Photonics 4, no. 12 (2019): 120801.

- Gabriel Marty, Sylvain Combrié, Fabrice Raineri, and Alfredo De Rossi. "Photonic crystal optical parametric oscillator." Nature photonics 15, no. 1 (2021): 53-58.

Table of Content

Introduction **4**

1 Integrated Nonlinear Optics in cavity **8**

1.1 Nonlinear optics in a cavity: fundamentals 9

1.1.1 Linear and Nonlinear Polarization 9

1.1.2 Third Order Nonlinear Effects in Semiconductors 10

1.2 Material Properties for efficient FWM 14

1.2.1 Indium Gallium Phosphide 17

1.3 FWM in microcavities 18

1.3.1 General properties of a cavity 18

1.3.2 Nonlinear frequency conversion 20

1.3.3 The optical parametric oscillator 21

1.4 Brief state of the art in integrated OPO 22

1.4.1 Different class of integrated OPOs 22

1.4.2 Reduction of the modal volume 25

1.5 Photonic crystal Cavities 25

1.5.1 Principle of Photonic Crystal cavities 25

1.5.2 Photonic crystal cavities for nonlinear optics 29

1.5.3 The role of structural disorder 31

2 Model for Parametric interaction in multi-mode cavities **34**

2.1 Properties of a cavity in the linear regime 35

2.1.1 Modal structure: spatial problem 35

2.1.2 Temporal Coupled Mode Theory 35

2.1.3 Introduction of losses 37

2.2 Model of a cavity in the nonlinear regime 39

2.2.1 Nonlinear polarization 40

2.2.2 Nonlinear cross section and coupling coefficient 42

2.3 Resonant FWM in a cavity 44
2.3.1 Master Equation 44
2.3.2 Detuning of the cavity by thermo-optic effect 46
2.3.3 Undepleted pump approximation 47
2.4 Degenerate FWM: spontaneous and stimulated FWM 48
2.4.1 Degenerate FWM for PhC cavities 48
2.4.2 Parametric oscillation 48
2.4.3 Stimulated FWM 50
2.4.4 Relation between stimulated and spontaneous emission . . 52
2.4.5 Quantum model for Spontaneous Emission 54
2.5 Three Photon Absorption 56

3 Design and fabrication of PhC multi-mode cavities 59
3.1 Principle of confinement: light cone and radiative modes 60
3.1.1 Trapping light in a potential 61
3.2 The bichromatic cavity for FWM 62
3.2.1 An optical harmonic oscillator 62
3.2.2 Design of the bichromatic cavity 63
3.2.3 Fabrication of the bichromatic cavity 66
3.2.4 Linear characterization 67
3.3 1D PhC on SOI: the nanobeam cavity 70
3.3.1 Principle of the SOI structure 70
3.3.2 Design of the nanobeam cavity 72
3.3.3 Fabrication process 75
3.3.4 Linear Characterisation 79

4 Four Wave mixing in PhC cavities 84
4.1 Thermal tuning for PhC cavity alignment 85
4.1.1 Thermal locking of a cavity resonance 85
4.1.2 Thermal tuning for inhomogenous modes 86
4.1.3 Thermal pulling measurement 87
4.2 Modeling the nonlinear cavity 88
4.2.1 Extraction of the on-chip power and the coupling losses . . 88
4.2.2 Energy in the cavity and nonlinear absorption 90
4.2.3 Effective temperature of the mode 92
4.2.4 Modeling FWM in the cavity 93

4.3 FWM in Bichromatic cavity . . . 97
4.3.1 Experimental Setup . . . 97
4.3.2 Extraction of the nonlinear efficiency . . . 98
4.3.3 Comparison with the theoretical model : scaling with the Q factor . . . 99
4.3.4 Observation of spontaneous FWM . . . 103
4.3.5 Observation of parametric oscillation in PhC . . . 106
4.4 FWM in hybrid PhC on SOI . . . 109
4.4.1 Experimental Setup . . . 109
4.4.2 Observation of stimulated FWM . . . 110
4.5 Discussion of the results . . . 111
4.5.1 Wavelength conversion in integrated platform . . . 111
4.5.2 Parametric oscillation in integrated platform . . . 113
4.5.3 Consideration on the footprint . . . 115

Conclusion **118**

Annexes **123**

A Linear characterization with OCT **124**
A.1 Principle of measurement . . . 124
A.2 OCT setup . . . 124
A.3 Fourier analysis of the signal . . . 126
A.4 Interpretation of the measurement . . . 127
A.4.1 Single-Ended cavity . . . 127
A.4.2 Side-Coupled cavity . . . 128
A.5 Precision of the frequency measurement . . . 132

B Parameters used in the numerical simulations **134**

Bibliography **147**

Introduction

The first realization of light amplification by stimulated emission radiation in 1960[1] granted access to a radically new light source type. Its singular properties unveiled many possibilities among which the concentration of coherent optical field at an unprecedented level. It took only one year after Maimann's first laser to focus the beam on a nonlinear crystal and observe second harmonic generation[2]. Experimental access to optical nonlinearities was at the time limited to electrically driven Kerr or Pockels effect. Soon after, Askaryan and Hercher discovered the optical Kerr effect through self focusing[3, 4]. It was followed by the observation of Raman scattering, supercontinuum generation... Among these, parametric oscillation[5] is an important achievement as it allows to tune the frequency of laser light.

In parallel, the advent of low loss optical fibers revolutionized the field of telecommunication and data transmission. Guided optics enabled light matter interaction over a very long length compensating for a lower interaction strength than in bulk crystal. Parametric amplification was studied very early in fibers[6]. It opened a wide range of applications for all optical signal treatment. This is of particular interest in the context of a growing need for higher bandwidth and energy efficiency in the worldwide data traffic. Indeed, an electronically signal processing requires a conversion of the optical signal of the fiber into an electrical signal. The data rates are limited by the bandwidth of this conversion, typically 100 GHz. All optical signal processing could push this limit back because optical processors could operate at higher speeds and cover a larger bandwidth. This perspective brought integrated optical circuits as a promising alternative for standard electronic chips. A single device could perform a massive parallel processing and the integration of nonlinear optics on chip has been a subject of extensive research over the past decades. Among optical nonlinearities, parametric interactions have a very short response (femtosecond). The corresponding theoretical data rate is superior to terabit-per-second which

would be a huge increase. Depending on the application, parametric interaction could perform different tasks such as wavelength conversion, signal amplification and regeneration, sampling, switching, memories.
Finally, parametric nonlinearities are also extremely useful for quantum information, e.g. the transmission of quantum states[7]. Their coherence properties can be exploited to generate and manipulate non-classical states of light, and on-chip quantum photonics will likely include some of these nonlinear functions.

Context of the study

The work presented in this manuscript comes within the scope of the global research effort of integrating photonics functionalities on a chip. More particularly, it is the continuation of years of collaborative work on integrated nonlinear nanophotonics between the Centre de Nanosciences et Nanotechnologies (C2N) and Thales Research and Technology (TRT). This work has been motivated by the goal to study wave mixing in a platform that combines both an interesting material (Indium Gallium Phosphide) and geometry (Photonic Crystal Cavity). It covers two different technologies (suspended and bonded membranes) that were developed by the two institutions. All the main steps of this study were performed during this thesis, from the theoretical modelling of the system to the design (except for the suspended membrane design), fabrication in clean-room, optical characterization and wave mixing experiments.

Outline of the manuscript

The manuscript is organized to describe the successive steps that lead to the realization of efficient Four Wave Mixing (FWM) in different photonic crystal platforms and the observation of parametric oscillation.

In the first chapter, a theoretical introduction summarizes the physical mechanisms that are taken into account for the rest of the study. In particular, it will emphasize the role of resonant FWM and will briefly review the state of the art in this domain. The difficulties to achieve FWM in Photonic Crystals will also be discussed.
The second chapter details the theoretical model that has been developed to describe the nonlinear behavior of the cavity using Temporal Coupled Mode

Theory. The regime of spontaneous and stimulated FWM are treated under the assumption of a strongly dominant thermal nonlinearity. We will explicit the link between the two regime that will be experimentally verified.
The third chapter explains the design, fabrication and linear characterization of PhC cavities for resonant FWM. Two strategies are developed, the first one with suspended membrane and the other with bonded membrane connected to a silicon circuitry, although based on the same confinement principle. A statistic study on the fabricated structures is performed and shows that an additional tuning mechanism is required to unveil the full potential of the cavities for FWM.
The fourth chapter introduces a thermal tuning technique specific to the used design. This technique is then used to performed FWM in the two platforms with record efficiency. The comparison experiment/theory corroborates the model developed in Chapter 2. Finally, we will explain how we were able to reach parametric oscillation and will compare these results to state-of the art platforms.

Chapter 1

Integrated Nonlinear Optics in cavity

The advent of fiber optics provides a formidable tool to study and implement nonlinear optical functions as their low losses results into a very large interaction length between the optical field and the fiber core. A desirable perspective would be to drastically reduce this length with the aim of on-chip integration. As a result, the choice of the best nonlinear platform depends on multiple parameters such as nonlinearity, confinement, losses etc. As always, trade-offs need to be made, depending on the application that is targeted. This chapter shortly reviews the tools to understand this problematic and provides a state of the art of integrated parametric oscillators.

In the first section, we will introduce the nonlinear effects that are taken into account in this work and provide a physical description. In the second part, we will discuss the relevant material parameters relevant for efficient nonlinear optics. In the third part, we will explain the interest of using a cavity to enhance these effects and we will end with a brief review of the performances of state-of-the-art integrated nonlinear cavities.

1.1 Nonlinear optics in a cavity: fundamentals

1.1.1 Linear and Nonlinear Polarization

A strong electromagnetic excitation can lead to a modification of the optical properties of the matter. When an electromagnetic field is shone upon a dielectric material, the electronic clouds of the particles constituting the material are modified by the Lorentz force. When the electric field oscillates, the electronic clouds oscillates as well and the medium can be described as an ensemble of oscillating dipoles. This density of dipoles is called *polarization*. When the electromagnetic field is weak, the response of the material is linear that is to say the polarization depends linearly with the applied field. In particular, the polarization will oscillate at the same frequency than the electromagnetic field.
In the case of nonlinear optics, the field is strong enough to induce an anharmonic response of the dipoles. As a result, the polarization does not depend linearly on the input field anymore. The nonlinear part of the response is treated as a perturbation of the linear solution. The polarization is then expressed as a series expansion[8]:

$$\mathbf{P}(\mathbf{t}) = P_{LIN}(t) + P_{NL}(t) = \epsilon_0 \underline{\underline{\chi}}^{(1)} \mathbf{E}(\mathbf{t}) + \epsilon_0 [\underline{\underline{\underline{\chi}}}^{(2)} \mathbf{E}(\mathbf{t})\mathbf{E}(\mathbf{t}) + \underline{\underline{\underline{\underline{\chi}}}}^{(3)} \mathbf{E}(\mathbf{t})\mathbf{E}(\mathbf{t})\mathbf{E}(\mathbf{t}) + ...] \tag{1.1}$$

where ϵ_0 is the vacuum permittivity and $\underline{\chi}^{(j)}$ is a $j+1$ order tensor corresponding to the j^{th} order susceptibility.
The first term of the expression corresponds to the linear polarization. The refractive index n and linear losses α of the material are related to its real and imaginary parts. The higher order terms correspond to the harmonics of the polarization and become a source term of new harmonic components of the light. The second order term, associated to $\chi^{(2)}$, involves the product of three waves. The $\chi^{(2)}$ term is the dominant nonlinear contribution. However, a center of symmetry in the crystalline arrangement of the medium nullifies all component of the $\chi^{(2)}$ tensor. Therefore, second order nonlinearities can only take place in non centro-symmetric medium. Conversely, odd-order susceptibility tensors are never null. Thus, third order nonlinear effects, that involve four waves, are the dominant terms in centro-symmetric material. This manuscript will treat third order nonlinear effects only. It is not due to material constraints because the material used, namely Indium Gallium Phosphide (InGaP) has a nonzero $\chi^{(2)}$ [9]. The reason lies in the difficulty to engineer the dispersion of a cavity on

a large frequency bandwidth, especially in Photonic Crystals. While it is not treated here, this topic is still active and recent progress has been reported[10].

1.1.2 Third Order Nonlinear Effects in Semiconductors

This manuscript deals with the interaction of four waves through the third order susceptibility $\chi^{(3)}$ in a semiconductor. Here, the electronic energy states are separated by a forbidden band. The width of this band is called the bandgap energy, E_g. If a photon has an energy larger than E_g, it can excite an electron from the lower level band, the valence band, to the higher level band, the conduction band. Changing the population of electron in these band lead to a change in the optical proprieties of the semiconductor, and is characterised by a lifetime in the excited state. However, if E_g is large enough, photons are no longer absorbed, and nonlinear interactions go through virtual levels, with a quasi-instantaneous response (few femtoseconds typically). Therefore, it is important to distinguish between processes that involve real or virtual electronic transition: only in the first case an exchange of energy with the medium will take place.
The equation 1.1 can be used in the temporal domain only in a dispersionless and lossless medium, which corresponds to the case of a purely real and frequency independent susceptibility tensor. In the general case of a complex susceptibility, it is necessary to express the polarization in the frequency domain. This requires a treatment of each frequency component separately. The electric field and the polarization are assumed to be decomposed in frequency harmonics, writing:

$$\mathbf{E}(\mathbf{t}) = \sum_k \mathbf{E}(\omega_\mathbf{k}) \exp \imath\omega_k t \tag{1.2}$$

$$\mathbf{P}(\mathbf{t}) = \sum_k \mathbf{P}(\omega_\mathbf{k}) \exp \imath\omega_k t \tag{1.3}$$

The sum on the harmonics is carried out on positive and negative frequencies so that the temporal field is real. As stated above, the third order processes can be divided in two categories: the elastic and the inelastic processes. The first one involves no energy transfer with the medium, and uses the real part of the susceptibility tensor. The second one involves an energy transfer with the medium, and involves the imaginary part of the tensor. These effects, that we are going to detail further, are depicted in Fig.1.1.

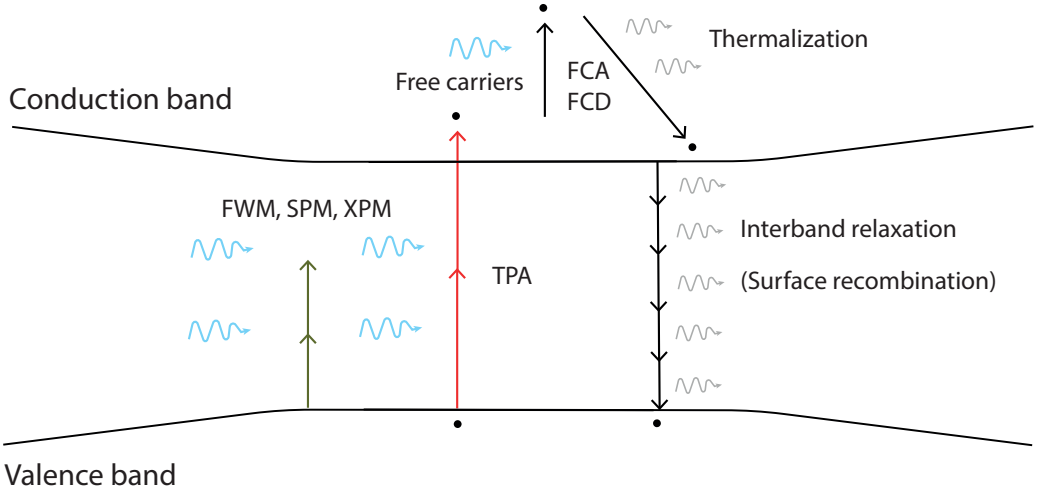

Figure 1.1: Illustration of the 3rd order nonlinearities in a semiconductor. If the photon energy is inferior to half the bandgap, it will trigger elastic effects (SPM, FWM, XPM). If it is superior to half the bandgap, it will trigger inelastic effects that involve absorption by the material. The generated carriers generates additional absorption through FCA. The relaxation lead to phonon creation that will heat the semiconductor and modify the refractive index (thermo-optic effect).

Elastic processes: the intensity-dependent refractive index

A strong electromagnetic field can cause a modification of the refractive index of a material: this is often called the optical Kerr effect. The real part of the refractive index n of the material is written:

$$n = n_0 + n_2 I \tag{1.4}$$

where n_0 is the linear refractive index, $I = 2n_0\epsilon_0 c|E|^2$ is the light intensity and n_2 is the nonlinear refractive index[1]:

$$n_2 = \frac{3\mathbb{R}e(\chi^{(3)})}{4n_0^2(\omega)\epsilon_0 c} \tag{1.5}$$

The nonlinear part of the refractive index depends on the square of the electric field, and causes several effects. First, the effects that modifies the spectral properties of the light. They are called Self-Phase Modulation (SPM) and Cross Phase Modulation (XPM). These effects are not subject to any resonance condition and are therefore always active. They affect mainly the propagation of a

[1]In this expression, all fields are supposed to be linearly polarized so that only one component of the tensor contributes to the refractive index

light pulse by broadening its spectrum, and they can be responsible for continuum generation.
On the other hand, the Kerr effect can also cause a transfer of energy between different fields: this is called four wave mixing (FWM). It results in the apparition of new frequency components. We call FWM the annihilation of two pump photons to generate two photons with different energy, and the annihilation of three pump photon to create a third harmonic is called Third Harmonic Generation (THG). During this type of nonlinear process, the interacting fields need to be maintained in phase. This defines a phase-matching condition on the wavevectors k outside of which the nonlinear effect is not efficient.

In this work, we will focus on degenerate FWM : the two pump photons are degenerate in frequency, which allows to use only one laser for the pump. Our goal is to generate as efficiently as possible the signal and idler photons according to the relation:

$$2\omega_p = \omega_s + \omega_i \tag{1.6}$$

where p, s, i stand respectively for pump, signal and idler. The phase matching condition then writes:

$$2k_p = k_s + k_i \tag{1.7}$$

If it is virtually possible to generate any signal/idler pair subject to the energy conservation from the pump , only those who satisfy the phase matching condition will be efficient. Practically, only a specific bandwidth in a waveguide or specific set of resonances in a cavity, both determined by the dispersion of the structure will be useful. This aspect will be detailed later when we will describe the optical cavity. Nonetheless, the parametric gain available in a material depends heavily on the nonlinear refractive index.

Inelastic processes: the Nonlinear absorption

In the previous part, we reviewed the consequences of the real part of the refractive index. Conversely, the imaginary part of the susceptibility adds a nonlinear term on the imaginary part of the refractive index, e.g. to the losses. This phenomenon is called two photon absorption (TPA). Contrary to the Kerr effect, the energy of the two photon excites a real level of energy of the material involving an energy transfer between the electromagnetic field and the material. Physically, in a semiconductor, it corresponds to an excitation of an electron in the valence band to the conduction band by the absorption of two photon at the same time

as pictured in Fig.1.1. The expression of the losses becomes:

$$\alpha = \alpha_0 + \alpha_2 I + \alpha_{FCA} I^2 \tag{1.8}$$

where α is total loss coefficient, α_0 are the linear losses, α_2 is the TPA coefficient and α_{FCA} is the free carrier absorption coefficient, with

$$\alpha_2 = \frac{-3\omega \mathbb{I}m(\chi^{(3)})}{2c^2 n_0(\omega)^2 \epsilon_0} \tag{1.9}$$

Two photon absorption is detrimental to the efficiency of third order nonlinear processes. Unfortunately, it cannot be compensated by increasing the pump power in order to increase the parametric gain because TPA will scale identically. However, we will see later that an appropriate choice of material can mitigate the problem. Raman and Brillouin scattering are also inelastic processes but they will be neglected in this work because they are not resonantly enhanced.

Nonlinear response due to free carriers

The electrons excited in the conduction band become free to absorb light through Free Carrier Absorption (FCA). The losses produced by FCA are proportional to the square of the intensity. Increasing the power of the pump will eventually make FCA dominant and clamp the nonlinear gain. FCA triggers a modification of the refractive index by the free electrons (Free Carrier Dispersion, FCD). The strength of FCA and FCD is directly related to the carrier density. The timescale of these effects depends on the carrier lifetime in the material, governed by the recombination rate. Typically, the response range from few ps to ns. A fraction of the energy is converted into heat through recombination or relaxation of the electron/hole pairs generated by TPA. This thermalization leads to a change of the refractive index through the thermo-optic effect, and in extreme situation, can damage the medium. It is crucial to limit TPA and mitigate free carriers in semiconductors when we aim at realizing efficient wave mixing. For different application, such as all-optical switching, FCD is exalted on purpose[11].
Finally, surface states can play an strong role in absorption of the photons and recombination of the carriers. They originate from finite size of the crystal, the semiconductor growth (impurities) and fabrication imperfection that disrupt the periodicity. The surface of a crystal possess lower energy bands than the bulk, and these mid-gap states are more prone to absorption.

Thermal nonlinearity

Thermal nonlinearity, also called the photothermal effect consists in a change of the refractive index due to the heating of the structure. Heating is caused when a fraction of the light is absorbed in the material through residual absorption. It leads to an increase of temperature, that can go up to damage the material. The effect on the refractive index is expressed as :

$$n = n_0 + \frac{dn}{dT}\Delta_T \tag{1.10}$$

where $\frac{dn}{dT}$ is the thermo-optic coefficient of the material and Δ_T is the change of temperature induced by the optical absorption. Depending on the material, the thermo-optic coefficient can be either positive or negative. The time scale of the thermo-optic effect is much longer (few μs to s) than the carrier timescale. As a result, the thermo-optic effect sets the time necessary to reach thermal equilibrium. However, it is not always detrimental. In the case of resonant FWM, the long response time of the thermal nonlinearity is used to initiate a soliton state by starting to sweep the pump laser faster than the thermal response of the cavity[12]. The thermo-optic effect is also used to tune the resonance frequencies in a cavity, and heating the crystal is a common way of tuning the wavelength output in FWM.

1.2 Material Properties for efficient FWM

In this section and with the help of the physical insight provided by the previous part, we will try to list the main characteristics of a suitable material in order to carry out FWM experiment. Several material found in the literature are listed and compared.

Index contrast

As stated in the previous part, the linear refractive index derives directly from the real part of the first order susceptibility. A large refractive index allows tight confinement in integrated structure via the total internal reflection mechanism. Thus, a high index contrast between the nonlinear material and the cladding (whether it is air or another semiconductor) allow to reduce the size of the integrated component thanks to limited radiation and bending losses. This feature is crucial for dense integration on a chip as well as for energy efficiency. Because

we work a telecom wavelength here, we seek for a material with a large refractive index at 1550 nm. To compare, optical fibers, whose light confinement relies on a small index difference, have a cross-section much larger than integrated waveguides. Hence, the effective mode cross section is of the order of 100 μm^2. This value is typically between two and three order of magnitude lower in integrated waveguides. It is therefore possible to obtain a much larger energy density in integrated devices, which is extremely useful for nonlinear optics.

Linear Losses

As stated in the previous section, linear losses are accounted by the imaginary part of the first order susceptibility. It is crucial that this term is as low as possible. In material where TPA is inhibited, linear losses set the limits of the nonlinear interactions. For example, in integrated cavities, it is the linear losses that are limiting the Q factors. The linear propagation losses are usually given with a coefficient α in m^{-1}, or sometimes in log-scale, $dB.m^{-1}$. This coefficient allows to extract an effective length of propagation in the material, which corresponds to a propagation in a shorter but lossless material. Therefore, the effective length is the true length of interaction between the light and the matter. Optical fibers can reach extremely low propagation losses, below 0.2 $dB.km^{-1}$. This low losses allows to have very long interaction length, almost identical to the physical length of the fiber. Integrated devices on the other hand have for a long time struggled to reduce their propagation losses. In state of the art silicon-based dielectric, losses can reach 0.13 $dB.m^{-1}$ [13], which is still way larger than in optical fibers. In III-V semiconductors, the lowest losses reported are 0.17 dB/cm [14]. However, these losses do not originate from the material itself but from the roughness induced scattering, dependant of material patterning and processing[15].

Material Nonlinearity and TPA

The material nonlinearity n_2 is of course a key parameter in the choice an adequate platform. A useful quantity to compare different nonlinear platform is the so-called nonlinear waveguide parameter $\gamma_{WG} = \frac{n_2 \omega}{c A_{eff}}$[16]. The value of γ_{WG} increase with the nonlinear index n_2 and is inversely proportional to the effec-

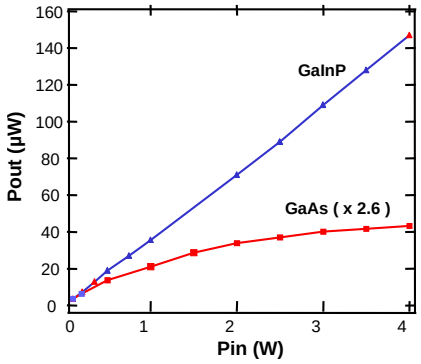

Figure 1.2: Impact of TPA on output power for a photonic crystal waveguides: GaAs (red) output is limited by TPA whereas GaInP (blue) output is linear[18].

tive mode area A_{eff}[2]. In particular, the nonlinear phase shift caused by SPM is directly proportional to the nonlinear parameter γ_{WG}, hence γ_{WG} is deduced by measuring the broadening of a propagating pulse. High values of γ_{WG} take into account the combination of large n_2 as well as the ability to confine light tightly, given by a large index contrast. If TPA is ruled out by a large bandgap, the nonlinear interaction of a propagating wave is ultimately set by the linear losses. The maximal value of this effective length, $L_{eff} = \frac{1-e^{-\alpha L}}{\alpha}$ is $\frac{1}{\alpha}$. The ratio γ_{WG}/α is therefore an important indicator that encompasses nonlinearity, losses and index contrast.

TPA occurs whenever the energy of two photon is superior to E_g ($2\hbar\omega > E_g$). At 1550 nm, E_g must be greater than 1.6 eV, while in silicon, this value is 1.12 eV. Thus, any FWM process will be dominated by TPA and FCA. Some achievements were still made with P-I-N junction to reduce the free carriers lifetime, particularly in silicon. However, this approach only reduces the lifetime of the carriers but do not cancel TPA that ends up to be detrimental. Fig.1.2, from [18], shows the difference of transmission of two photonic crystal waveguides at telecom wavelength: one made of GaAs (E_g = 1.4 eV) and the other in InGaP (E_g = 1.9 eV). The losses caused by TPA severely lessen the optical output. For these reasons, widegap materials are extremely appealing for nonlinear optics, even if in semiconductors, the nonlinear index n_2 decreases with a higher bandgap[19].

[2] A_{eff} is in fact the third order nonlinear effective area that takes into account the overlap between the modes of the interacting waves[17]

Different Material for integrated nonlinear optics

Comparing the parameter γ_{WG} of an optical fiber with a silicon waveguide on insulator (SOI) highlights the advantages of integrated optics for nonlinear operation: γ_{WG} jumps from 0.001 W/m (up to 2 W/m in highly nonlinear fibers) to >100 W/m[20]. There is a great variety of material used for nonlinear optics in the literature.

Silicon seems attractive because of its high $n_2 = 5 \times 10^{-18} m^2 W^{-1}$, combined with a large $n = 3.46$ at telecom wavelength. However, the energy bandgap E_g of silicon does not prevent two-photon absorption at telecom wavelength. Frequency comb generation have been demonstrated in silicon in the mid-infrared, where photon bears lower energy (TPA stops around 2.2 μm in silicon)[21]. To operate in the telecom band, a mechanism to remove the photo-generated carriers is needed[22].
To address this point, a variety of glasses have been experimented such as chalcogenide, Hydex or silicon nitride. They have a relatively low index, which limits the confinement and, according to the empirical Miller's rule, the nonlinearity in these materials scales up with refractive index[23]. However, very low loss can be achieved in glasses, and their low γ_{WG} is offseted by an increased interaction length. Silicon-rich materials such as Si_7N_3 have been specifically developed for nonlinear optics as a TPA-free platform. Here, the limitation comes from the relatively high linear losses. All these platform possess the advantage of being almost directly CMOS compatible, requiring little development to the existing process to reach mass-production.
Semiconductors made of III-V alloys have drawn attention as nonlinear platform primarily thanks to their large bandgap to avoid TPA[24]. Their n_2 is typically around 10^{-17} W.m^{-1}, which is three orders of magnitude larger than silica. Their large n allows to obtain an A_{eff} hundreds times smaller than in a fiber.

1.2.1 Indium Gallium Phosphide

In this work, the nonlinear material is Indium Gallium Phosphide ($In_xGa_{1-x}P$). The refractive index of InGaP is 3.13 at telecom wavelength which is comparable to silicon and the nonlinear index is $n_2 = 0.6 \times 10^{-17} m^2.W^{-1}$. Like many III-V semiconductors, it has a zinc blend type crystal symmetry (group $\bar{4}3n$). InGaP

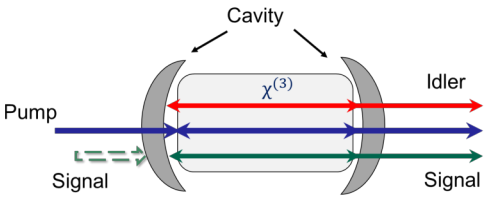

Figure 1.3: Schematic of resonant spontaneous and stimulated FWM. When the threshold of the cavity is reached, the system is called an optical parametric oscillator (OPO)

was introduced in nonlinear optics for second harmonic generation[9]. TPA-free SPM[25] and supercontinuum generation[26] have been reported in InGaP on insulator waveguides. The corresponding γ_{WG} is about 475 $W^{-1}.m^{-1}$, six orders of magnitude larger than in a silica fiber. However, the reported linear loss are relatively high, 12 dB/cm compared to state of the art AlGaAs notably which has seen considerable reduction of the losses recently.

1.3 FWM in microcavities

1.3.1 General properties of a cavity

Resonant FWM is pictured in Fig.1.3. Adding an optical cavity to the nonlinear medium increases the interaction between the waves. If the cavity is appropriately designed, the fields will be resonantly enhanced and the energy density inside the medium grows. The important features of a cavity, besides the nonlinear material, are the quality factor Q, the mode volume V, the dispersion control. We can define a linear figure of merit Q/V and a nonlinear figure of merit Q^2/V. Global footprint of the device must be added to this list, since an advantage of a cavity compared to a waveguide is compactness.

The Quality factor

Ideally, a cavity with perfect confinement would retain the photons indefinitely. In reality, this is not the case. The quality factor Q is a figure of merit describing how close a resonator is to the ideal case. It is defined as the ratio of the stored

energy in the system over the power dissipated in one optical cycle[27]:

$$Q = \frac{2\pi \times StoredEnergy}{PowerLoss} = \omega\tau \tag{1.11}$$

This equation, where ω is the resonant frequency defines a photon lifetime τ in the cavity. Hence, if the definition with energy is generic to all type of resonator, it corresponds in an optical cavity to the average time that a photon is trapped before leaking out. In other words, the Q factor quantifies the *temporal confinement* of the photons. This description corresponds to a Lorentzian lineshape in the spectral domain.

The modal volume

The modal volume represents the *spatial confinement* of the cavity mode. Various definitions of the modal volume can be introduced[28]. Here, we use the standard cavity quantum electrodynamics modal volume definition:

$$V_m = \frac{\int_V \epsilon(r)|\mathbf{E}(r)|^2 d^3r}{max[\epsilon(r)|\mathbf{E}(r)|^2]} \tag{1.12}$$

where ϵ is the material permittivity, $\mathbf{E}(r)$ is the electric field dependant of the position r. The volume is defined as the volume occupied by the electromagnetic energy weighted all over space. This definition assumes no radiative leakage otherwise it would lead to a divergence of the integral (and an infinite volume)[29]. A rigorous definition for leaky modes as been derived[30] to provide an adequate definition for cavity with low Q such has plasmonic resonators. In the case of ultra-high Q resonators dealt with here, the mode is well localized and the expression of V_m is used.

Dispersion Control

In FWM, the conservation of energy dictates that the generated frequencies are symmetric with respect to the pump frequency. Integrated resonators need to have their resonant frequencies coinciding with the signal and idler. To do so, the dispersion of a cavity, which is the variation of the free spectral range (FSR) with the frequency, needs to be carefully engineered. This step needs to take into account the material dispersion (relatively low in a small frequency interval) as well as several effects that modifies the dispersion such as the nonlinear phase shift (SPM, XPM) or the thermo-optic effect. Dispersion is

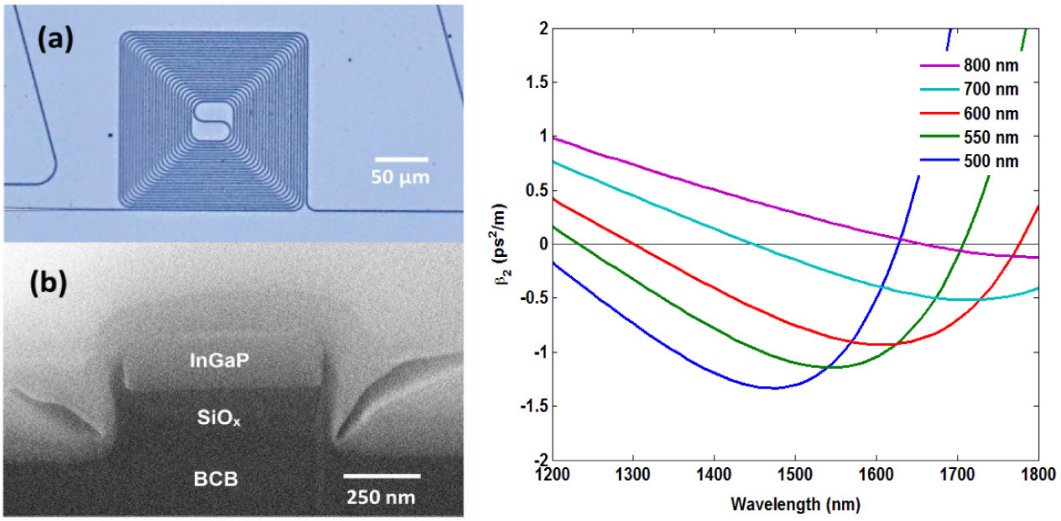

Figure 1.4: Dispersion control of an InGaP waveguide whose cross section is shown b). The dispersion is calculated with a fixed height of 250 nm and a varying width. A positive β_2 means that the dispersion is anomalous. The grey line represents the zero dispersion point. From[25]

said to be anomalous when the FSR increases with the frequency, and normal when it decreases. For waveguiding structures, the dispersion is usually noted as $\beta_2 = \frac{\partial^2 \beta}{\partial \omega^2}$ where β is the propagation constant[31]. The dispersion is engineered simply by changing the width and height of the waveguide. Fig.1.4 shows the dependence of the dispersion of a InGaP waveguide with the variation of the width where all different regimes are achieved. However, in cavities with more complex mode structure such as photonic crystal, with Bloch modes, dispersion engineering involves more degree of freedom.

1.3.2 Nonlinear frequency conversion

Nonlinear frequency conversion consists in seeding a signal in addition to the pump laser to stimulate the FWM for a specific frequency. It is achievable in both waveguides and resonators. This operation regime is called stimulated FWM (S-FWM) and its efficiency is defined as :

$$\eta = 10log(\frac{P_{i,out}}{P_{s,in}}) \tag{1.13}$$

η is the ratio of the idler power collected over the signal power injected inside the cavity, that is the ratio between the amount of light generated by FWM over

the amount of light injected to stimulated it. S-FWM can also be performed in waveguides and it illustrated how greatly the cavity enhance the FWM. In [32], S-FWM is performed in AlGaAs waveguide and ring resonator. With the same pump power of 7 mW, a 110 µm-long ring resonator with a Q around 40 000 increased η by 52.5 dB compared to a simple waveguide of length such that the propagation time is equal to the cavity lifetime (3 mm-long waveguide with the same cross section). It is noteworthy that the counterpart of using a resonant structure is a reduction of the operating bandwidth which becomes limited to the linewidth of the resonance.

1.3.3 The optical parametric oscillator

The performance comparison between resonators and waveguide is not always straightforward, because resonators exhibit a discrete spectrum of narrow resonances instead of a broad bandwidth. In resonator with propagating waves , the resonant structure increases the effective optical path length[33]. A parameter γ_{WG} can be extrapolated and the field enhancement factor of the resonator compared to a waveguide is quantified[32]. The advantage here is to keep the device compact and reduce the operating power. But when it comes to cavity with standing modes such a photonic crystal, the notion of circulating power is no longer valid and the parameter γ_{WG} is not appropriate.
A more general indicator is the threshold for parametric oscillation, which corresponds to the situation where the parametric gain inside the cavity is equal to its losses. The parametric process under consideration here is the spontaneous FWM in which only a pump laser is used to generate signal and idler. The parametric gain increases when the cavity is fed with optical energy through an input port. The threshold for parametric oscillation is defined as the minimal power circulating inside this feeding port that triggers parametric oscillation inside the cavity. The cavity has reached the state of optical parametric oscillator (OPO). A low power threshold is an indicator of an efficient nonlinear platform. In Chapter II, we will see that this key parameter can be written:

$$P_{th} = \frac{\omega^2}{8\gamma Q^2} \tag{1.14}$$

where γ is the cavity nonlinear coefficient, ω is the pulsation of the pump and Q is the geometric mean Q factor of the interacting modes. The parametric gain is

directly proportional to the quantity γ expressed as:

$$\gamma = \frac{c_0 n_2 \omega}{\epsilon_r V_\chi} \tag{1.15}$$

Here, V_χ is the volume of interaction of the waves. We clearly see that a high n_2 leads to a high parametric gain, hence the importance of the choice of the material. It appears also clearly that $P_{th} \propto \frac{V_\chi}{Q^2}$. To exhibit a good FWM efficiency, a cavity needs to have the ratio Q^2/V as high as possible.
Another important parameter is the slope efficiency, that is defined as the curve obtained by plotting the output power of the OPO versus the input pump power. When there is no nonlinear absorption, this curve is linear. The slope efficiency η_{SL} yields:

$$P_{s,out} = \eta_{SL}(P_{in} - P_{th}) \tag{1.16}$$

A high slope efficiency means that an important fraction of the pump power is converted in a useful signal.

1.4 Brief state of the art in integrated OPO

1.4.1 Different class of integrated OPOs

Until now, all integrated OPO have been realized in whispering gallery mode or ring resonators (WGM). These cavities confine light by total internal reflection thanks to a higher refractive index than their surrounding. The first OPOs in microcavity were demonstrated in fused silica microtoroid[44] and CaF_2 WGM resonator[45] which both had $Q \approx 10^8$. Silica toroid was also used to demonstrate the first Kerr frequency comb in microresonator[46], in which cascading FWM generate multiple frequency lines. This class of resonator due to their coupling that require suspended waveguide or fiber is difficult to integrate in a photonic chip.

Ring resonators have been widely studied in the literature[49]. They consist in a waveguide looped on itself and a coupling port to access to the resonator. This type of planar microresonator is more suited for photonic integrated technologies[50]. Parametric oscillation have been demonstrated in numerous material that are compared in Table 1.1. In ring resonators, the oscillation

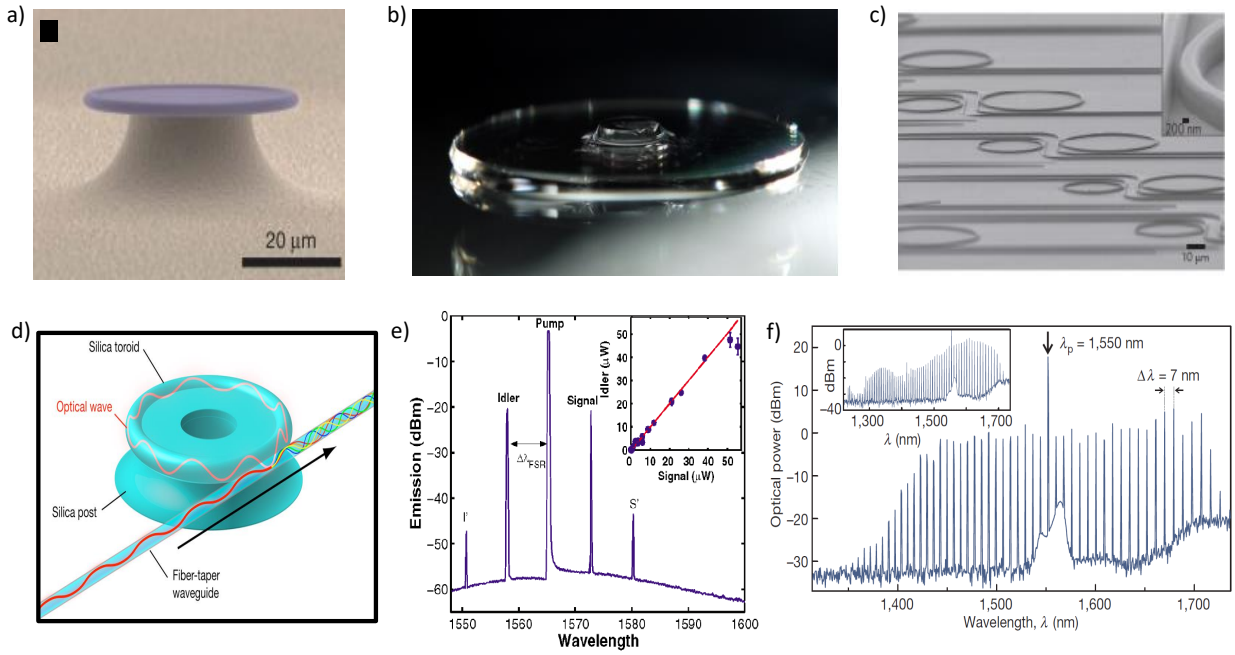

Figure 1.5: Examples of a) Silica microtroid[46] b) Crystalline WGM[47] and c)Ring (Diamond) [39]. The coupling scheme and travelling-wave modal structure is pictured in d)[48] for a microtroid. FWM can lead above threshold to d) parametric oscillation[44] where the generated sidebands are clearly visible. In the case where cascaded FWM occurs, a Kerr frequency comb with multiple lines is generated[46].

Material	n	n_2 $(m^2.W^{-1})$	Q_{avg}	P_{th} (mW)	Ref
Si	3.47	5×10^{-18}	5.9×10^5	3.1	[21]
AlGaAs	3.3	2.6×10^{-17}	10^5	3	[34]
AlGaAs	3.3	2.6×10^{-17}	10^6	0.036	[35]
AlGaAs	3.3	2.6×10^{-17}	2.6×10^6	0.023	[14]
GaP	3.3	3.5×10^{-18}	2×10^5	3	[36]
AlN $\chi^{(2)}$	2.12	XX	4.16×10^5	12	[37]
AlN $\chi^{(3)}$	2.12	2.3×10^{-19}	1.1×10^6	25	[38]
Diamond	2.4	8.2×10^{-20}	10^6	20	[39]
Si_3N_4	2.0	2.5×10^{-19}	35×10^6	0.33	[13]
SiO_2	1.45	3×10^{-20}	6.7×10^8	1.2	[40]
SiC	2.6	6.9×10^{-15}	1.8×10^5	8.5	[41]
$LiNbO_3$	2.24	1.8×10^{-19}	2.2×10^6	4.2	[42]
Hydex	1.7	1.15×10^{-19}	2.2×10^6	50	[43]

Table 1.1: Comparison between the different integrated (ring or wedge disk) OPO on different nonlinear platforms at telecom wavelength,

threshold can be reduced mainly by increasing the Q factor. Hence the material reported here were managed to lower waveguide loss. The example of SiN and AlGaAs are particularly revealing of this trend. The first demonstration of a OPO in a SiN ring resonator had a 50 mW threshold[51]. The linear losses of 0.5 dB.cm^{-1} enabled a Q factor $\approx$ 500 000. The ring had a radius of 58 μm, and a cross-section of 711$\times$ 1700 nm. Since then, the scattering losses due to the waveguide edges have been greatly reduced through an optimization of the fabrication processes. In [13], losses are reduced to 0.8 dB.m^{-1} and Q factor are increased to 35×10^6. Consequently, the threshold is 330 μW, despite the fact that the modal volume has increased (Radius of 115 μm, cross section of 730$\times$2500 nm). Let us note also that material absorption is reduced thanks to a thermal annealing around 1200 °C[52] which is not compatible with CMOS fabrication process.

An increase of the ring cross section contributes to limit the impact of roughness, hence a decrease in scattering losses. Taking advantage of the higher n_2 of material with higher refractive index such as III-V materials also requires dealing with higher losses, since scattering is proportional to the difference of

refractive indexes. In [34], an AlGaAs OPO is demonstrated in a ring with a 12.5 μm radius and a cross section of 320×630 nm. Q factor of 10^5 and $\alpha = 1.4$ dB.cm^{-1} are sufficient to allow a threshold of 3.1 mW. Reduction of the losses (through roughness reduction and different epitaxy technique) in a ring with the same radius and a similar cross section (400×700 nm) have increased the Q up to 3.5×10^6 and the threshold down to 26 μW[14]. Compared to SiN, the AlGaAs platform, thanks to a n_2 100 times larger and a tighter confinement manage to reach a threshold one order of magnitude lower, despite a Q factor ten times lower.

1.4.2 Reduction of the modal volume

This class of OPO is particularly attractive when considering Kerr comb generation. For a particular material, the OPO threshold depends on the minimum achievable losses, that is the highest Q possible. But another possibility to decrease the threshold would be to decrease the modal volume as much as possible. From this point of view, ring resonator offers limited room for improvement, because the modal volume scales inversely with the radius of the ring[53]. The strength of the interaction ultimately set by bending losses[54], as can be seen in Fig.1.6. For example, in silicon, a ring with a radius of 2 μm cannot exceed 10^6, for a modal volume 10 times higher than the diffraction limit $(\frac{\lambda}{n})^3$. More generally, due to the broadening of the amplitude of the wavevector with the decrease of the modal volume, total internal reflection conditions become harder and harder to satisfy in a wavelength-sized cavity. To further increase the light matter interaction and decrease the device footprint, a different type of confinement must be used.

1.5 Photonic crystal Cavities

1.5.1 Principle of Photonic Crystal cavities

The concept of Photonic Crystal (PhC) was introduced in 1987[55, 56]. It is based on a periodic modulation of the refractive index that opens a photonic bandgap (PBG) in the dispersion diagram of a photonic structure. This phenomenon

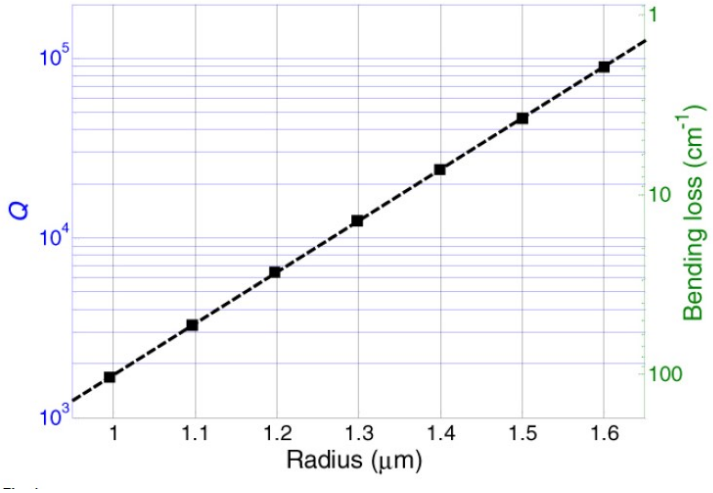

Figure 1.6: A fundamental limit for ring resonator is set by the bending losses that limit the minimal radius[54]

is analogous to electrons in a solid crystal, which see a periodic modulation of the electric potential due to the crystal lattice. A consequence of the PBG is that light cannot propagate within a certain range of frequencies and wavevector. Since the first demonstrations of PhC at optical wavelength in semiconductors[57, 58], they have been used in various areas in optics such as electrically pumped laser[59], all optical switching[11] or optomechanics[60]. A detailed study of PhC properties can be found in various textbook[61, 62], and we will simply here address qualitatively the effect a periodic modulation with a lattice a of the dielectric constant ϵ. This condition is written $\epsilon(\mathbf{r}) = \epsilon(\mathbf{r} + ma)$ where m is an integer. According to the Bloch-Floquet theorem, this discrete translational symmetry imposes an electromagnetic field solution of the form:

$$\mathbf{E_k}(\mathbf{r}) = E_0 e^{ik\mathbf{r}} \mathbf{u_k}(\mathbf{r}) \tag{1.17}$$

where k is the wavevector and $\mathbf{u_k}$ is a periodic function with the same period a than ϵ. The resulting field is a plane wave modulated by this periodic function, called a Bloch state. Consequently, all Bloch states with a k-vector equal to $k + m\frac{2\pi}{a}$ are indistinguishable, and have the same frequency $\omega(k) = \omega(k + m\frac{2\pi}{a})$. The dispersion diagram is periodic with the reciprocal lattice $\frac{2\pi}{a}$. Hence, the study of the dispersion of PhC can be restricted in the first Brillouin zone, corresponding to a k-vector between $-\frac{\pi}{a} < k < \frac{\pi}{a}$ in 1D. The opening of the bandgap for a 1D photonic crystal can be understood intuitively. A refractive index modulation leads to the diffraction of a propagating wave inside the PhC. At the Brillouin

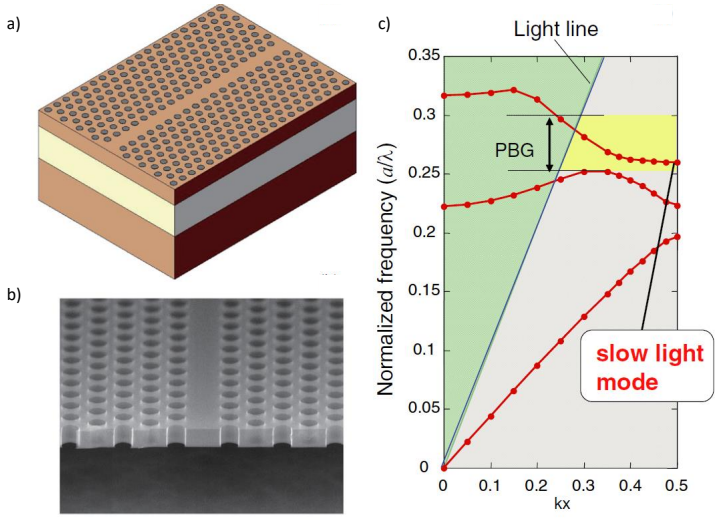

Figure 1.7: a)Schematic of a single hole line defect (W1) waveguide b) SEM picture of his waveguide made in Si. c) Corresponding dispersion relation where one can see the light line that delimits the light cone (green zone), the PBG (yellow zone) and the mode defects (red lines) with slow light modes near the band edge. From [28]

zone boundaries, there is a coupling between the wave propagation at ($k = \pi/a$) and ($k = \text{-}\pi/a$). It results in a splitting in frequency of this degenerate state, that opens a bandgap. The strongest is the modulation of ϵ (hence the variation of the refractive index n), the larger is the PBG. Low energy modes are concentrated in high index layer, they are in the dielectric band. On the opposite, higher energy mode are concentrated in the low index layer: this is the air band.

If PhC were originally thought in 3D [63], the current state of the research provides much more examples of 2D and 1D PhC. The reason is a simpler fabrication by using conventional semiconductor technologies such as lithography and pattern transfer via etching process. 2D PhCs consist in a slab patterned with holes.The slab is often suspended in air. Light confinement is ensured by a PBG in the plane of the slab, by total internal reflection in the vertical direction. 1D PhCs called nanobeam, consist in a ridge waveguide drilled with holes. Light confinement is ensured by a PBG in the propagation direction of the waveguide, and by total internal reflection in the two transverse directions. To stay confined, the Bloch state must now satisfy the Snell-Descartes relation. The range of confined modes are delimited by the so-called light-line $\omega = ck_{||}/n$

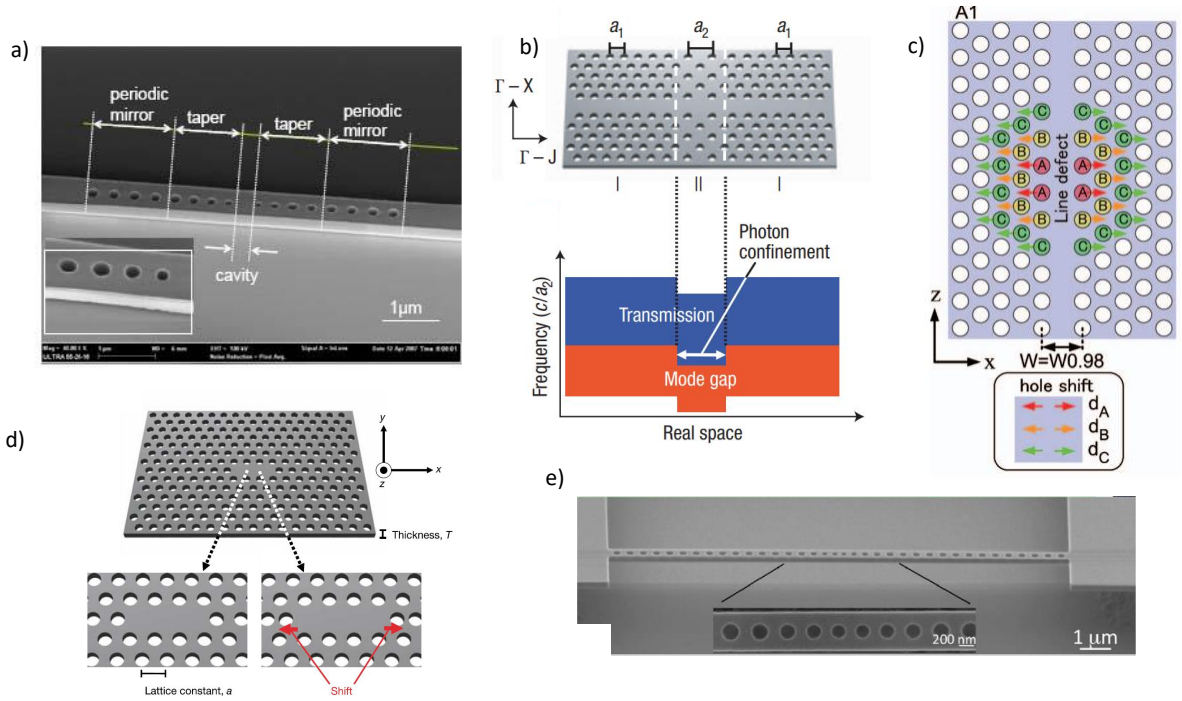

Figure 1.8: a)1D nanobeam with a point defect[64] and d) 2D L3 modified cavity d)[65] b)[66] c) [67] are mode gap 2D cavities. e) represents a nanobeam with non point defect but with a distributed mirror all along the ridge waveguide[68]

where $k_{||}$ is the in-plane component of k. Modes with a k-vector above the light line can radiate freely and will leak outside the PhC structure.

If a defect is inserted in the PhC, it will scatter or localize the Bloch state. If a line of holes is removed from a 2D-PhC slab, it will create a line defect photonic crystal waveguide[69].These waveguides offer particular interest with slow light propagation, because the group velocity $v_g = \frac{d\omega}{dk}$ tends to zero close to the band edge, where the dispersion curve is flattened[70]. Slow light propagation with $v_g = c/30$ have been demonstrated[71], and can be used to enhance Kerr nonlinearity[72].

A PhC cavity is created by inserting an artificial defect in the periodic modulation of the dielectric constant[73]. Contrary to PhC waveguide which are line defects, cavities are point defects. This defect can be as small as the diffraction limited volume $(\frac{\lambda}{2n})^3$. This properties gives to the PhC cavities the smallest mode volume when compared to other cavities with dielectric material. A cavity can be created by removing a certain number of holes in a perfectly periodic PhC either 2D[65] or 1D[74] (see Fig1.8a. and d.). In this case, a taper zone

must be added to adapt progressively the mode profile at the waveguide-mirror interface[75, 76]. In 2D slab, it is also possible to create a cavity from a photonic crystal waveguide by shifting some specific holes toward the PhC region[66, 67]. This affects the transmission of the PhC waveguide locally, in a so called photonic double heterostructure, as can be seen in Fig.1.8b) and c).
Record high Q factor up to 1.1×10^7 have been demonstrated 2D silicon PhC[77]. A strong confinement in a small volume is appealing for nonlinearities. In [78], a lithium niobate 1D PhC cavity have been achieved with a Q = 1.4×10^6 in a modal volume as low as 0.78 $(\frac{\lambda}{n})^3$. As a result the resonance could be tuned via the thermo-optic effect at telecom frequency with an efficiency of 88.4 MHz for a single photon in the cavity. It is straightforward to conclude that this combination of high Q and small volume should be suited for nonlinear application such a FWM.

1.5.2 Photonic crystal cavities for nonlinear optics

PhC cavities have been used to demonstrate various nonlinear device like Raman lasing[79]. Nonlinear frequency conversion in PhC is mostly studied with $\chi^{(2)}$ processes such as second harmonic generation and sum frequency generation. A broad variety of material have been used such as III-V semiconductors (GaP[80, 81], GaAs[82, 83], GaN[84]), Si[85], Lithium Niobate[86], SiC[87, 88] and SiN[89]. It shows the interest that PhC cavities are arousing for nonlinear optics, thanks to the combination of high Q and ultra small modal volume. However, all these studies showed relatively low nonlinear efficiencies. Indeed, the major limitation with PhC cavities comes from the difficulty to engineer the dispersion of the cavity. Contrary to ring resonator where the dimensions of the waveguide dictates the dispersion curve, PhC Bloch mode structure is much more complex.
Still, triply resonant FWM were observed in coupled PhC cavities in 1D[90] and 2D[91, 92], whose performance are summed up in Table1.2. The approach of [90] relies on the coupling of identical PhC cavities and exploits the splitting of the resonances that appears (see Fig1.9a). It allowed to demonstrate - 55 dB of conversion efficiency with 60 μW on chip power. However, the cavities were not exactly similar, hence FWM could only be achieved with low Q factor (Q $\approx$ 9000): a large resonance linewidth is needed to compensate for imperfectly aligned triplet.

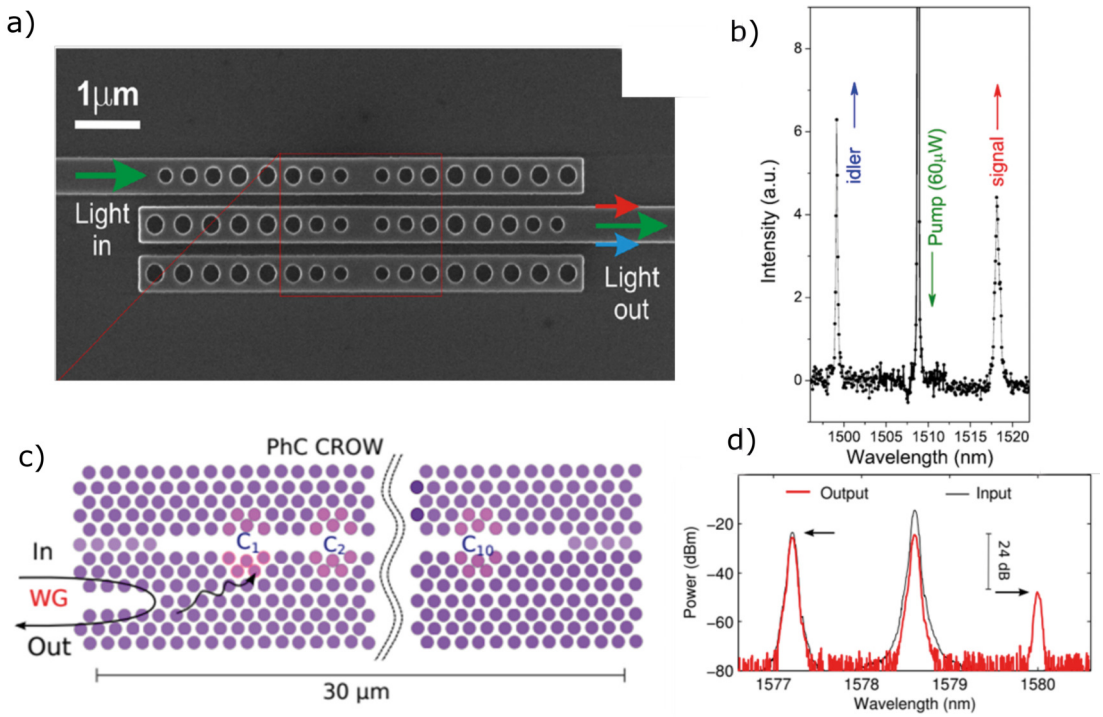

Figure 1.9: a)Coupled cavities of 1D Si-nanobeam and corresponding spontaneous FWM from [90] and b) InGaP CROW of ten resonators that enabled -24 dB nonlinear conversion from[92]

This approach was pushed further in[91] where a coupled resonator optical waveguide (CROW) constituted of more than 200 resonators was used. Nonlinearity here is enhanced through a slow light effect[3] The very high quality factor (Q $\approx$ 600 000) could compensate for the increased modal volume (V scales with the number of resonators). Still, the nonlinear efficiency was hindered by the misalignment of the resonances: - 35 dB for 100 μW on chip power. A CROW was also used in [92] to increase the efficiency up to -24 dB with 36 μW (see Fig1.9b). The improvement, despite a much lower Q, is due to the use of InGaP instead of Si (inhibiting TPA) and a much lower number of cavities (10) that decreased the modal volume.

It is interesting to note that the use of coupled PhC cavities, while resulting in limited nonlinear efficiency, was carried out on devices with a very small footprint, down to $\approx 5\ \mu m^2$ in Ref. [90].

[3]Strictly speaking, the CROW involves strongly delocalized coupled modes than can be interpreted as slow modes

Geometry	Material	Q_{avg}	On Chip power (μW)	η_{NL} (dB)	Ref.
1D PhC (3 coupled cavities)	Si	4000	60	-55	[90]
2D PhC CROW	Si	600 000	100	-35	[91]
2D PhC CROW	InGaP	70 000	36	-24	[92]

Table 1.2: *Comparison of continuous wave FWM nonlinear efficiency conversion in PhC cavities. (CROW: Coupled Resonators Optical Waveguide)*

1.5.3 The role of structural disorder

In fact, the control of the frequency of resonances in PhC is ultimately limited by structural disorder. This disorder is an imperfection in the periodicity of the PhC that occurs during the fabrication. Even in state of the art PhC cavities, this small geometrical fluctuations lead to a non negligible deviation on the resonant frequency as well as on the Q factor by inducing scattering. For example, in Si 2D-PhC, the sidewall roughness was evaluated by SEM to be around nanometers[93]. Disorder is modelled as a variation on the position or the radius of the holes[94, 95]. It was found that PhC are extremely sensitive to disorder, as irregularities of 1 nm can induce more than 100 GHz of uncertainties in the resonant frequency. In state-of-the art PhC, The average deviation from the targeted frequency is at best around 40 GHz[96], and the deviation of the spacing between two frequencies is 28 GHz[97]. Besides, the alignment of three resonances is increasingly challenging with the Q factor, because a narrow linewidth decreases the FWM bandwidth. This disorder-induced misalignment makes almost impossible to have a PhC cavity that satisfies the triply resonant condition for high Q modes without an additional tuning mechanism. Such a study have been carried out in InGaP 2D PhC, where the individual control of the resonances of the CROW is demonstrated using an holographic projection on top of the structure[98, 99]. This patterned laser locally heats the resonators to tune their eigenfrequencies. However, no nonlinear experiment using this technique have been reported.

Conclusion

In this chapter, the objective was to introduce all the necessary notions to understand the context of this work. The issue we try to address in this work is:

why are PhC cavities, despite having high Q/V performance, are not used for the FWM experiment ? We have seen that the problem does not come from the choice of material neither from structural losses, because very high Q factors have been demonstrated in a wide range of material. The problem comes from the dispersion engineering, which is much more complicated than in WGM and ring resonators. As a result, only those type of microcavities have been used to demonstrated integrated OPO. Resonant FWM in PhC have not proven to be efficient yet, because of the difficulty to align three modes in a equally spaced triplet. For all these reasons, the possibility of a PhC OPO was considered theoretically more than a decade ago[100, 101], but the demonstration is extremely challenging.

Chapter 2

Model for Parametric interaction in multi-mode cavities

Light interaction in a cavity filled with a nonlinear medium and coupled with a external waveguide is modeled with the Temporal Coupled Mode Theory (TCMT). Based on general principles such as energy conservation and time-reversal symmetry, this theory provides a powerful formalism regardless of the complexity of the geometry of the system[102]. This approach relies on a perturbative treatment of the cavity electromagnetic field and allows to obtain analytical solutions to the Maxwell equations. Hence, the variety of phenomena described ranges from optical switching to complex geometry of coupled cavities, lasing and nonlinear optics.

In this chapter, we use TCMT to describe the evolution of the electric field inside what will be our PhC cavity, starting from the linear description of a simple cavity coupled to a waveguide. We will add the contribution of the Kerr effect and thermal nonlinearity to derive the Four Wave Mixing efficiency and parametric threshold. Raman and Brillouin nonlinearities are not included in this model because they are not resonantly enhanced in the PhC cavities considered.

2.1 Properties of a cavity in the linear regime

2.1.1 Modal structure: spatial problem

Classical Maxwell equations describe the evolution of the electromagnetic field in a dielectric cavity with a relative permittivity ϵ_r:

$$\nabla \times \mathbf{E}(\mathbf{r},t) = -\mu_0 \partial_t \mathbf{H}(\mathbf{r},t) \tag{2.1}$$

$$\nabla \times \mathbf{H}(\mathbf{r},t) = \partial_t \mathbf{D}(\mathbf{r},t) \tag{2.2}$$

The electric displacement is defined by the constitutive relation:

$$\mathbf{D}(\mathbf{r},t) = \epsilon_0 \mathbf{E}(\mathbf{r},t) + \mathbf{P}(\mathbf{r},t) \tag{2.3}$$

The electromagnetic modes of a linear resonant structure are generally defined using time-harmonic solutions of Maxwell equations:

$$\mathbf{E}(\mathbf{r},t) = \tilde{\mathbf{E}}(\mathbf{r},\omega) e^{\imath\omega t} \tag{2.4}$$

The position dependant term $\tilde{\mathbf{E}}(\mathbf{r},\omega)$ is solution of the wave equation obtained from the Maxwell equations:

$$\nabla \times \nabla \times \tilde{\mathbf{E}}(\mathbf{r},\omega) - \frac{\omega^2}{c^2} \epsilon_0 \epsilon_r(\mathbf{r},\omega) \tilde{\mathbf{E}}(\mathbf{r},\omega) = 0 \tag{2.5}$$

The relative permittivity $\epsilon_r(\mathbf{r},\omega)$ is space and frequency dependent. We consider here a cavity which defines a finite domain. With such boundaries conditions, Eq.(2.5) has discrete solutions. The resonant frequencies are the eigenvalues of the wave equations, the resonant modes are the eigenmodes. The discrete structure of the eigenvalues gives the discretized spectrum of the cavity. For an isolated system, the wave equation is Hermitian with real eigenvalues. Its eigenvectors - the cavity modes - form an orthogonal basis for the total electric field which can be conveniently written as a sum of the different resonant modes contribution. Such an ideal lossless case is characterized perfectly defined resonant frequency, with an infinitely narrow linewidth.

2.1.2 Temporal Coupled Mode Theory

Temporal coupled mode theory is used to describe the electromagnetic modes of a structure with dissipation, nonlinearity and external coupling. In this work, we apply it for a resonant cavity but it can also be used with waveguides. In the

formalism of TCMT, the mode structure is describe by normal modes.
Let us start with the simplest case of a lossless single mode cavity, whose resonant field writes:

$$\mathbf{E}(\mathbf{r},t) = ae^{\imath\omega_0 t}\mathbf{e}(\mathbf{r}) \tag{2.6}$$

Here, ω_0 is the resonant pulsation of the field. a is the complex amplitude of the mode. $\mathbf{e}(\mathbf{r})$ describes the spatial distribution inside the cavity. The link with the time harmonic representation above is $\tilde{\mathbf{E}}(\mathbf{r},\omega) \approx a\mathbf{e}(\mathbf{r})$ and the spatial vector $\mathbf{e}(\mathbf{r})$ is solution normalized with the condition:

$$\frac{\epsilon_0}{2}\int_V \epsilon_r |\mathbf{e}(\mathbf{r})|^2 d^3\mathbf{r} = 1 \tag{2.7}$$

As a result, the energy of the mode[1] can be calculated by integration of the electromagnetic energy density over the volume of the mode:

$$U = \int_V \epsilon_0\epsilon_r \frac{|\mathbf{E}|^2}{2} dV = |a|^2 \tag{2.8}$$

For a lossless isolated cavity, the energy inside the cavity is constant and the evolution of the field is:

$$\partial_t \mathbf{E} = \imath\omega_0\mathbf{E} \tag{2.9}$$

$$\mathbf{E}(\mathbf{r},\mathbf{t}) = \sqrt{U}e^{\imath\omega_0 t}\mathbf{e}(\mathbf{r}) \tag{2.10}$$

This expression is exact for an isolated system, and the complex envelope a is constant. For a multimode cavity, the total electric field is the superposition of the different normal modes that form a set of orthogonal vectors:

$$\mathbf{E}(\mathbf{r},t) = \sum_{-n}^{n} a_n e^{\imath\omega_n t}\mathbf{e_n}(\mathbf{r}) \tag{2.11}$$

with the normalization condition being:

$$\frac{\epsilon_0}{2}\int_V \mathbf{e}^*_\mathbf{m}(\mathbf{r})\epsilon_r\mathbf{e_n}(\mathbf{r})d^3\mathbf{r} = \delta_{m,n} \tag{2.12}$$

where $\delta_{m,n}$ is the Kronecker delta. This normalization keeps the energy of each mode at $U_n = |a_n|^2$.

[1]Since the cavity size is larger than the diffraction limit, the mode is very well spatially localized. The electric and magnetic energy density are equal: $\epsilon|\mathbf{E}|^2/4 = \mu|\mathbf{B}|^2/4$

2.1.3 Introduction of losses

So far, the cavity that we have described is perfectly isolated, meaning no exchange of energy outside its boundaries. In absence of losses, the time evolution of the cavity field is unitary[103]. As a consequence, its eigenmodes form an orthogonal basis. The introduction of losses raises the issue that the operator becomes non unitary and the modes inside the cavity are decomposed on a non-orthogonal basis[104]. A rigorous approach would require quasi-normal modes[105] with complex eigenfrequencies. However, because we will treat losses with a perturbative approach, the modes will still be approximated by a set of normal modes that do not couple with each other. Losses will be included in the complex amplitude that becomes time dependant, $a \rightarrow a(t)$ with a temporal dependence much slower than ω_0. The quality factor measures the ratio of the stored energy over the dissipated energy in one cycle. Consequently, the value of Q factor is a direct figure of merit of this approximation compared to a isolated system, where Q is infinite. In the case of $Q > 10^4$ which corresponds to the experimental values here, the cavity is weakly coupled to the outside and we can keep a normal mode structure for the cavity.

Fig.2.1 shows a representation of the cavity coupled to an external waveguide. There is no particular assumption made over the geometry of the cavity itself. We see that losses can have two origins: internal losses that includes dissipation and radiation, and coupling to an external port.
Internal losses to the cavity (absorption, out-of-plane scattering..) are modeled with a decay rate Γ related to the intrinsic Q factor: $\Gamma = \omega/Q_0$ with a decay time τ_0.
Coupling loss to an external port are modeled with a decay rate κ related to the coupling Q factor: $\kappa = \omega/Q_c$ with a decay time τ_c. The cavity-waveguide scheme can allow multiple decaying ports. If the cavity is symmetric regarding all the coupling ports - which will always be the case here -, they will be all considered identical and independent. This simply means that the same coupling constant will be multiplied by the number of coupling channels in the equation. Fig.2.1a) and b) shows the example of a resonator coupled with one or two ports. Different configuration are possible but only these two will be experimentally realized in this work.
Finally, the external port can also feed the cavity with an incoming wave noted

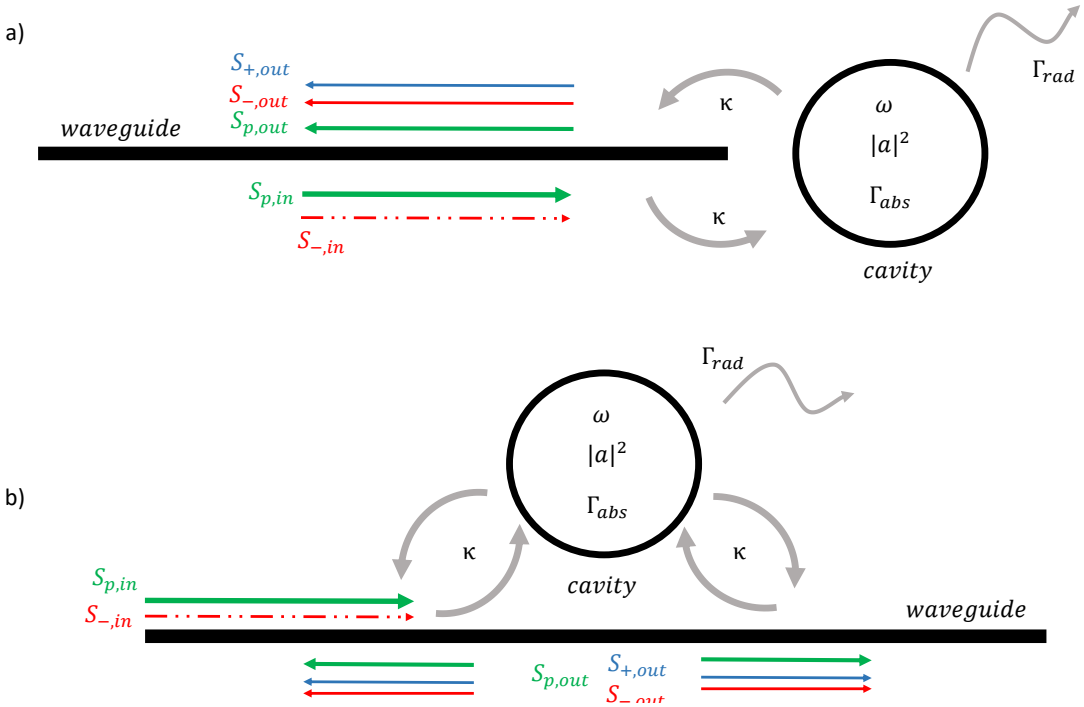

Figure 2.1: a) Representation of a resonator coupled to a single-ended waveguide in the time-dependent coupled mode theory with the definition of the field in the waveguide s and in the cavity a, internal Γ_{abs} and radiation loss Γ_{rad} and waveguide coupling κ. b) Same resonator in a different coupling scheme with two different decaying ports.

s, normalized so that $|s|^2$ represents the power of this wave. One can note that a power normalization was not appropriate for the cavity modes as they can be (and actually, in the case of PhC, are) standing waves. The energy conservation and time reversal principles dictate that the coupling of s is equal to $\imath\sqrt{\kappa}$[102]. The frequency of s can be out of resonance, with a detuning $\delta = \omega_s - \omega_0$ lower than the resonance linewidth.

In the single ended configuration shown in Fig.2.1a) , the cavity has only one port connected to the outside. The equation of the evolution of the intra-cavity field for the $m-th$ mode is now:

$$\partial_t(\mathbf{E}\cdot\mathbf{e_m}) = \imath\omega_m(\mathbf{E}\cdot\mathbf{e_m}) - \frac{\Gamma_0+\kappa}{2}(\mathbf{E}\cdot\mathbf{e_m}) + \imath\sqrt{\kappa}e^{\imath\omega_s t}s_m \tag{2.13}$$

The evolution of the envelope for each mode is obtained by developing equation (2.13):

$$\partial_t a_m = -\frac{\Gamma_0+\kappa}{2}a_m + \imath\sqrt{\kappa}e^{\imath\delta_m t}s_m \tag{2.14}$$

The losses and coupling that we have added are responsible for the time dependence of a which is not constant. This equation does not include any phase term in ω because we stated that the evolution of a was much slower in a perturbative approach. In order to remove the exponential term in the equation, we can chose to reference the fields in the frame of the external laser, $\mathbf{E} = a(t)e^{-\imath\delta_m t}e^{-\imath\omega_s t}$. Hence, we can rewrite this equation by setting $a(t) \to a(t)e^{-\imath\delta_m t}$. It reads:

$$\partial_t a_m = (-\imath\delta_m - \frac{\Gamma_0+\kappa}{2})a_m + \imath\sqrt{\kappa}s_m \tag{2.15}$$

As expected in the frame of the laser, it is the amplitude a_m that is phase-shifted by $-\delta_m$ which is also very small compared to ω_m.

2.2 Model of a cavity in the nonlinear regime

The equation Eq. (2.15) describe the evolution of the amplitude of modes that is a set of independent equations. The nonlinear polarization adds a term that couples these equations. We are now going to provide an explicit definition of this term.

2.2.1 Nonlinear polarization

In order to derive the nonlinear polarization perturbation in the model, we start from the Maxwell equations Eqs(2.1) to obtain:

$$\nabla \times \nabla \times \mathbf{E} = -\mu_0 \partial_t^2 \mathbf{D} \tag{2.16}$$

. The linear part of the polarisation is separated from higher order terms in the constitutive relation(2.3), rewritten

$$\mathbf{D} = \epsilon_0 \epsilon_r \mathbf{E} + \mathbf{P_{NL}} \tag{2.17}$$

where $\epsilon_r = (1 + \chi^{(1)})$ is a tensor that takes into account the linear polarization under the assumption that the material is isotropic and has an instantaneous response.

In absence of nonlinear polarization and losses, the amplitude of the electric field a is constant as it represents a linear combination of normal modes. The second order derivative of $\mathbf{E}$ is:

$$\partial_t^2 \mathbf{E} = \sum_n -\omega_n^2 a e^{\imath \omega_n t} \mathbf{e_n}(\mathbf{r}) \tag{2.18}$$

Injected in Eq. (2.16) and given that the $\mathbf{e_n}$ are orthogonal , we retrieve the linear wave equation with the notations of TCMT:

$$[\nabla \times \nabla \times \mathbf{e_n}(\mathbf{r}) - \omega_n^2 \mu_0 \epsilon_0 \epsilon_r \mathbf{e_n}(\mathbf{r})] = 0 \tag{2.19}$$

We see here the practicality of TCMT that allows to treat separately the spatial and temporal part of the field. The wave equation translates into a condition on each vector $\mathbf{e_n}$.

The nonlinear term in TCMT equations is derived as a first order perturbation of normal modes. The amplitude of the field $a(t)$ is now time dependant. The second order derivative of $\mathbf{E}$ becomes:

$$\partial_t^2 \mathbf{E} = \sum_n (\partial_t^2 a_n + 2\imath\omega_n \partial_t a_n - \omega_n^2 a_n) e^{\imath \omega_n t} \mathbf{e_n}(\mathbf{r}) \tag{2.20}$$

The injection in Eq.(2.16) leads to :

$$\begin{aligned} \nabla \times \nabla \times \left[\sum_n a_n(t) e^{\imath \omega_n t} \mathbf{e_n}(\mathbf{r}) \right] = \\ - \mu_0 [\epsilon_0 \epsilon_r \sum_n (\partial_t^2 a_n + 2\imath\omega_n \partial_t a_n - \omega_n^2 a_n) e^{\imath \omega_n t} \mathbf{e_n}(\mathbf{r}) + \partial_t^2 \mathbf{P_{NL}}] \end{aligned} \tag{2.21}$$

which can be recast into:

$$\sum_n a_n e^{\imath\omega_n t}[\nabla\times\nabla\times\mathbf{e_n}(\mathbf{r}) - \omega_n^2\mu_0\epsilon_0\epsilon_r\mathbf{e_n}(\mathbf{r})] = \\ -\mu_0\epsilon_0\epsilon_r\sum_n(\partial_t^2 a_n + 2\imath\omega_n\partial_t a_n)e^{\imath\omega_n t}\mathbf{e_n}(\mathbf{r}) - \mu_0\partial_t^2\mathbf{P_{NL}} \quad (2.22)$$

On the left hand side, we recognize the linear wave equation (2.19) which is equal to zero. We also make the assumption that the amplitudes $a(t)$ are slowly varying compared to the optical frequency ω. This is justified because the bandwidth of the resonance, information carried in $a(t)$, is narrow enough to separate its evolution from the carrier frequency in TCMT formalism. Mathematically, this condition writes $|\partial_t^2 a| << |\omega\partial_t a| << |\omega^2 a|$, or slowly varying envelope approximation (SVEA).
In the equation Eq. (2.22), when the linear part vanishes, we only keep the lowest order terms, meaning that we can neglect the contribution of the second order derivative $\partial_t^2 a$.
Eq. (2.22) with only first order terms becomes:

$$\partial_t^2\mathbf{P_{NL}} = -\epsilon_0\epsilon_r\sum_n(2\imath\omega_n\partial_t a_n)e^{\imath\omega_n t}\mathbf{e_n}(\mathbf{r}) \quad (2.23)$$

We now integrate on the volume of the cavity mode. The integration over the volume affects only the terms depending on the spatial coordinate $\mathbf{r}$, i.e. the vectors $\mathbf{e_n}(\mathbf{r})$. We also project on the $m-th$ mode by multiplying $\mathbf{e_m^*}(\mathbf{r})$. It yields:

$$\int_V \mathbf{e_m^*}(\mathbf{r})\cdot\partial_t^2\mathbf{P_{NL}}dV = -\sum_n\left[(2\imath\omega_n\partial_t a_n)e^{\imath\omega_n t}\int_V \mathbf{e_m^*}(\mathbf{r})\epsilon_0\epsilon_r\mathbf{e_n}(\mathbf{r})dV\right] \quad (2.24)$$

On the right hand side, we recognize the normalization condition Eq.(2.12). Hence, we derived the nonlinear contribution to the polarization of the $m-th$ mode:

$$\partial_t a_m = \imath\frac{e^{-\imath\omega_m t}}{4\omega_m}\int_V \mathbf{e_m^*}(\mathbf{r})\cdot\partial_t^2\mathbf{P_{NL}}dV \quad (2.25)$$

We can also inject this expression in the equation ((2.15))of the evolution of the field envelope with the addition of the nonlinear term:

$$\partial_t a = (-\imath\delta_0 - \frac{\Gamma_0+\kappa}{2})a + \imath\sqrt{\kappa}s + \imath\frac{e^{-\imath\omega_m t}}{4\omega_m}\int_V \mathbf{e_m^*}(\mathbf{r})\cdot\partial_t^2\mathbf{P_{NL}}dV \quad (2.26)$$

2.2.2 Nonlinear cross section and coupling coefficient

The next step is to express the term $\mathbf{P_{NL}}$ as a function of the cavity parameters. We are considering the nonlinear polarization induced by Kerr effect. Due to symmetry considerations, most of the elements of the $\chi^{\mathbf{3}}$ are vanishing. In Ref.[8], all the nonzero elements of $\chi^{(\mathbf{3})}$ tensor contributing to the nonlinear refractive index are expressed. It gives the following expression, for an isotropic material and a nonlinearity induced by nonresonant electronic response[2]:

$$\mathbf{P_{NL}} = n_2 \epsilon_r \epsilon_0^2 c_0 \frac{2(\mathbf{E}\cdot\mathbf{E}^*)\mathbf{E} + (\mathbf{E}\cdot\mathbf{E})\mathbf{E}^*}{3} \tag{2.27}$$

We now multiply it by $\mathbf{E}^*$ to have the same form as in Eq.(2.25):

$$\mathbf{P_{NL}}\cdot\mathbf{E}^* = n_2 \epsilon_r \epsilon_0^2 c_0 \frac{2|\mathbf{E}|^4 + |\mathbf{E}\cdot\mathbf{E}|^2}{3} \tag{2.28}$$

.

In order to facilitate the interpretation of the calculus, we start by considering a single mode cavity, where the electric field writes like in Eq.(2.6). The only nonlinearity possible is SPM, and we assume that the polarization has an harmonic dependence in ω. We substitute the equation Eq.(2.28) in Eq.(2.25).

$$\begin{aligned}
\partial_t a &= \imath \frac{e^{-\imath\omega t}}{4\omega} \int_V \mathbf{e}^*(\mathbf{r})\cdot\partial_t^2 \mathbf{P_{NL}} dV \\
&= \imath \frac{e^{-\imath\omega t}}{4\omega} \int_V \mathbf{e}^*(\mathbf{r})\cdot(-\omega^2 \mathbf{P_{NL}}) dV \\
&= -\imath \frac{\omega e^{-\imath\omega t}}{4} \int_V \frac{e^{\imath\omega t}}{a^*} \mathbf{E}^*\cdot\mathbf{P_{NL}} dV \\
&= -\imath \frac{\omega}{4} \int_V n_2 \epsilon_r \epsilon_0^2 c_0 \frac{2|\mathbf{e}(\mathbf{r})|^4 + |\mathbf{e}(\mathbf{r})\cdot\mathbf{e}(\mathbf{r})|^2}{3} dV |a|^2 a
\end{aligned}$$

We expressed the nonlinear term as a function of the complex amplitude a and the energy of the mode $|a|^2$. We can rewrite this equation into:

$$\partial_t a = \imath\gamma |a|^2 a \tag{2.29}$$

where we have introduced the parameter γ

$$\gamma = -\frac{c_0 n_2 \omega}{\epsilon_r V_\chi} \tag{2.30}$$

[2]Chapter 4 equation (4.2.10) and (4.2.13b) of Ref.[8]

and defined the nonlinear interaction volume as :

$$\frac{1}{V_\chi} = \frac{\epsilon_r^2 \epsilon_0^2}{4} \int_V \frac{2|\mathbf{e}(\mathbf{r})|^4 + |\mathbf{e}(\mathbf{r}) \cdot \mathbf{e}(\mathbf{r})|^2}{3} dV \tag{2.31}$$

Written under this form, the impact of the $\chi^{(3)}$ nonlinearity is easily interpreted as a frequency shift proportional to the mode energy $|a|^2$. We have derived the expression that corresponds to the SPM under the CMT formalism. The strength of SPM is also proportional to the material nonlinearity n_2 and inversely proportional to the nonlinear volume V_χ. Let us also note that γ is a complex number that takes into account the nonlinear absorption. In absence of TPA, the term $\gamma|a|^2$ can be simply interpreted as an effective detuning caused by SPM.

We are now going to derive the expression for the parametric process involving several modes. We describe the case of a cavity with 4 modes, which corresponds to the case of non-degenerate FWM. The intra-cavity field is the superposition of 4 resonant field, as in Eq. ((2.11)) with n = 4. For each mode m, we now have to evaluate the product $\mathbf{P_{NL}} \cdot \mathbf{e_m^*}$. It yields:

$$\begin{aligned} P_{NL} \cdot {\mathbf{e_m}}^* = n_2 \epsilon_r \epsilon_0^2 c_0 \\ [A_m |a_m|^2 + \sum_{m \neq n} 2B_{m,n} |a_n|^2 + 2C_{m,n,l,k} a_n^* a_l a_k e^{\imath(\omega_l + \omega_k - \omega_n)t}] \end{aligned} \tag{2.32}$$

with

$$\begin{aligned} A_m &= \frac{2|\mathbf{e}_m|^4 + |\mathbf{e}_m \cdot \mathbf{e}_m|^2}{3} \\ B_{m,n} &= \frac{2|\mathbf{e}_n|^2 |\mathbf{e}_m|^2 + |\mathbf{e}_n \cdot \mathbf{e}_m|^2}{3} \\ C_{n,m,l,k} &= \frac{2(\mathbf{e}_n^* \cdot \mathbf{e}_l)(\mathbf{e}_m^* \cdot \mathbf{e}_k) + (\mathbf{e}_n^* \cdot \mathbf{e}_m^*)(\mathbf{e}_l \cdot \mathbf{e}_k)}{3} \end{aligned}$$

We recognize in the frequency matching term of the FWM in the exponential. We set this frequency mismatch as:

$$2\Delta_{FWM} = \omega_l + \omega_k - \omega_m - \omega_n \tag{2.33}$$

Following the same development as before, we now insert this expression in Eq. (2.25) to obtain the nonlinear contribution:

$$\begin{aligned} \partial_t a_m = -\imath \gamma_m |a_m|^2 a_m - \imath \sum_{m \neq n} 2\gamma_{m,n} |a|_n^2 a_m + \\ - 2\gamma_{m,n,l,k} a_n^* a_l a_k e^{2\imath \Delta_{FWM} t} \end{aligned} \tag{2.34}$$

This equation has three different terms corresponding to the SPM, XPM and FWM with the the corresponding nonlinear parameters, γ_m, $\gamma_{m,n}$, $\gamma_{m,n,l,k}$ defined as follows;

$$\gamma_{xx} = \frac{c_0 n_2 \omega}{\varepsilon_r V_{\chi,xx}} \tag{2.35}$$

where the nonlinear volumes $V_{\chi,xx}$ are defined as

$$\begin{aligned}
\frac{1}{V_{\chi,n}} &= \frac{\varepsilon_0^2 \varepsilon_r^2}{4} \int_V \frac{2|\mathbf{e}_n|^4 + |\mathbf{e}_n \cdot \mathbf{e}_n|^2}{3} dV \\
\frac{1}{V_{\chi,n,m}} &= \frac{\varepsilon_0^2 \varepsilon_r^2}{4} \int_V \frac{2|\mathbf{e}_n|^2|\mathbf{e}_m|^2 + |\mathbf{e}_n \cdot \mathbf{e}_m|^2}{3} dV \\
\frac{1}{V_{\chi,n,m,l,k}} &= \frac{\varepsilon_0^2 \varepsilon_r^2}{4} \int_V \frac{2(\mathbf{e}_n^* \cdot \mathbf{e}_l)(\mathbf{e}_m^* \cdot \mathbf{e}_k) + (\mathbf{e}_n^* \cdot \mathbf{e}_m^*)(\mathbf{e}_l \cdot \mathbf{e}_k)}{3} dV
\end{aligned}$$

2.3 Resonant FWM in a cavity

2.3.1 Master Equation

We can now establish the master equation by adding to Eq.(2.15) the contribution of the Kerr effect. When the cavity is pumped, the resonance frequency is detuned from the cold cavity by thermal change of the refractive index. The thermo-optic effect adds to the SPM and XPM in the detuning of the cavity. In the frame of the laser field, all these contributions are included in a single effective detuning that shifts the cold resonance ω_m to its hot value, $\omega_{m,h}$. The detuning of the cavity is discussed more in detail in the next section.
The master equation yields:

$$\partial_t a_m = (-\imath\delta_{m,h} - \frac{\Gamma_m + \kappa_m}{2}) a_m + \imath\sqrt{\kappa_m} s_m - 2\gamma_{m,n,l,k} a_n^* a_l a_k \tag{2.36}$$

where we have set $\delta_{m,h} = \omega_s - \omega_{m,h}$. The phase-matching term in the FWM term is canceled here because we must do the substitution $a_m \rightarrow a_m e^{-\imath\delta_m t}$ in order to be in the frame of the laser.

The derivation of the master equation including Kerr nonlinearity is consistent with Ref.[101, 106].
This expression is valid for the case of a 4 modes resonator. It implies no cascading effects are considered. As shown in Fig.2.2a), the two pump modes are labelled $a_{p,1}$ and $a_{p,2}$. The Stokes and anti-Stokes modes are labelled a_- and a_+ respectively. In the undepleted pump approximation, we have $|a_{p,1}|, |a_{p,2}| >> |a_+|, |a_-|$.

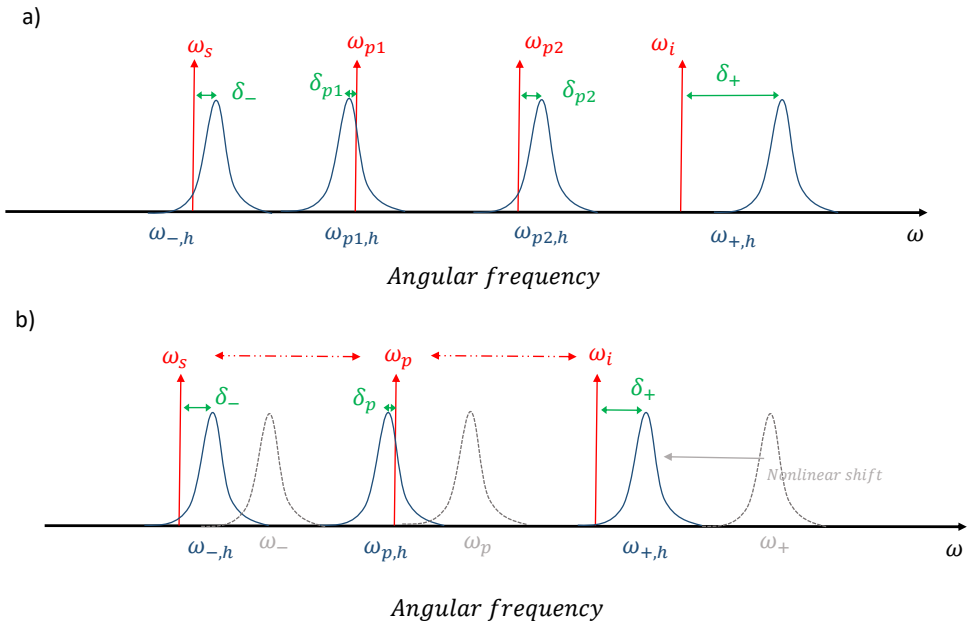

Figure 2.2: a)Non degenerate FWM in cavity. The "hot" resonances of the pumped cavity are modeled by the blue Lorentzian. The red arrows are the frequencies involved in FWM. They are detuned by δ, and perfectly resonant when $\delta = 0$. b) Degenerate FWM. Signal and idler are symmetric with respect to the pump so the cavity resonances must be equispaced too. In dotted grey line, the cold cavity resonances are shown. They have all shifted due to the nonlinearity, each by a different quantity, which implies that the dispersion of the "hot" cavity is different than the "cold" case.

2.3.2 Detuning of the cavity by thermo-optic effect

In the model, the cavity resonances and FWM fields are detuned. Intuitively, one would say that the efficiency of the FWM process should occur when the pump, signal and idler are perfectly resonant. However, it is important to be clear on which detuning we are referring to prevent any confusion.

- Firstly, the cavity mismatch $\Delta\omega_h$ represents the frequency misalignment of the cavity resonances. The FSR of the cavity are equal when $\Delta\omega_h = 0$. The cavity mismatch stems from the sum of two contributions: $2\Delta\omega_h = \Delta\omega_{cold} + \Delta\omega_{NL}$ where $\Delta\omega_{cold}$ is the original misalignment of the cavity (equivalent to the first order dispersion) and $\Delta\omega_{NL}$ is the contribution of the nonlinearities, namely SPM, XPM and thermo-optic effect: $\Delta\omega_{NL} = \Delta\omega_{Kerr} + \Delta_{Thermal}$. At steady state, the thermo-refractive effect induces a much stronger detuning than SPM or XPM (around 2 orders of magnitude higher in PhC cavities). We have already derived the contribution of the Kerr nonlinearity. We now introduce formally the thermo-optic effect which is expressed as:

$$\Delta\omega_{NL} \approx \Delta_{Thermal} = \sum_{i,j} = \alpha_{i,j}\sigma_j|a_j|^2 \tag{2.37}$$

  where $\alpha_{i,j} = \frac{\partial\omega_{h,i}}{\partial|a_j|^2}$ are the thermo-optic coefficients that represent the thermal influence of the j_th mode on the $i-th$ mode. The coefficients σ_j are chosen for a red-detuning induced by the thermo-optic (equal to 1 or -1). Let us note that in this model, each loaded mode influences the other modes differently. The coefficients $\alpha_{i,j}$ is close to unity when the spatial overlap between the two considered modes is large. But in the general case, different coefficient for each pair of modes are required. It is particularly true in the case of PhC where the distribution of the modes is inhomogeneous compared to ring resonator for example. In rings, all the thermo-optic can be approximated equal at first order due to a much better overlap between the modes.

  We neglect the influence of the signal and idler waves on the thermo-optic effect that we assume being only induced by the pump. Under the later assumption, and in the case of degenerate FWM that we will consider later on, the frequency mismatch can be expressed in a simpler form:

$$2\Delta\omega_h = \Delta\omega_{cold} + (2\alpha_{p,p} - \alpha_{p,+} - \alpha_{p,-})|a_p|^2. \tag{2.38}$$

- Secondly, we have the detuning of the FWM fields with their respective cavity resonances, denoted $\delta = \omega - \omega_h$. When the pump frequency is set, δ_+ and δ_- are not independent because they are linked to the frequency mismatch of the hot cavity $2\Delta\omega_h = \omega_{h,p1} + \omega_{h,p2} - \omega_{h,+} - \omega_{h,-}$. We can inject this result in the expression of δ_+:

$$\delta_+ = 2\Delta\omega_h + \delta_{p,1} + \delta_{p,2} - \delta_- \tag{2.39}$$

2.3.3 Undepleted pump approximation

In FWM experiments, the pump beam is generally much stronger than the generated idler and signal. The undepleted pump approximation is valid in the case of a strong continuous pump and low parametric gain. Under these assumptions, the FWM term can be neglected for the pump field. It is possible to explicit it and inject the expression in the equation of the signal and idler.
The master equations for the pump becomes :

$$\partial_t a_p = (-\imath\delta_{p,h} - \frac{\Gamma_p + \kappa_p}{2})a_p + \imath\sqrt{\kappa_p}s_p \tag{2.40}$$

At steady state ($\partial_t a_p = 0$), the pump is constant and the solution of this equation is:

$$a_p(t) = \sqrt{\frac{4\kappa_p}{(\Gamma_p + \kappa_p)^2 + 4\delta_p^2}P_p} = \sqrt{U_p} \tag{2.41}$$

with $U_p = |a_p|^2$ the energy stored in the cavity, and P_p the pump power.

The pump beams can be different (non degenerate FWM). We now insert these expressions of $a_{p,1}$ and $a_{p,2}$, with the energy $U_{p,1}$ and $U_{p,2}$ in the master equation (Eq.(2.36)) for the signal and idler:

$$\begin{aligned}
\partial_t a_+ &= (-\imath\delta_{+,h} - \frac{\Gamma_+ + \kappa_+}{2})a_+ + \imath\sqrt{\kappa_+}s_+ - 2\gamma_{FWM}\sqrt{U_{p,1}U_{p,2}}a_-^* \\
\partial_t a_- &= (-\imath\delta_{-,h} - \frac{\Gamma_- + \kappa_-}{2})a_- + \imath\sqrt{\kappa_-}s_- - 2\gamma_{FWM}\sqrt{U_{p,1}U_{p,2}}a_+^*
\end{aligned} \tag{2.42}$$

This system can be recast with the matrix notation:

$$\partial_t \begin{bmatrix} a_- \\ a_+^* \end{bmatrix} = \begin{bmatrix} -\imath\delta_- - \frac{\Gamma_- + \kappa_-}{2} & -\imath\chi \\ \imath\chi^* & \imath\delta_+ - \frac{\Gamma_+ + \kappa_+}{2} \end{bmatrix} \begin{bmatrix} a_- \\ a_+^* \end{bmatrix} + \begin{bmatrix} \imath\sqrt{\kappa_-}s_- \\ -\imath\sqrt{\kappa_+}s_+^* \end{bmatrix} \tag{2.43}$$

where we have introduced the parametric gain

$$\chi = 2\gamma_{FWM}\sqrt{U_{p,1}U_{p,2}} \tag{2.44}$$

From the expression of U_p, let us note that the parametric gain χ reaches a maximum when the pump fields are at resonance that is when $\delta_{p,1} = \delta_{p,2} = 0$.

2.4 Degenerate FWM: spontaneous and stimulated FWM

2.4.1 Degenerate FWM for PhC cavities

So far, we have considered the general case of FWM where the two pump beams are different. We are now going to restrict the study to the degenerate FWM where the two pump photons have the same frequency that is $\omega_{p,1} = \omega_{p,2} = \omega_p$, as shown in Fig.2.2b),. It would be possible to carry on the derivation in the non degenerate regime at the cost of bulkier notations. Moreover, the model presented here is developed with the idea to apply it to PhC cavities. For example, the assumption to neglect the Kerr phase shift over thermal effects is not appropriate for ring resonators. PhC cavities support Bloch modes assimilated to standing waves. Hence, the parity of two successive modes is different and the integral of the overlap expressed in V_χ is close to 0. For this reason, non-degenerate FWM is not likely to occur in PhC. We will now deal with degenerate FWM even if the reasoning is exactly the same for the non-degenerate case. However, due to the degeneracy of the pump field, the parametric gain loses its factor 2 to become:

$$\chi = \gamma_{FWM}U_p \tag{2.45}$$

2.4.2 Parametric oscillation

We start with the case of spontaneous FWM. The matrix defined in Eq.(2.43) gives the condition for parametric oscillation. As in Ref.[31], the onset of hyper-parametric oscillation is given when the determinant of this matrix is null. This determinant is:

$$\mathcal{D} = \left(-\imath\delta_- - \frac{\Gamma_- + \kappa_-}{2}\right)\left(\imath\delta_+ - \frac{\Gamma_+ + \kappa_+}{2}\right) - |\chi|^2 \tag{2.46}$$

The matrix is singular when $\mathcal{D} = 0$. Projecting on the real and imaginary part, we have the set of equations:

$$\frac{(\Gamma_- + \kappa_-)(\Gamma_+ + \kappa_+)}{4} + \delta_-\delta_+ - |\chi|^2 = 0 \tag{2.47}$$

$$\frac{\delta_-(\Gamma_+ + \kappa_+)}{2} - \frac{\delta_+(\Gamma_- + \kappa_-)}{2} = 0 \tag{2.48}$$

To solve this system, we must add the fact that δ_+ and δ_- are not independent. In the case of degenerate FWM, the expression of Eq.(2.39) becomes $\delta_+ = 2\Delta\omega_h + 2\delta_p - \delta_-$. It gives:

$$\delta_- = \left(1 + \frac{\Gamma_+ + \kappa_+}{\Gamma_- + \kappa_-}\right)^{-1} (2\Delta\omega_h + 2\delta_p) \tag{2.49}$$

$$\delta_+ = \left(1 + \frac{\Gamma_- + \kappa_-}{\Gamma_- + \kappa_+}\right)^{-1} (2\Delta\omega_h + 2\delta_p) \tag{2.50}$$

With this, it is possible to express the parametric gain χ as a function of the cavity properties:

$$|\chi|^2 = \frac{(\Gamma_+ + \kappa_+)(\Gamma_- + \kappa_-)}{(\Gamma_- + \kappa_- + \Gamma_+ + \kappa_+)^2} (2\Delta\omega_h + 2\delta_p)^2 + \frac{(\Gamma_+ + \kappa_+)(\Gamma_- + \kappa_-)}{4} \tag{2.51}$$

In order to simplify the notation, we assume that $\Gamma_+ = \Gamma_-$ and $\kappa_+ = \kappa_-$, which turns the equation into:

$$|\chi|^2 = \frac{(\Gamma_- + \kappa_-)^2}{4} + (\Delta\omega_h + \delta_p)^2 \tag{2.52}$$

The parametric gain χ was originally defined as a function of the energy stored in the pump mode. We remind that in the case of degenerate FWM, $\chi = \gamma_{FWM} U_p$. We are now able to express the pump power P_{th} that is necessary to reach the threshold of the cavity:

$$|\chi|^2 = |\gamma_{FWM} \frac{4\kappa_p}{(\Gamma_p + \kappa_p)^2 + 4\delta_p^2} P_{th}|^2 = \frac{(\Gamma_- + \kappa_-)^2}{4} + (\Delta\omega_h + \delta_p)^2 \tag{2.53}$$

Developing and rearranging of the terms gives:

$$P_{th} = \frac{(\frac{(\Gamma_- + \kappa_-)^2}{4} + (\Delta\omega_h + \delta_p)^2)^{1/2}}{4\kappa_p} \frac{(\Gamma_p + \kappa_p)^2 + 4\delta_p^2}{|\gamma_{FWM}|} \tag{2.54}$$

We just need to express the nonlinear parameter as a function of the cavity characteristics. For that, we remind that the definition of this parameter for

FWM is : $\gamma_{FWM} = \frac{c_0 n_2 \omega_p}{\epsilon_r V_{FWM}}$. The expression of the cavity power threshold for non triply resonant FWM is :

$$P_{th} = \frac{\epsilon_r |V_{FWM}|}{c_0 n_2 \omega_p}((\Gamma_p + \kappa_p)^2 + 4\delta_p^2)\frac{(\frac{(\Gamma_- + \kappa_-)^2}{4} + (\Delta\omega_h + \delta_p)^2)^{1/2}}{4\kappa_p} \tag{2.55}$$

Finally, it is interesting to consider the case where the cavity is actually triply resonant, which gives the lowest possible threshold. This implies that the cavity detuning $\Delta\omega_h = 0$ and that all the fields are resonant $\delta = 0$. The expression of P_{th} takes the form :

$$P_{th} = \frac{\epsilon_r |V_{FWM}|}{8 c_0 n_2 \omega_p}\frac{(\Gamma_- + \kappa_-)(\Gamma_p + \kappa_p)^2}{\kappa_p} \tag{2.56}$$

We can also relate the threshold to the quality factor as this is the value that is commonly measured in microcavities $Q = \omega/(\Gamma + \kappa)$:

$$P_{th} = \frac{\epsilon_r |V_{FWM}|}{8 c_0 n_2}\frac{Q_{c,p}}{Q_p^2 Q_-}\omega_- \tag{2.57}$$

where $Q_{c,p}$ is coupling Q of the pump and Q_-, Q_p are the loaded Q factor of the signal (supposed equal to the idler) and pump respectively. The dependence in ω_- is due to the fact that we have counted the modes "+" and "-" indifferently, which stands for close frequencies. In fact, the threshold depends on the geometric average of the frequencies, that is the one of the pump.

2.4.3 Stimulated FWM

In this section, we will consider the case of stimulated FWM. We assume that a signal laser is seeded in the mode ω_-. The system of equation is completely symmetrical so the reasoning holds exactly the same if we had chosen to seed mode ω_+. We must now take into account the vector $\begin{bmatrix} \imath\sqrt{\kappa_-}s_- \\ 0 \end{bmatrix}$ in Eq.(2.43). We solve this equation at steady state to express the nonlinear efficiency of the stimulated FWM. This translates into:

$$(-\imath\delta_- - \frac{\Gamma_-\kappa_-}{2})a_- - \imath\chi a_+^* + \imath\sqrt{\kappa_-}s_- = 0 \tag{2.58}$$

$$(\imath\delta_+ - \frac{\Gamma_+\kappa_+}{2})a_+^* - \imath\chi^* a_- = 0 \tag{2.59}$$

We are interested in the efficiency, so it is logical to express the ratios of the intra-cavity field over the signal seed:

$$\frac{a_-}{s_-} = -\sqrt{\kappa_-}\left(\delta_+ + \imath\frac{\Gamma_+ + \kappa_+}{2}\right)\frac{1}{\mathcal{D}} \tag{2.60}$$

$$\frac{a_+^*}{s_-^*} = \frac{\chi^*\sqrt{\kappa_-}}{\mathcal{D}} \tag{2.61}$$

where $\mathcal{D}$ is the same determinant of the matrix of the system defined in the previous section. In the frame of TCMT, the fields going out of the cavity are given by : $s_{out} = s_{in} + \imath\sqrt{\kappa}a$. Dividing this relation by s_- for the modes $(+,-)$ gives:

$$\frac{s_{out,-}}{s_-} = 1 - \kappa_-\left(\imath\delta_+ - \frac{\Gamma_+ + \kappa_+}{2}\right)\frac{1}{\mathcal{D}} \tag{2.62}$$

$$\frac{s_{out,+}^*}{s_-^*} = -\imath\frac{\chi^*\sqrt{\kappa_-\kappa_+}}{\mathcal{D}} \tag{2.63}$$

To have the nonlinear efficiency, we must now take the modulus square of these equation because the quantity $|s|^2$ is normalized as a power quantity. Taking $\Gamma_+ = \Gamma_-$ and $\kappa_+ = \kappa_-$ with all fields resonant ($\delta = 0$) gives a simpler form:

$$\eta_{FWM} = \frac{|s_{o,+}|^2}{|s_-|^2} = \frac{|\chi|^2\kappa_+^2}{[|\chi|^2 - (\Gamma_+ + \kappa_+)^2/4]^2} \tag{2.64}$$

It is also possible to stay in the general case with detuned fields and choose to consider the low parametric gain regime A more general yet simple expression for the conversion efficiency is given in the limit of low parametric gain ($\lim_{\chi\to 0}$). This regime is well below the threshold of oscillation, meaning that the expression will be less and less accurate with growing conversion efficiency. Ruling out at the first order the terms in $|\chi|$ yields

$$\eta_{FWM} = \frac{|\chi|^2\kappa_-\kappa_+}{[(\Gamma_- + \kappa_-)^2/4 + \delta_-^2]\,[(\Gamma_+ + \kappa_+)^2/4 + \delta_+^2]} \tag{2.65}$$

As we proceeded for the power threshold, we can now link η_{FWM} with the pump power through the parametric gain $\chi = \gamma_{FWM}U_p$. Defining the Lorentzian function as $\mathcal{L}(x) = 1/(1+x^2)$, Eq.(2.65) can be rewritten as

$$\eta_{FWM} = \left[\frac{c_0 n_2 \omega}{\varepsilon_r |V_\chi|}\right]^2 \frac{\kappa_p^2}{4(\Gamma_p + \kappa_p)^4}\frac{\kappa_-\kappa_+}{(\Gamma_- + \kappa_-)^2(\Gamma_+ + \kappa_+)^2}P_p^2$$
$$\mathcal{L}\left(\frac{2\delta_p}{(\Gamma_p + \kappa_p)}\right)^2 \mathcal{L}\left(\frac{2\delta_-}{(\Gamma_- + \kappa_-)}\right)\mathcal{L}\left(\frac{4\delta_p + 4\Delta_\chi - 2\delta_-}{(\Gamma_+ + \kappa_+)}\right) \tag{2.66}$$

The nonlinear efficiency has been written as a product of several terms: a coefficient that depends on the cavity geometry and material, a second term that account for the quality factor of the cavity and the coupling efficiency and the last part is the product of three Lorentzian that account for the resonant enhancement of the FWM. Only this last part changes with the respective detunings of the pump, probe and cavity. As expected, the conversion efficiency reaches a maximum when all the detunings $\delta = 0$ are zero, which corresponds again to the triply resonant cavity ($\Delta\omega_h = 0$).

$$\eta_{FWM,max} = \left[\frac{c_0 n_2 \omega}{\varepsilon_r |V_\chi|}\right]^2 \frac{\kappa_p^2}{4(\Gamma_p + \kappa_p)^4} \frac{\kappa_+ \kappa_-}{(\Gamma_- + \kappa_-)^2 (\Gamma_+ + \kappa_+)^2} P_p^2 \tag{2.67}$$

2.4.4 Relation between stimulated and spontaneous emission

Spontaneous emission corresponds spontaneous FWM under oscillation threshold. When the resonator is driven under threshold, only the pump mode is excited from a semi-classical standpoint. However, the quantum fluctuations in the side modes allow spontaneous generation. Hence a rigorous approach requires a full quantum description.

Spontaneous emission being interpreted as a stimulated emission triggered by vacuum fluctuations has been derived in the case of ring resonators and waveguides[107]. This link is particularly interesting because spontaneous FWM can be characterized via stimulated FWM, the latter being easier to observe experimentally at low efficiencies. The average generated power associated with one photon of each pair is defined as a function of the power circulating in the structure and the field enhancement factor. Unfortunately, the results of Ref.[107] are not strictly adapted in the context of standing waves resonators such as PhC because there is no clear definition of field enhancement factor, as the field is strongly inhomogenous in the cavity and there is neither a clear definition of circulating power. However, if we assume a generalization of this interpretation, it yields in Ref.[107]:

$$P_{SPE,0} = \hbar\omega \int_\omega \eta_{FWM} d\omega \tag{2.68}$$

where P_{SPE} is the power associated with spontaneous emission of one side mode that is coupled out in the waveguide. It corresponds to the integral over the cavity resonance of the probability of stimulated parametric conversion η_{FWM}

defined in Eq. 2.62.

This expression has been derived in the limit of a strongly over-coupled cavity, meaning that the cavity internal losses are neglected. As a result, any generated pair is coupled out. The purpose of this section is to modify the equation to account for internal cavity losses. First, we note that the total power loss rate P_t of a given mode of the cavity is, by definition $P_t = (\Gamma + \kappa)|a|^2$ .The power associated with the coupling is $P_c = \kappa|a|^2$, the power dissipated is $P_d = \Gamma|a|^2$.

.

Hence, the fraction of the total power coupled out to the waveguide is then:

$$\frac{P_c}{P_t} = \frac{\kappa|a|^2}{(\Gamma + \kappa)|a|^2} = \frac{\kappa}{\Gamma + \kappa}$$

Unfortunately, we cannot apply it directly to Eq.2.68 because we cannot define an internal power in cavities with standing modes. Experimentally, we have access to the *external* conversion efficiency, defined as:

$$\eta_{FWM} = \frac{P_{+,out}}{P_{-,in}} \tag{2.69}$$

where we assume that the signal laser is set on the mode (-). When there is no internal losses, all the photons are coupled to the waveguide and none is lost for detection. It means that the *internal* and *external* conversion efficiencies are equal. Hence, it corresponds to the limit case where, for a total loss rate unchanged, $(\Gamma+\kappa) \to \kappa_0$ where κ_0 defines entirely the linewidth of the resonance. At resonance, in the case of the PhC cavity coupled to a single waveguide , the signal energy stored is

$$|a|^2 = \frac{4\kappa}{(\Gamma + \kappa)^2} P_{in}$$

while the idler power radiated from the cavity to the waveguide is still $P_c = \kappa|a|^2$. In the absence of internal loss, we have an optimal conversion efficiency:

$$\eta_0 = \kappa_{0,+}|a_+|^2 \frac{4\kappa_{0,-}}{\kappa_{0,-}^2|a_-|^2} = \frac{4\kappa_{0,+}|a_+|^2}{\kappa_{0,-}|a_-|^2}$$

In the case internal losses are not negligible, instead:

$$\eta_{FWM} = \frac{4\kappa_-\kappa_+|a_+|^2}{(\Gamma_- + \kappa_-)^2|a_-|^2}$$

Dividing the two equations and taking $(\Gamma + \kappa) = \kappa_0$ leads to

$$\eta_{FWM} = \eta_0 \frac{\kappa_+\kappa_-}{(\Gamma_+ + \kappa_+)(\Gamma_- + \kappa_-)} \tag{2.70}$$

Thus, the *internal* conversion efficiency can be deduced from the measurement of the *external* conversion efficiency. Now, the rate of generated signal and idler photon which are coupled to the waveguide is related to the total rate of generated pairs:

$$\begin{aligned} P_+ &= \frac{\kappa_+}{\Gamma_+ + \kappa_+} P_{SPE,0} \\ P_- &= \frac{\kappa_-}{\Gamma_- + \kappa_-} P_{SPE,0} \end{aligned} \tag{2.71}$$

where $P_{SPE,0}$ is defined in eq.(2.68).Reformulated with the external stimulated emission, it yields:

$$\begin{aligned} P_+ &= \frac{\Gamma_- + \kappa_-}{\kappa_-} \hbar\omega_+ \int \eta_{FWM} d\omega \\ P_- &= \frac{\Gamma_+ + \kappa_+}{\kappa_+} \hbar\omega_- \int \eta_{FWM} d\omega \end{aligned} \tag{2.72}$$

We see that the power associated with spontaneous emission, in the case of lossy cavity, is multiplied by an escape efficiency term, which is specific to the mode. The escape efficiency accounts for the fact that the power transferred in the sideband is partly coupled to the waveguide and the rest is dissipated. This relation generalizes the results of Ref.[107]. Although the formalism to derive this equation used was not adapted for our type of cavities, it provides a great insight on the physical interpretation of each term. On the other hand, we will see in the next section that this relation still stands, although re-derived through another method.

2.4.5 Quantum model for Spontaneous Emission

In this section, we present the derivation of Eq.2.72 that is rigorously valid for our type resonators. It relies on the quantization of the TCMT model that we have developed in this chapter. We show that it matches the generalized result of Ref.[107] that we just derived in the previous section.

In ref.[108], the spectral density of the output of the spontaneous photon flux is calculated using Quantum Langevin equations. The master equation is canonically quantized by replacing the complex amplitude with annihilation and creation operators, $\hat{a}$ and $\hat{a}^\dagger$. Vacuum fluctuations are added through vacuum operators $\hat{V}_\Gamma$ and $\hat{V}_\kappa$ associated with the intrinsic and coupling losses. Then, the time-domain equations for the quantum fluctuations are Fourier transformed in order to deduce the power spectra of the side modes. With our notation and

coupling scheme, the equation of the quantum fluctuations for the signal and idler modes writes[3]

$$\partial_t \begin{bmatrix} \delta\hat{a}_- \\ \delta\hat{a}_+^\dagger \end{bmatrix} = \begin{bmatrix} -\imath\delta_- - \frac{\Gamma_- + \kappa_-}{2} & -\imath\chi \\ \imath\chi^* & \imath\delta_+ - \frac{\Gamma_+ + \kappa_+}{2} \end{bmatrix} \begin{bmatrix} \delta\hat{a}_- \\ \delta\hat{a}_+^\dagger \end{bmatrix} + \begin{bmatrix} \imath(\sqrt{\kappa_-}\hat{V}_{\kappa,-} + \sqrt{\Gamma_-}\hat{V}_{\Gamma,-}) \\ -\imath(\sqrt{\kappa_+}\hat{V}_{\kappa,+}^\dagger + \sqrt{\Gamma_+}\hat{V}_{\Gamma,+}^\dagger) \end{bmatrix} \tag{2.73}$$

We apply now the Fourier transform to this system in order to have the equations in the spectral domain. Finally, knowing that the output field $\hat{s}_{out}$ is:

$$\hat{s}_{out} = \imath\sqrt{\kappa}\hat{a} - \hat{V}_\kappa \tag{2.74}$$

we can calculate the spectral density of the output photon flux in each mode:

$$S_{SPE}(\omega) = \langle \delta\hat{s}_{out}(\omega)\delta\hat{s}_{out}^\dagger(\omega)\rangle \tag{2.75}$$

$$= (\Gamma + \kappa)\kappa\frac{|\chi|^2}{|\mathcal{D}|^2} \tag{2.76}$$

with

$$\mathcal{D} = (\Gamma + \kappa)^2/4 - |\chi|^2 - \delta^2 \tag{2.77}$$

We retrieve the modulus square of Eq.(2.62) which corresponds in the case where the detunings and loss rates are equal: $\delta_+ = \delta_-$, $\Gamma_+ = \Gamma_-$, $\kappa_+ = \kappa_-$:

$$\eta_{FWM} = \frac{|s_{out,+}|^2}{|s_-|^2} = \kappa^2\frac{|\chi|^2}{|\mathcal{D}|^2} = \frac{\kappa}{\kappa + \Gamma}S_{SPE}(\omega) \tag{2.78}$$

Using the Parseval theorem, we can derive the output power of the output photon rate $R_{SPE,+}$ by integrating the spectral density, (here for the mode (+)):

$$R_{SPE,+} = \int_{\omega_+} N_{SPE}(\omega)d\omega \tag{2.79}$$

The photon rate, expressed in Hz, is linked to the output power by the relation:

$$P_{SPE,+} = \hbar\omega_+ R_{SPE,+} \tag{2.80}$$

It yields to the relation:

$$P_{SPE,+} = \hbar\omega_+\frac{\kappa_+ + \Gamma_+}{\kappa_+}\int_{\omega_+}\eta_{FMW}d\omega \tag{2.81}$$

[3]The equivalence of notations with ref.[108] is: : $|\chi| \to g_0A_0^2$, $\kappa \to 2\kappa_t$, $\Gamma \to 2\kappa_i$ $(\Gamma+\kappa)/2 \to \kappa$ and $-\delta \to \sigma - 1/2\zeta_2 l^2 + 2\imath g_0|A_0|^2 - \omega$

We have demonstrated here that both Ref[108] and [107] lead to the same formula. As a result, it is possible to describe spontaneous emission rate as the parametric conversion of the vacuum fluctuations in the modes (+,-). The power of the spontaneous light emitted in the mode (+) is the integral of the stimulated nonlinear efficiency carried over the resonance linewidth of this mode (+) when the mode (-) is stimulated multiplied by an escape efficiency that accounts for the internal losses of the cavity.

2.5 Three Photon Absorption

Until now, we have neglected the nonlinear absorption because we have supposed that the cavity is made of a TPA-free material. The limitation of the power injected inside the cavity would then be the nonlinear absorption due to Three Photons Absorption (3PA) where three pump photons generate an electron-hole pair in the semiconductor. We derive the 3PA generation rate using the same method as in Ref.[109]. The 3PA is usually defined by the power dissipated in the cavity during the propagation:

$$\frac{dI}{dz} = -\alpha_{3PA} I^3 \tag{2.82}$$

where I is the irradiance of the beam and α_{3PA} is the 3PA coefficient expressed in (m^2/W^2). This coefficient is explicitly defined for propagating waves. In order to apply it to standing waves, we have to generalize this definition by converting it in energy units. The irradiance is related to the energy density $\mathcal{U}$ through $I = c_0\mathcal{U}/n$ in an uniform medium of index $n = \sqrt{\epsilon_r}$. The key relation here is that

$$\frac{dI}{dz} = \frac{d\mathcal{U}}{dt} \tag{2.83}$$

Replacing with the expression of 3PA gives

$$\frac{d\mathcal{U}}{dt} = -\alpha_{3PA}\mathcal{U}^3\frac{c_0^3}{n^3} \tag{2.84}$$

This equation is valid locally in any isotropic non dispersive medium. Integrating over the volume containing the cavity and using the definitions for the normal cavity modes defined before:

$$\begin{aligned}\int_V \frac{d\mathcal{U}}{dt}dV &= -\int_V \alpha_{3PA}\left(\frac{c_0\epsilon_0\epsilon_r|\mathrm{e}|^2}{2n}\right)^3 dV = \\ &= -\alpha_{3PA}\left(\frac{c_0}{n}\right)^3|a|^6\int_V \frac{\epsilon_0^3\epsilon_r^3}{8}|u|^6 dV\end{aligned}$$

where we have defined a three photon absorption volume $V_{3PA}^{-2} = \int_V \frac{\epsilon_0^3 \epsilon_r^3}{8} |u|^6 dV$. Thus we can now define a nonlinear absorption rate $\Gamma_{3PA}|a|^4$ (in Hz):

$$\frac{d|a|^2}{dt} = -\alpha_{3PA} \left(\frac{c_0}{n}\right)^3 \frac{|a|^6}{(V_{3PA})^2} = -\Gamma_{3PA}|a|^6 \tag{2.85}$$

which is rewritten as:

$$\Gamma_{3PA} = \frac{\alpha_{3PA}}{(V_{3PA})^2} \left(\frac{c_0}{n}\right)^3 \tag{2.86}$$

Conclusion

In this chapter, we have use Temporal Coupled Mode Theory to establish a model of Kerr cavities. This model makes no assumption on the geometry of the cavity itself, except for the coupling scheme which needs to be precised. As a result, it can be applied to all types of resonators including PhC cavities which differs from ring resonators by their modal structure that prohibits the notion of circulating power. Thermal nonlinearity was added but TPA was neglected. We then derived the equations of stimulated and spontaneous FWM in the case of degenerate FWM. Special care was taken in keeping different the loss rates and thermal coefficients of the modes because they can differ strongly between the modes of a PhC cavity. Without a surprise, the model predicts a maximum of efficiency for a triply resonant cavity.
The hypothesis to neglect SPM and XPM over thermal nonlinearities corresponds to the experimental situation that we will have with high-Q PhC cavities. This effect will indeed be used to align the cavity as we will demonstrate in the next chapter, meaning that all the detunings $\delta = 0$. A realistic exploitation of this analytical model requires two experimental steps:

- achieving a triply resonant PhC cavity
- a proper characterization of its characteristic: loss rates, thermal coefficients, nonlinear gain ..

In the next chapter, we will present the type of cavity that will be used and the characterization of their linear parameters. The nonlinear characterization and nonlinear experiments validating the model developed here will be in Chapter 4.

Chapter 3

Design and fabrication of PhC multi-mode cavities

In this chapter, we will describe the principle of confinement, the design and fabrication of two types of PhC microcavities. Both possess the property of having equispaced modes while having small modal volumes and ultra-high Q factors. The optical properties of the resonators will be investigated numerically in order to bring out the relevant parameters for efficient nonlinear wave mixing. We will see that remarkably, two different resonator-type with two different confinement strategies lead to the same modal structure, described by the same theoretical model.

In the first part of the chapter, we will briefly detail what are the common strategies for designing a PhC cavity. In the second and third parts, we will describe the design, fabrication and characterization of our 2D PhC and 1D PhC on insulator.

3.1 Principle of confinement: light cone and radiative modes

Theoretically, only a 3D bandgap allows a perfect confinement. 1D and 2D PhC add total internal reflection (TIR) confinement in one or two dimensions of space. This hybridisation comes with losses, because the light confined by PBG can couple into radiative modes[110]. As we explained in Chapter I, the radiative modes defines a light line above which conservative modes can exist. High index materials allow a larger number of modes below the light line, thanks to higher index contrast. Design of high Q PhC cavities comes down to reducing the out of plane losses. It was shown that the reduction of these losses can be realized by tapering the mirror region[76, 111], for example an increase in the hole radii or hole to hole distance. It realizes an engineering of the Bloch mode supported by the cavity by gradually adapting the mode profile to the evanescent mode in the perfect mirror section. With this approach, the losses of the cavity are treated as a wave impedance matching problem, with Fabry-Perot like reflections.
In the meantime, the idea of gentle confinement was introduced[65], illustrated in Fig3.1. This approach relies on computing the (spatial) Fourier components of the field inside the cavity. The losses are minimized by removing any component inside the light cone, which are the components that can couple to out-of plane radiative modes. As a result, a high Q is achieved by the shaping of the spatial envelope of the mode, and the "gentle' confinement consists in smoothing the profile of the mode so that the lowest spatial frequencies are removed. Fig3.1 illustrates this principle. On the top left, an abrupt mode profile between two perfect mirrors possess some components inside the light cone, shown on the bottom left. On the top right, an apodized mode profile suppresses the radiative components. The gentle confinement concept allowed to reach very high-Q PhC microcavities, because it gives a very simple design rule: a Gaussian-shaped mode envelope allows to achieve ultra-high Q factor. This method can be also viewed as an impedance matching in a tapered Bragg mirror[112].

Nevertheless, we can conclude that, regardless of the physical explanation that lies behind, a practical design method can be now derived for optimizing the Q factor of a PhC cavity, which is a Gaussian shaped mode envelope. We can also note that, while other spatial shapes could be used, the Gaussian function is the one minimizing both the spatial components inside the light cone and the

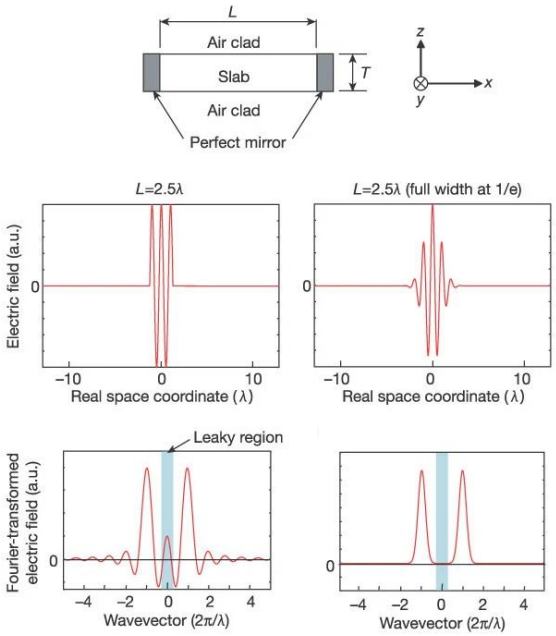

Figure 3.1: Illustration of the Gaussian apodization confinement compared to an abrupt mode profile. From [65].

mode volume.

3.1.1 Trapping light in a potential

It is of common knowledge that light confinement is difficult because a photon has no charge nor mass. Still, effective potential can be realized to confine photons. The double heterostructure cavity PhC[66, 67],is realized by manipulating the geometry of a PhCW slab. A small perturbation in the PhCW lattice is introduced, generally by slightly shifting several hole from their positions. Within the perturbed region, the PhCW modes are above the cutoff, so they propagate. However, in the unperturbed region, the PhCW modes are below the cutoff, hence evanescent. The propagating modes are therefore trapped in the perturbed regions, thanks to a shallow effective potential induced by a small variation of the cutoff frequency of the PhCW.
In 2015, Alpegigiani *et al.* introduced the concept of Bichromatic design[113]. Inspired by condensed matter theory, the Bichromatic design superimposes two periodic lattices with different constant in a PhCW slab. A drastic reduction of the radiation losses was predicted, resulting from a non trivial localization

mechanism. This is interpreted as the generation of an effective Aubry-André potential for photons, which was already observed with matter waves[114]. The first realization of this design[115], in silicon, demonstrated a cavity mode with a Q factor of 10^6. Interestingly, the mode of this cavity has a nearly perfect Gaussian envelope, with a volume that remains close to the diffraction limit.
Still, all these trapping ideas were introduced to optimize single mode cavities, and did not provide any answer for a multimodal PhC cavity with equidistant high Q modes. The next section will explain how to adapt this design to realize a PhC cavity interesting for nonlinear optics.

3.2 The bichromatic cavity for FWM

3.2.1 An optical harmonic oscillator

Prior to my arrival, our research group exploited the concept of confining potential in PhC. It was already known that the evolution of photons near the band edge is described by a Schrodinger equation[116]. They had the intuition that a Gaussian envelope of the first order mode combined with the approximately parabolic photonic band edge of a PhC could be connected to an effective parabolic potential function.

And, if the photons are trapped in a parabolic potential, it results in a system that is analogous to the quantum harmonic oscillator. The relevant property of such an optical harmonic oscillator is that its eigenmodes are equally distributed on the frequency axis, which is precisely what is needed for resonant FWM. In one dimension, the spatial envelopes of the modes are described by Hermite-Gauss (HG) functions:

$$\Psi_n(x) = \frac{1}{\sqrt{2^n n!}} \pi^{-1/4} exp(-x^2/2) H_n(x) \tag{3.1}$$

with

$$H_n(x) = n! \sum_{m=0}^{E(\frac{n}{2})} \frac{(-1)^m}{m!(n-2m)!} (2x)^{(n-2m)} \tag{3.2}$$

where n is the order of the mode, and E is the integer part function. This longitudinal mode profile is very different from microresonator relying on travelling waves, or even from standard Fabry-Perot cavities (which still involves traveling waves).
This approach can be implemented for surface photonics or bottle resonators[117,

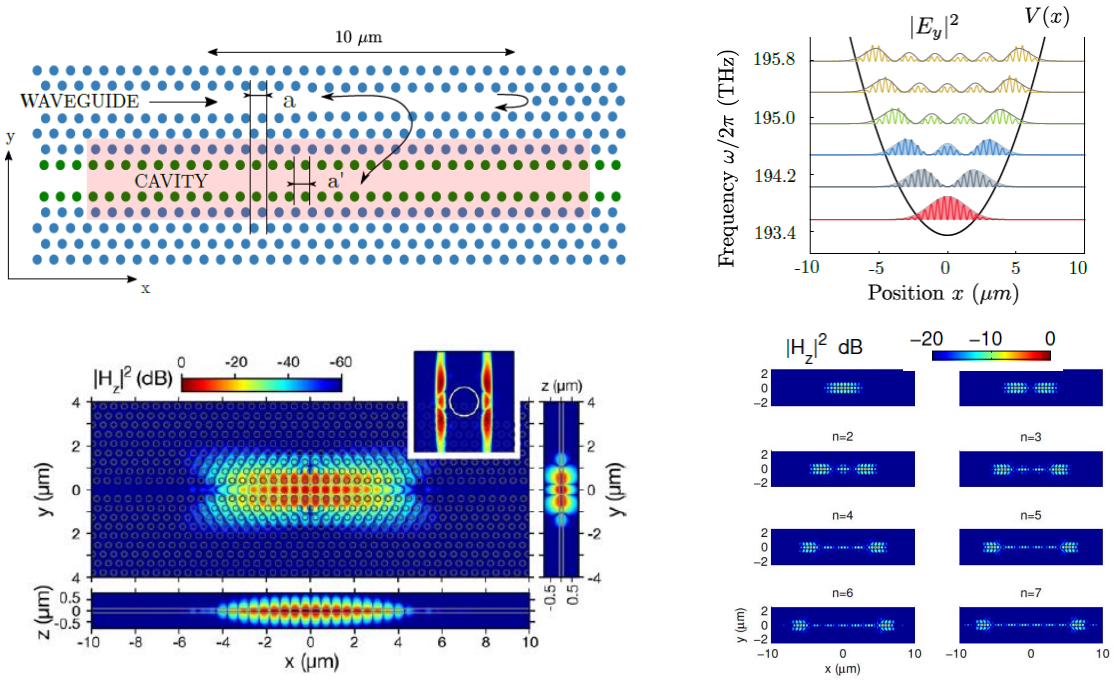

Figure 3.2: a) Schematic of the bichromatic cavity with the two different period a and a' b) calculated Hermite-Gauss modes corresponding to an effective parabolic potential for photons c) False color map of the fundamental mode calculated by FDTD along the main symmetry axis. The inset shows the reciprocal space, the white circle being the light line. From [120] d) Calculated 2D H-field intensity map for the 8 first modes, in logarithm scale.

118] where a parabolic modulation of the width of a fiber induces a parabolic potential for surface axial waves. In PhC though, the parabolic modulation occurs at a much lower spatial scale, and was introduced primarily to reduce the radiative losses, as we already discussed in the previous section. The key point here is that the potential must be deep enough to allow at least 3 different modes. A theoretical study of a parabolic modulation of the thickness of a PhC slab was also carried out[119].

3.2.2 Design of the bichromatic cavity

The study of a new bichromatic design to realize an harmonic oscillator was reported in Ref.[120]. The starting point is a missing line PhCWG slab, as shown in Fig 3.2a). second lattice is introduced by changing the period of the first rows

of the PhCWG. The resulting potential along the x-axis can be approximated by $V(x) = V_0 cos(2\pi a) + V_0 cos(2\pi a')$. In this example, the period $a = 485nm$ and $a' = 0.98a$. The radius of the holes is $r = 0.27a$ and the slab thickness is 180 nm. The cavity is fed by a PhCWG in a single ended configuration. Light that travels into the waveguide evanescently coupled to the bichromatic cavity, and then reflected back at the end of the waveguide. The end of the waveguide is terminated by a PhC reflector, with a reflectivity $\approx 100\%$ [69]. The space between the waveguide and the cavity is either 5 or 6 rows wide. The commensurability parameter, $\beta = a/a'$ is fixed. The potential width directly depends on β because the sum of cosine can be rewritten into:

$$V \propto cos(2\pi\beta x) \approx (1 - \pi\beta x^2) \tag{3.3}$$

The parameter β controls the convexity of the potential, hence the spatial extent of the confinement. Values closer to unity increase the volume of the mode, and decreases the FSR of the cavity.The value chosen here, $\beta = 0.98$ leads to a FSR around 400 GHz. The parabolic approximation tends to be less accurate with higher order mode. This anharmonicity leads to a decreasing of the mode spacing with higher order modes, calculated to be less than 10 GHz (a corrective second order term is added to the dispersion: $\Delta^2\nu = -2.69GHz$) for two consecutive FSR. Practically, this deviation is much lower than the randomness introduced during the fabrication. Figure3.2b) shows the intensity mode profile along the x-axis calculated by Finite Difference Time Domain (FDTD). Their envelope are fitted with the polynomials of Eq.3.1, in solid line with a very good agreement. This strongly suggests that the bichromatic design implements an effective harmonic photonic potential for photons, with a very close analogy to the quantum harmonic oscillator for electrons.

Figure3.2c) and d), taken from Ref.[120] show the 2D simulated map of the H_z intensity field for the fundamental mode and higher order modes respectively. An inset shows the representation in the reciprocal space, that indicates no components in the light cone. Since the first order HG mode is a pure Gaussian, the bichromatic design intrinsically lead to a minimization of the out-of-plane losses. It results in very high Q factors (simulated $Q \approx 10^7$). Interestingly, higher order HG modes do also have high Qs. The electromagnetic energy distribution is mostly concentrated in the outer lobes. The volume of the fundamental mode is close to the diffraction limit since $V_0 = 1.03 \times 10^{-19} m^3 = 0.9(\frac{\lambda}{n})^3$ at 1550 nm.

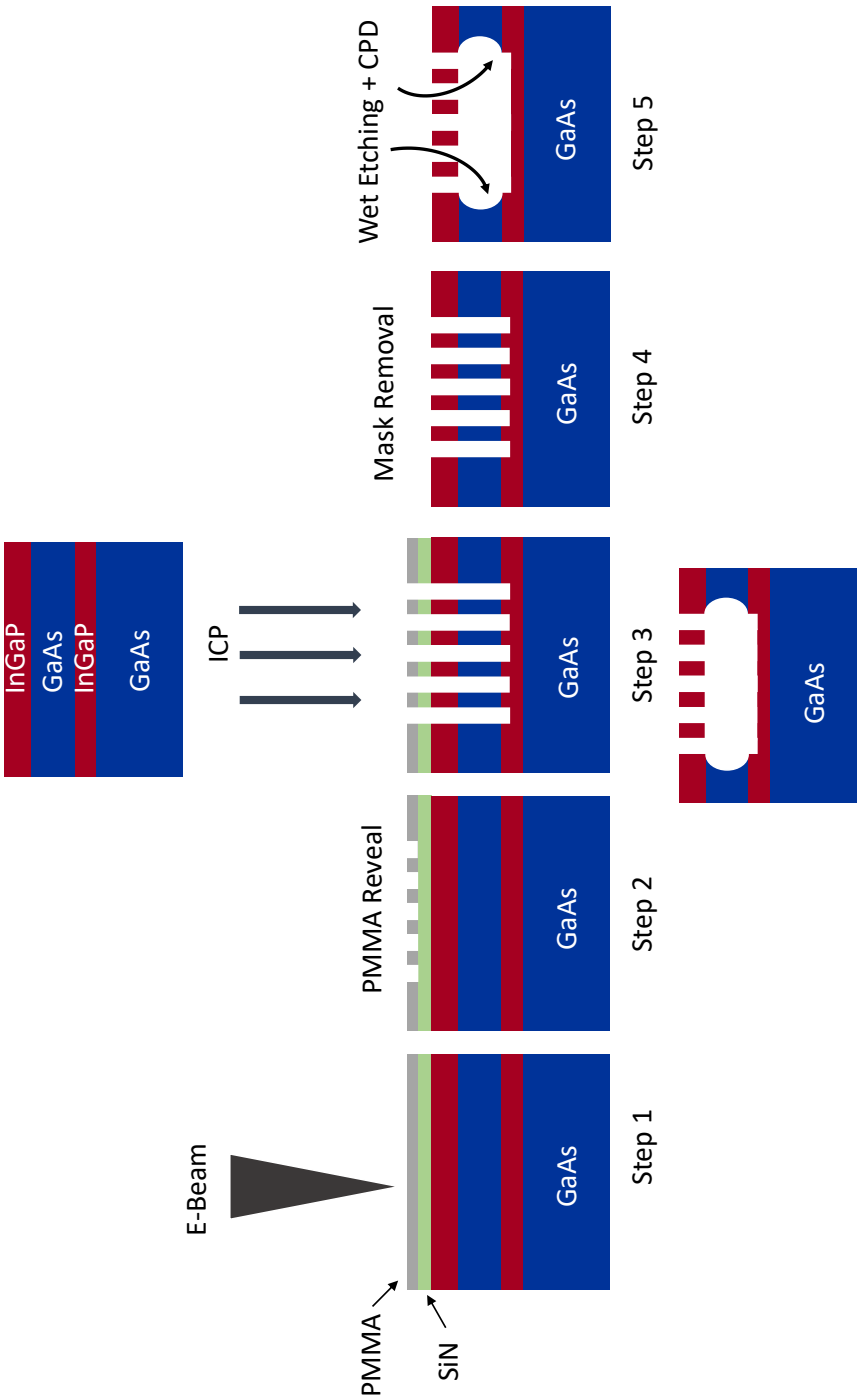

Figure 3.3: Fabrication step for the suspended membrane

3.2.3 Fabrication of the bichromatic cavity

In our configuration, the bichromatic cavity is fabricated in a suspended membrane made of InGaP. In this section, we will review the fabrication flow for achieving high quality factors in these structures. The process has been optimized in Thales for a decade, and more recently in C2N, and it was used to fabricate PhC waveguide[18, 121] and cavities[92]. The suspended membranes are made of Indium Gallium Phosphide lattice-matched to GaAs grown by MOCVD (Metalorganic Vapour Phase Epitaxy). The fabrication steps are schematized in Fig3.3.

The starting point is a InGaP/GaAs wafer stack. The intermediate InGaP layer is 200 nm thick, then there is a sacrificial GaAs layer of 1.4 microns and the final GaInP, depending on the epitaxy, is either 190 or 320 nm. The former was initially grown specifically for suspended membrane while the latter was intended for bonded structure.

The first step consists in coating a silica or silicon nitride mask on top of the InGaP of 300 nm by PECVD (Plasma-Enhanced Chemical Vapor Deposition). Then a positive resist, polymethyl-methacrylate (PMMA) is spin-coated. The PhC motive is patterned on the resist with electron beam lithography (e-beam) by a Nanobeam NB4 beamwritter .A special care is taken for the positioning of the writing field, so that the cavity is included in the same subfield to avoid any drift of the e-beam. Positive resist is used in the case of 2D photonic membrane because it limits the lithography time by writing the holes instead of the contours for a negative resist. On the other hand, it limits the resolution of the lithography to 1 nm, which is the lowest possible for PMMA before being sensitive to proximity effect.

The resist is then developed using diluted Methyl isobutyl-ketone (MIBK) for one minute. The resin mask is then transferred to the SiN layer thanks to dry etching with Capacitively Coupled Plasma Reactive Ions Etching (CCP-RIE). The PhC pattern is transferred to the III-V stack by Inductive Coupled Plasma (ICP). The plasma is composed of oxygen and hydrogen bromide ($HBr/He/O_2$:8/90/0.9 sccm). This step is crucial because the smoothness of the etching will determine the quality of the PhC.

The remaining hard mask is removed with CCP-RIE. The sample is then very briefly put into a 1% diluted fluorhydric acid to remove any redepositon of the SiN mask during the ICP step.

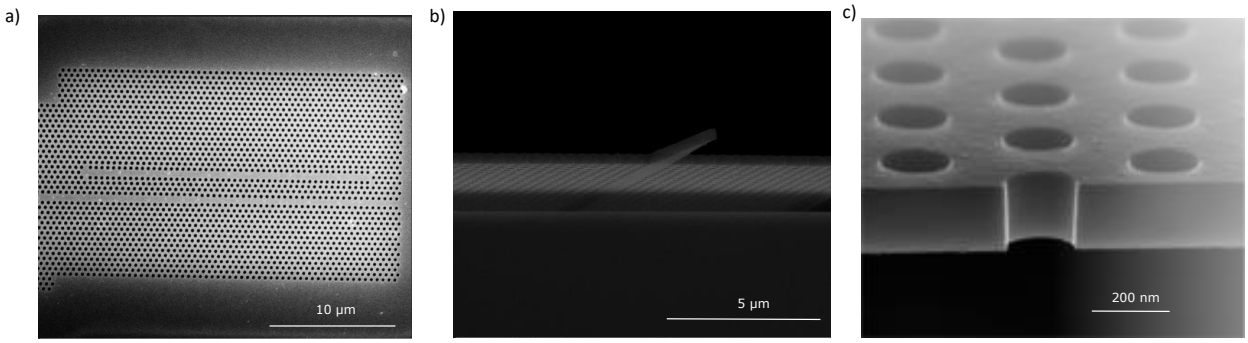

Figure 3.4: SEM picture of suspended Bichromatic membranes showing a) the cavity and its coupling waveguide, b) the coupling taper, c) a transverse cut of the membrane

Another critical step is the underetching, realized by means of a diluted citric acid solution. The time of etching needs to be sufficient enough to free the membrane completely, but not too much otherwise it collapses. It takes around one hour to underetch the bichromatic cavities in our case. Finally, the drying of the sample is realized with the critical point drying (CPD) technique that smoothly transforms the liquid into gaseous state. On the latest generation of sample, 5 nm of ALD deposition was put to protect the sample from any environmental degradation. The impact of this encapsulation was never critical, as we did not see any change in the Q factor of the cavities with or without it. Still, it did not seem to prevent photo-oxidation, which made us question the porosity of the ALD material.
Fig3.4 shows pictures taken with a scanning electron microscope (SEM). A bichromatic cavity with its access waveguide can be seen in Fig.3.4a). The coupling tip, that adapts the mode of the fiber to the mode of the PhC waveguide is shown in Fig.3.4b). Fig.3.4c) shows a zoom of the suspended membrane to verify that the roughness of the etching is good.

3.2.4 Linear characterization

Optical Measurements are performed on a temperature stabilized position stage. The laser light is injected thanks to a lensed fiber in the coupling tip of the cavity. The light reflected back from the sample is out-coupled through the same fiber but is separated away from the incoming laser thanks to an optical

circulator placed right after the fiber. The power level is adjusted thanks to a variable attenuator. The sample is placed on a copper plate that is stabilized by a Peltier/thermistor pair ensuring better than 0.1K temperature control. The position stage and the lensed fibers are placed inside a box filled with nitrogen to limit oxidation or surface degradation.
The cavities are linearly characterized with an Optical Coherent Tomography (OCT) set-up with a swept source. The principle of measurement is detailed in Annex A. The main advantage of this technique is that it allows to access to the full complex spectrum of the cavity in a single scan of the laser (around 30 seconds). The optical source is a continuously swept narrow-linewidth laser (Santec TSL510). The sample is placed in one arm of a Michelson interferometer, the second being a 7 meters single mode fiber (SMF). The reflected signal from the cavity is then mixed with the second arm and acquired with a balanced photo-detector (Thorlabs PDB450c). The instantaneous wavelength of the laser source is measured by an external reference interferometer which also triggers the acquisition of photocurrent by the ADC card.
An example of the spectrum of the cavity is shown in Fig3.5a). Here, the three first resonances are analyzed. They correspond to a Q factor of respectively 160 000, 94 000 and 130 000. Up to 7 modes were observed in the cavities. Fig3.5b) shows 3 pictures of the cavity when 3 different modes are excited. On the three picture, the left spot shows the positions of the lensed fibers, at the input of the sample. When changing the frequency of the laser, the different modes are successively exited. The top picture shows the fundamental mode. The light is concentrated in one bright spot that corresponds to the center of the cavity. The middle and bottom pictures shows the mode 3 and 7. We clearly see that the spot becomes distributed to the extremities of the cavities, as predicted by the HG distribution.

We are interested in the measurement of the dispersion of the cavity with narrow resonances. Hence, the question of the absolute error in the measured frequency is fundamental. Before characterizing the sample, a reference Hydrogen Cyanide gas cell is measured in order to correct the dispersion inside the fibers. This cell features absorption lines known with 0.2 pm precision (20 MHz). After calibration, the standard deviation from the NIST (National Institute of Standards and Technology) reference measurements is about 20 MHz. The complex reflectivity spectrum is extracted after Fourier analysis. Both the amplitude

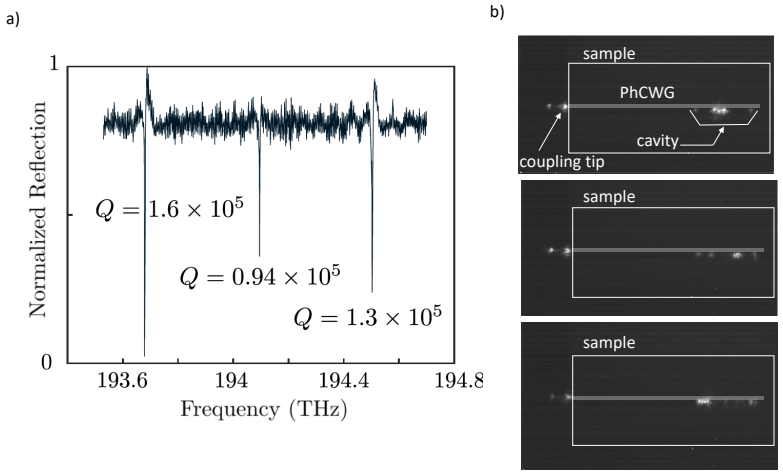

Figure 3.5: a) Spectrum of a bichromatic cavity with Q factor around 10^5 b) Picture using an infrared camera to visualize the scattering of the mode when they are excited. The non-homogeneous structure of HG modes is clearly visible
.

and phase of the spectrum are fitted with a zero/pole model which leads to the loaded Q, the intrinsic Q_0 and the coupling Q_c. The OCT measurement is performed with sufficiently low power ($< 1\mu$W) to avoid any thermal effect inside the cavity. With this technique we could measure the standard deviation of the dispersion $\Delta\nu_{cold}$ over about 300 resonances in 96 resonators.
The statistics is shown in Fig.3.6a). Here, $\Delta\nu_{cold}$ represents the evolution of the FSR between three consecutive resonances, which is the useful value for FWM. We see that it is included mainly between a $+/-100$ GHz around a flat dispersion, for a nominal FSR of 450 GHz. Most of the counts are on the negative dispersion side, which was predicted by the slight anharmonicity of the parabolic potential. However, the distribution of $\Delta\nu_{cold}$ does not follow a straightforward law. The cause for this statistics is the disorder that comes for fabrication imperfection. The role of structural disorder, already discussed in Chapter I, is evidenced here. The absolute average $|\Delta\nu_{cold}|$ is 50 GHz, while the linewidth of the resonances ranges from 1 GHz to 300 MHz.
To go further, the correlation matrix on the FSR for the first five modes of the 96 cavities is calculated. The FSR between the modes $(\nu_{i+1} - \nu_i)$ of the jth cavity is noted $F_{i,j}$. Each cavity has a nominal FSR noted $\overline{F}_j$ set by design. The

correlation matrix is written:

$$C_{j,k} = \frac{\sum_{i=1}^{4}(F_{i,j} - \overline{F}_j)(F_{i,k} - \overline{F}_k)}{\sqrt{\sum_{i=1}^{4}(F_{i,j} - \overline{F}_j)^2}\sqrt{\sum_{i=1}^{4}(F_{i,k} - \overline{F}_k)^2}}$$

Figure 3.6b) shows that a deviation from the mean FSR for two consecutive modes does not impact the fluctuations of the others FSRs for a given cavity. Therefore, it is possible to conclude that the fluctuations on the dispersion of the cavity are set by the fluctuations of each eigenfrequency. Importantly, fluctuations of the eigenfrequencies of a single cavity are uncorrelated. This result could be well explained by the non homogeneous distribution of the HG modes. A local defect would therefore affect each mode differently. This is fundamentally different to ring resonators for example, where a defect would impact almost all the modes simultaneously. As a result, the absolute frequency deviation is the same for each mode, and the FSR are on the overall kept constant.
On a side note, we suspect that thinner membranes are less sensitive to disorder fabrication, because the average effective index is lower. As a result, a perturbation in the modulation has a lower relative impact. This was observed in the samples fabricated with a 320 nm thick of InGaP that resulted in a lower Q factor on average compared to the 190 nm thick membrane. The quality of the epitaxy was also suspected to explain this difference, as some defect could be observed with the microscope.
From the nature of the HG modes and the sensitivity of PhC to fabrication variation, we showed in this section that current state of the art PhC cavities require a post fabrication tuning mechanism to reach consistently exact constant FSR, even if the design theoretically fulfills this condition.

3.3 1D PhC on SOI: the nanobeam cavity

3.3.1 Principle of the SOI structure

Air-bridged structures are interesting to realize a strong index contrast with bulk InGaP. This matter of fact explains why the highest Q factors reported up-to-date are suspended 2D silicon membrane. However, this approach has two main drawbacks. First, a suspended membrane is harder to protect it from environment pollution. Secondly, it is difficult to integrate on the same chip alongside components with different material and fabrication process flow, such

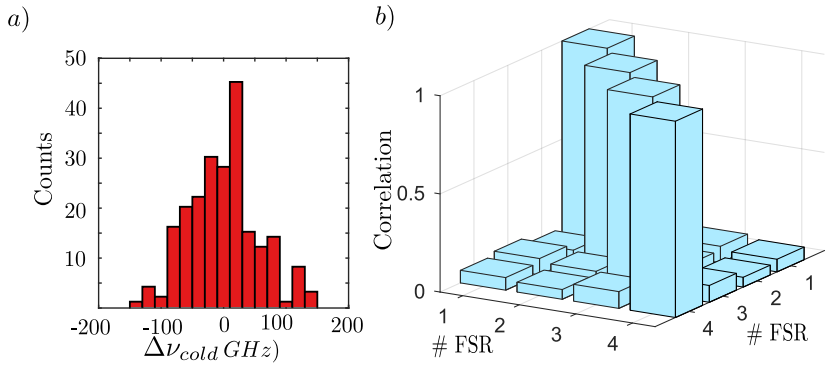

Figure 3.6: a) Histogram of the eigenfrequencies misalignment $\Delta\nu_{cold}$ b)Correlation matrix of the fluctuation of the first four FSRs (five modes) for 96 cavities.

as laser source or photodetectors. A possible workaround is the integration of specific photonic function on a silicon on insulator (SOI) platform. The SOI platform benefits from massive manufacturing capabilities developed for electronic application over the past few decades and could accelerate considerably the industrialisation of complex photonics components. Because silicon suffers from limitations such as indirect bandgap and TPA, some complex photonic function need to be realized by components made of different materials. The basic idea is to have a layer of silicon waveguides that serves as a circuitry between these photonic components: this is the basic principle of hybrid integration.

Fig. 3.7 shows a schematic of our hybrid InGaP PhC cavity on SOI for nonlinear optics applications. The SOI level consists in a 220 nm thin Si waveguide patterned on top of a SiO_2 cladding layer. The thickness of the SiO_2 layer, also called the buried oxide layer (BOX) is 2 μm. Both materials are transparent at telecom wavelength, and the confinement of the light is ensured by TIR due to the large index contrast between silicon and its oxide. The Si waveguide width ranges from 250 to 550 nm, which is low enough to ensure single mode TE propagation.

The waveguide is terminated on both side by a shallow grating coupler. The design and fabrication of these couplers is not optimized, and the transmission coefficient is rarely more than -6 dB by grating. An optimization in this direction would decrease the power level used in experiments, but the general proof of principle would remain the same. The key point here is that the final goal is to have the light source and the detector integrated alongside the nonlinear cavity. Hence, an optimization of the grating coupler is secondary.

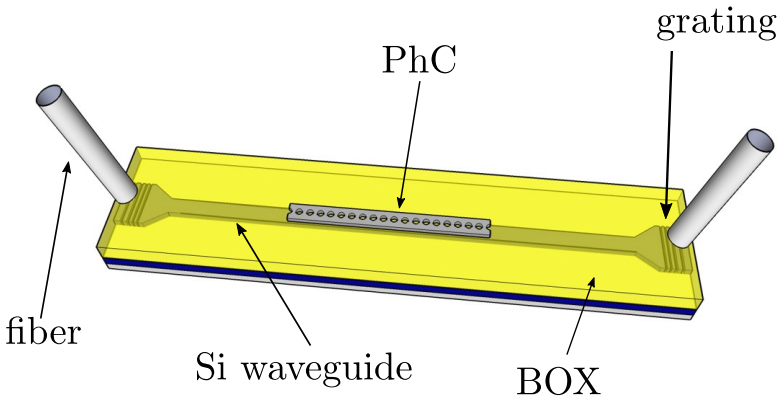

Figure 3.7: Schematic of the hybrid InGaP nanobeam of SOI structure.

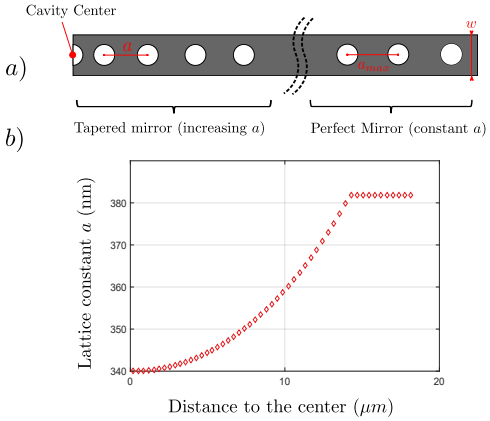

Figure 3.8: a) Schematic of the nanobeam cavity with a tapered mirror and a perfect mirror b) Evolution of the distance between the holes.

Finally, the cavity is a 1D PhC also called nanobeam. It is bonded on top of the SOI using benzocyclobutene (BCB), an adhesive polymer. The fabrication steps will be detailed in the next sections.

3.3.2 Design of the nanobeam cavity

The nanobeam cavity consists in a ridge waveguide drilled with circular holes where the hole to hole distance, a, is varied in order to build high reflectivity mirrors, (see Figure3.8). In this case, the electromagnetic field decay in the mirrors is not simply exponential as in a perfectly periodic structure but depends directly on the evolution of the lattice constant a in the longitudinal direction. Thus, the EM field in the cavity writes $E \propto e^{-A(x)x}$, , where $A(x)$ is the spatially dependent field decay at the position x. The complete methodology is developed in Ref.[122] and we will only recap the major steps. First, we

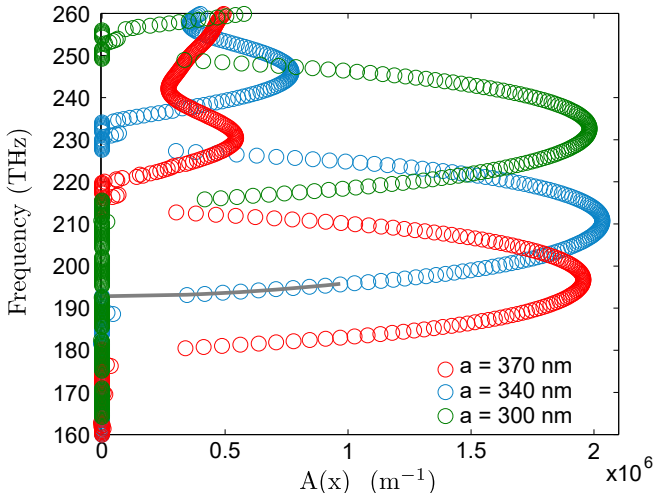

Figure 3.9: Calculated imaginary part of the evanescent field for an infinite 1D PhC (width and height : 650 × 290 nm) with a period of a= 300, 340, 370 nm with a fixed radius of 110 nm. The grey line is a parabolic fit near the band edge f_{cut} = 192.692 THz (1555 nm) in the case where a = 340 nm.

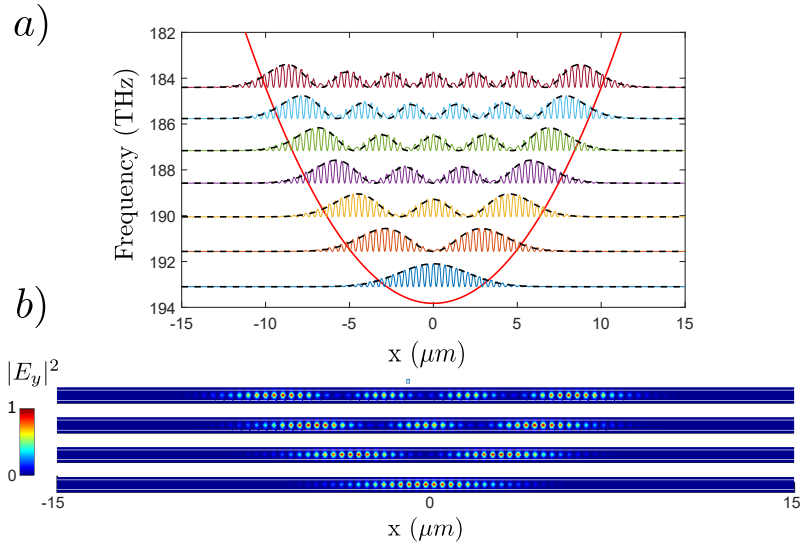

Figure 3.10: a) Calculated first seven eigenmodes represented along the x-axis, Hermite-Gauss envelopes (dashed) and the corresponding parabolic potential. b) Map of the electric field amplitude $|E_y|^2$ of the first four modes in the z = 0 plane

calculate the dependence of A with a in a semi-infinite PhC wire with a constant a. In this PhC wire, $A(x)$ is constant along the x-axis for a given frequency and a given a. The value of A for each frequency is calculated by extracting the attenuation of a broadband excitation is the axis of the wire. Fig.3.9 shows the evolution of this field decay A for different a for a 650 nm wide, 290 nm thick PhC wire made in InGaP (n=3.13) encapsulated in SiO_2 where the holes radius r = 110 nm. We see that increasing the lattice constant a changes the cut-off frequency of the dielectric band-edge, that is to say the frequency that opens the bandgap but still has $A = 0$. In the case of the blue curve ($a = 340$), this cut-off frequency is equal to 192.692 THz (1550 nm). An increase in the period a leads to an increase in the field decay A up to its maximum value located a half the width of the bandgap. Once the relation between a and A is established, we can introduce a variation of the period $a(x)$ so that $A(x) = Bx$ in order to shape the first order resonant mode E-field envelope into a Gaussian. This envelope is characterized by its full width at half maximum (FWHM) which can be adjusted at will by changing $a(x)$. The calculated dependence of a with x is plotted on Fig.3.8) for a cut-off frequency at 192.692 THz. We can see that a increases from 340 nm in the center of the cavity (A=0) to 382 nm at its extremities (maximum of A which corresponds to the middle of the photonic bandgap at 1550 nm). 10 holes are added on the sides of the cavity with $a = 382$ nm to avoid leakage of the EM field in the longitudinal direction.

Such a design allows us to obtain in simulation (3D FDTD) a Gaussian shaped mode at 193.103 THz (1552.5 nm) with a Q factor beyond 10^7. This high Q value is expected: this mode exhibits a reduced amplitude of the E-field distribution at spatial frequencies inside the light cone which thereby diminishes radiative losses as previously stated, while keeping the modal volume close to the diffraction limit. Higher order modes are allowed. Their spatial distribution in energy as well as their resonant frequency are given in Fig.3.10a) and b) together with those of the fundamental mode. The modes are equally spaced in frequency, separated by a FSR of 1.4 THz. The Q factor of these modes are all above 10^7. The spatial envelope of the modes contains a number of lobes equals to their order and, as can be seen on Fig.3.10a), it can be accurately fitted by a Hermite-Gauss function. Built under the only condition of achieving a spatially-Gaussian fundamental mode and not a parabolic evolution of the lattice constant a, this cavity possess a modal structure very similar to the one presented in the previous

section, with the bichromatic design.
Where the bichromatic design depends on the commensurability parameter a'/a, this design of nanobeam tailors the photonic potential with the FWHM of the fundamental mode. particularly, the FSR can be adjusted to a large extent as shown in Fig.3.11a).

A striking feature of this PhC multi-mode cavity design is its flexibility. Particularly, the FSR can be adjusted to a large extent as shown in Fig.3.11a), the FSR being related to the FWHM of the fundamental Gaussian mode, which is our key design parameter. We note a parabolic dependence of the FSR with $(\text{FWHM})^{-1}$, while in a Fabry-Perot or a ring resonator, the FSR is linearly dependent with the inverse of the length of the cavity. The frequency of the fundamental mode also slightly changes from 192.5 THz (1557.4 nm) to 193.8 THz (1546.7 nm) when the FSR decreases from 2.4 THz (19 nm) to 130 GHz (1 nm) for identical geometric parameters (dimension of the ridge, hole diameter, initial and final hole period). Moreover, as FWHM increases, the full cavity length strongly increases due to our design rules previously described. The calculated volume of the fundamental mode, $V_{m,0}$, (see Fig. 3.11b)) grows linearly with the FWHM, ranging from 0.76 to 4.45 $\left(\frac{\lambda}{n}\right)^3$ when the FWHM increases from 2 μm to 12 μm. Fig.3.11c) shows the calculated volume of the higher order modes for FWHM = 4 μm and FWHM = 12 μm. As expected, it increases with the mode order, the largest change being observed going from the fundamental to 2nd order mode. $V_{m,p}$ doubles its value only up to the seventh order mode.

3.3.3 Fabrication process

The fabrication steps of the hybrid nanobeam on SOI are depicted in Fig.3.12. Following the hybrid integration principle, our nanobeam cavities made in InGaP slabs are bonded onto a SOI waveguide circuitry[123]. The starting point are the SOI wafer and the same InGaP/GaAs stack than for the bichromatic cavity with 320 nm thickness.
A thin layer of 20 nm of SiO_2 is deposited by ALD on the InGaP. Then 330 nm of SiO_2 are sputtered. This step is necessary because sputtered SiO_2 is hydrophilic, contrary to PECVD SiO_2 for example, and BCB bonding works only on with hydrophilic surfaces. During the whole process, we have to make sure that BCB has not been in contact with water or any wet surface. The ALD layer is here to protect the InGaP that could be damaged during the sputtering.

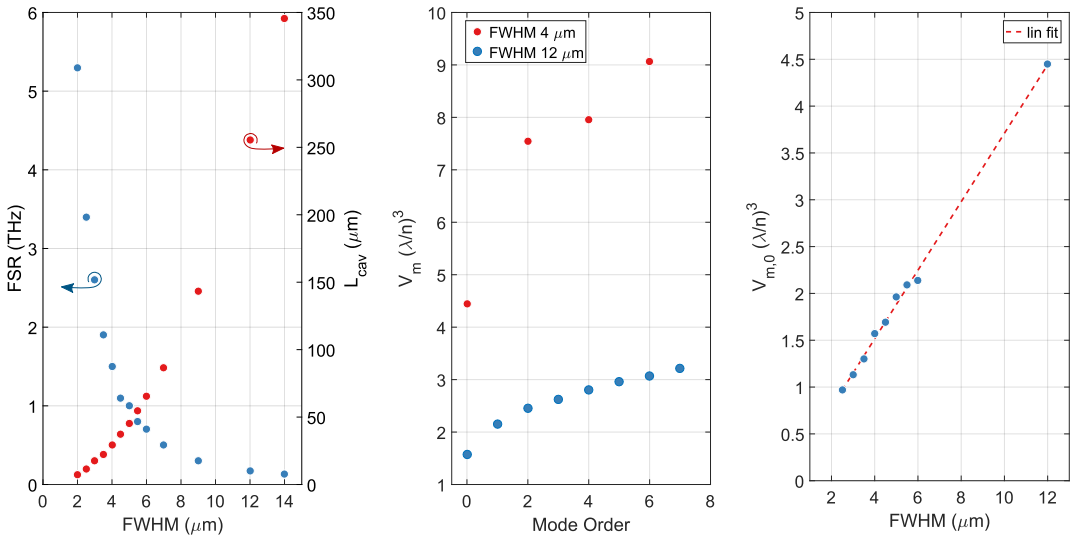

Figure 3.11: a) Evolution of the FSR with the FWHM of the fundamental mode and the corresponding length of the cavity. b) Mode volume of the first modes of a 4 mm and a 12 mm FWHM cavity. Volume units are normalized with the diffraction volume. c)Evolution of the volume of the fundamental mode with respect to the FWHM. Red dotted line is a linear fit

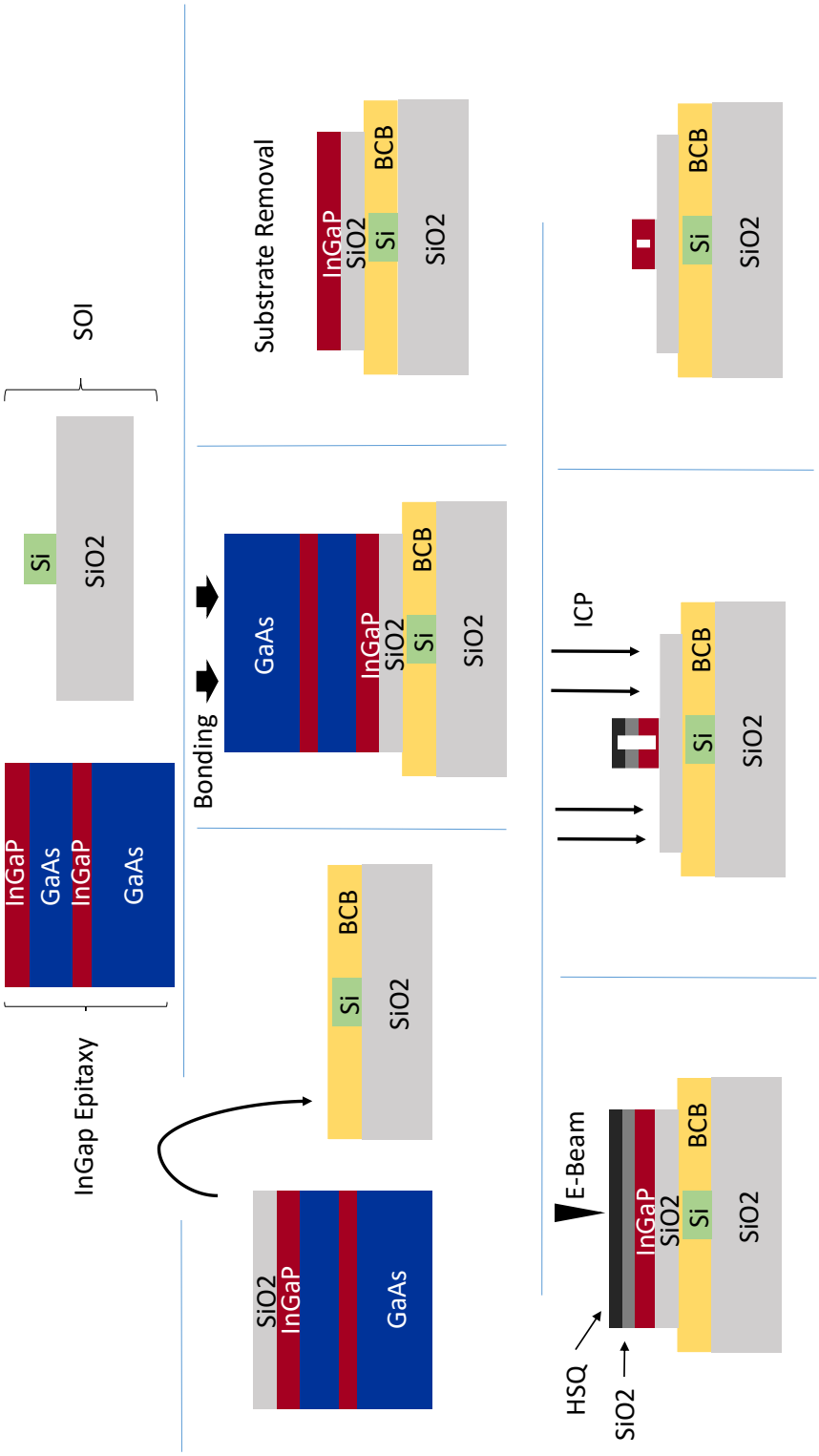

Figure 3.12: Fabrication steps for the InGaP nanobeam on SOI via wafer bonding

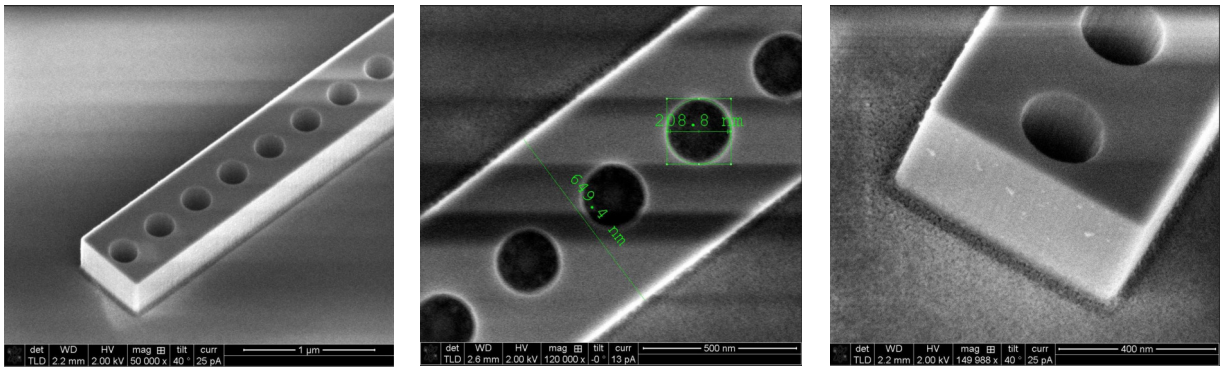

Figure 3.13: SEM pictures of the nanobeam after fabrication.

The bonding layer is an adhesive polymer solution of divinylsiloxane-benzocyclobutene (BCB), with its solvent, mesitylene with the ratio (2 ml/ 1.5 ml). BCB is spin coated with a spinning speed of 5000 rpm, initial acceleration of 2000 rpm/s for 30 second. These parameters are set to have a final BCB thickness of 300 nm. The SOI with BCB is then soflty baked at 80 °C for 15 minutes to evaporate the solvent.

The next step puts the InGaP stack on the SOI with BCB in the chamber of the bonder (Süss MicroTech). This machine realizes the bonding by applying a press at 320 °C in vacuum to polymerize the BCB.

The next step is substrate removal. It is realized by wet etching. The GaAs substrate is removed using a H_2O_2:NH_3 solution diluted at 19:1. When the GaAs is removed, usually after 2 hours, we can observed a pink-colored surface indicating the presence of InGaP. This stop layer is removed in pure HCl for 20 seconds, and the final GaAs layer is plunged back into the H_2O_2:NH_3 solution for 40 seconds. It is during this step that the success of the bonding is observed, because the substrate removal gradually reveals any mechanical strains on the InGaP layer that can very often suffer form big cracks or in the worst case, lift off.

The next step is the patterning of the nanobeam cavity. This is done by negative lithography with a Leica EBPG5000+ beamwritter. Hydrogen Silses Quioxane

(HSQ) is spin coated on top of the GaInP membrane (with filter XR1541-006) with a spinning speed of 600 rpm and an initial acceleration of 3000 rpm/s for 60 seconds. A 5 nm ALD SiO_2 was deposited prior to the resin to ensure adhesion. Contrary to positive resist used for 2D PhC, in the case of HSQ resist, exposed surfaces are solidified while the non exposed surfaces are removed with the developer AZ400K:H2O (1:4) for 1 min 30. Single pass lithography with hole contouring is used with a writing resolution of 0.5 nm.
Finally, after revelation of the HSQ mask, holes are drilled with Inductive Coupling Plasma (ICP) etching using the same $HBr/He/O_2$ gas mix than the 2D PhC. The exposed HSQ plays is similar to silica. As a result, it can be either kept on top of the InGaP, either removed with diluted AF at 1% As can be seen on the SEM picture of Fig.3.13 , very smooth sidewalls are obtained from the optimized etching process.
A final encapsulation step an be added, just like with the bichromatic cavities, consisting in 20 nm of ALD Al_2O_3.

3.3.4 Linear Characterisation

The linear transmission of the fabricated bonded nanobeams is again characterized using the OCT setup employing a spectrally narrow swept laser source which is coupled to SOI waveguides through the grating couplers. The difference here is that the OCT is used in transmission and not in reflection. The interferometer is then a Mach–Zehnder interferometer. The transmission spectra displays a comb of high Q resonances, as can be seen on Fig.3.14a). 54 resonances can be counted on Fig.3.14a), this number being limited, here, by the transmission bandwidth of the gratings couplers. This spectrum corresponds to the transmission of a cavity with a FWHM = 12 μm. The high reflectivity bandwidth of the mirrors of the cavity, which is determined by the width of the photonic bandgap of the PhC ($\sim$40 THz), allows the existence of this high number of resonances which is far greater than 2D bichromatic cavities (typically 4 or 5 modes) thanks to a larger PBG. The mode order of each resonance is plotted on Fig.3.14b) as a function of its frequency. The linearity of the obtained curve is, at first glance, a proof that the FSR is constant as the mode order increases. Only one resonance was not detected in this measurement. Looking closely at the FSR as a function of the frequency (Fig.3.14c)), we can see that it oscillates in a 100 GHz range and stabilizes toward a constant value

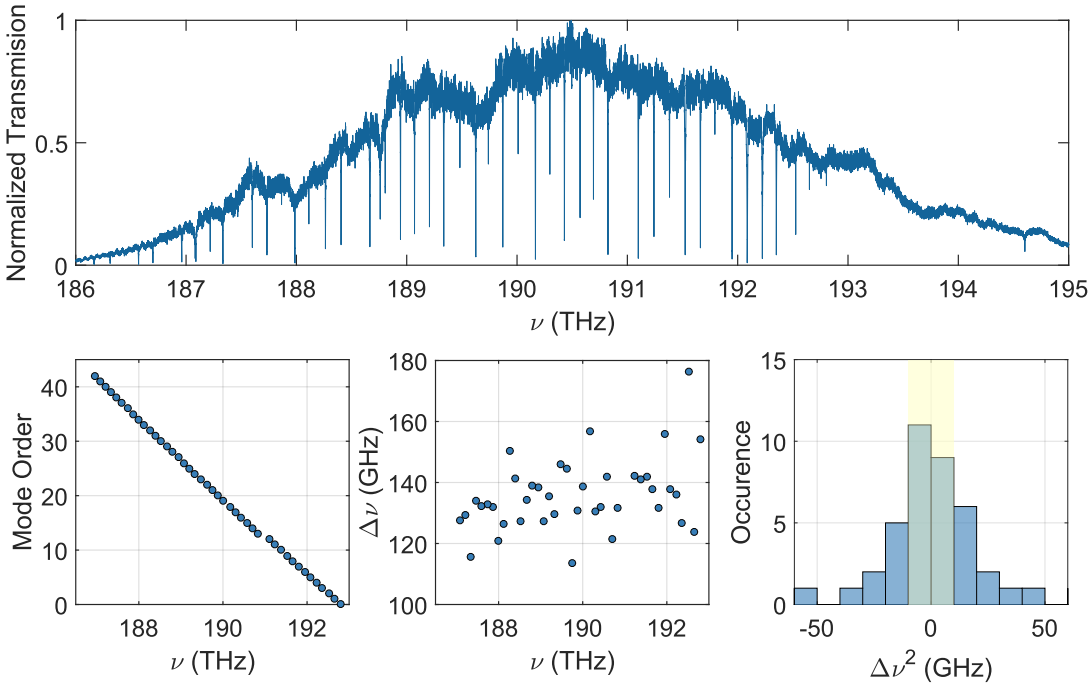

Figure 3.14: a) Normalized Raw Transmission Spectrum of the full device (including grating couplers); b) extracted eigenfrequencies; c) FSR vs frequency and d) histogram of the frequency mismatch D2n of three consecutive resonances.

around 130 GHz. We infer that this oscillation is due to a Moiré effect that happens during the discretization of the e-beam writing grid. A histogram of the second order dispersion for three consecutive resonances is plotted on Fig.3.14d)). The region highlighted in yellow shows the triplets with a frequency mismatch below 10 GHz. The distribution appears to be normal and centered around 0. Again, the intrinsic and coupling losses of all resonant modes are deduced from the coupled mode theory model related to the measurement OCT technique (Annex 1). Fig.3.15a), b) and c) shows the dependence of the quality factors Q_0 (linked to intrinsic loss), Q_c (coupling loss) and Q_L (total loss) factors on the width of the feeding SOI waveguide. The statistics of Q_0 is independent of the coupling strength, as expected, and reveals that the most frequent value is around 200 000 with a maximum at 445 000, which is a record in InGaP bonded structure. It is limited by the roughness of the etched sidewalls and the absorption of the InGaP and the silica intermediate layers. We suspect the latter to be the main limitation.

As previously demonstrated the coupling between the silicon waveguide and the nanobeam can be tuned by changing the thickness of the adhesive silica layer or

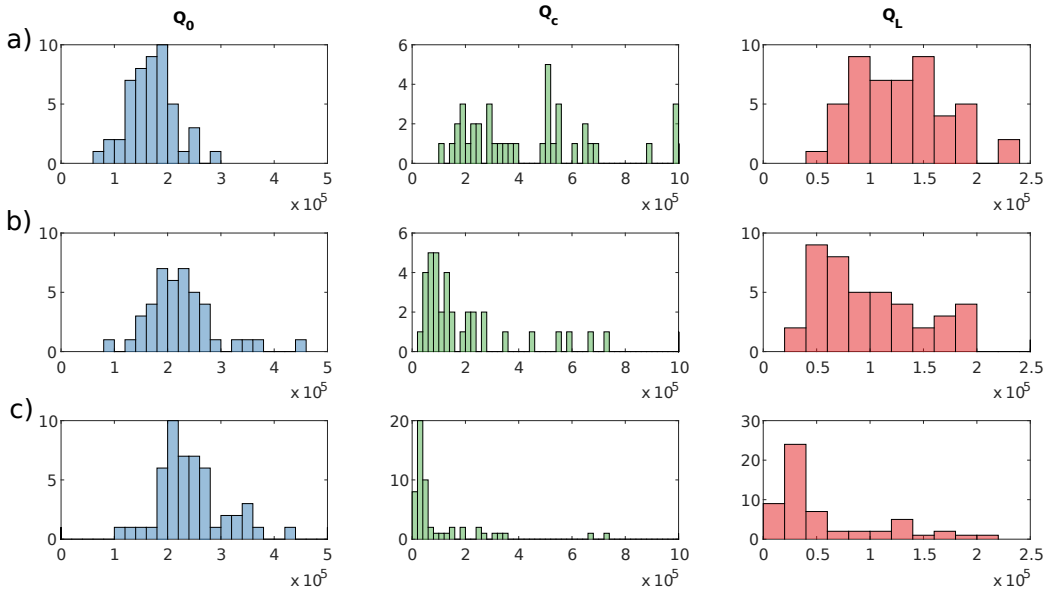

Figure 3.15: Statistical analysis of the values of Q factors of a nanobeam with 12 microns FWHM fed with a waveguide width of a) 400 nm (under-coupled regime); b) 550 nm (critically-coupled regime) and c) 500 nm (over-coupled regime)

the width of the feeding waveguide[124]. Q_c is strongly dependent of the width of the SOI waveguide as can be seen on Fig.3.15. Three representative cases are shown: the under-coupled ($Q_0 < Q_c$) regime with 400 nm wide waveguides (a), the over-coupled one ($Q_0 > Q_c$) with 500 nm waveguides (c) and the critically coupled ($Q_0 = Q_c$) one with 550 nm waveguides (b). The averaged Q_c are 440 000, 100 000 and 197 000 , for 400, 500, 550 nm wide waveguides, respectively and the average Q_0 are 171 000 (a), 224 000 (b) and 243 000 (c) . The average loaded Q, Q_L, can then be tuned from 58 000 (c) to 128 000 (a) just by changing Q_c through a change of waveguide width, and reaches $Q_L = 99\ 000$ at critical coupling (b) . In the transmission window of the gratings, we did not observe a dispersive coupling (contrary to the PhC waveguide coupling the bichromatic cavity), but some resonances can be unexpectedly under or over-coupled, which is attributed to localized default arising from fabrication.

Conclusion

In this chapter, we discussed the design and fabrication of photonic crystal cavities for nonlinear optics application. We studied and realized two different platforms namely suspended and bonded membranes. Both rely on the same idea to create a parabolic potential for the photons leading to equispaced modes. An OCT setup has been used to probe the spectra of the fabricated cavity. It confirmed the existence of several high Q modes. The suspended membranes has exhibit higher Q because of the absorption of the silica layer used in bonded cavities. On the other hand, we showed the versatility of the nanobeam by adjusting the coupling between the feeding waveguide and the cavity in simple way. The nanobeam also possess a much larger number of modes, thanks to a higher PBG, which can be interesting for some applications. With this study, we gave the proof that PhC cavities based on a parabolic modulation of the refractive index are suitable candidate for efficient FWM.
However, we also evidenced the extreme sensitivity of PhC to any sort of irregularities induced during the fabrication steps, which is combined to the fact that very high Qs narrow greatly the tolerance in the misalignment of the modes. As a consequence, this fabricated cavities are not directly usable for FWM, and a tuning mechanism must be introduced.

Chapter 4

Four Wave mixing in PhC cavities

This chapter reports the different FWM experiments performed in the cavities described in Chapter 3. These cavities are by design adapted for FWM with a near constant FSR and very high Q factor. However, the optical characterization after fabrication showed a somewhat significant deviation from a flat linear dispersion. Moreover, the higher the Q factor, the more stringent the condition on the FSR. Indeed, this condition is directly set by the linewidth of the resonance. For Q = 10^5 which corresponds to $\Delta\nu \approx 1.9$ GHz, resonant pump and signal waves allow a tolerance on the idler resonance detuning below 1 GHz in order to achieve a triply resonant configuration. Hence, there is a need for a post-processsing tuning mechanism to adjust the dispersion of the cavity.

The first part of this chapter describes a method to locally control the temperature of the cavity so that it is possible tune the relative position of the resonances.

Secondly, we show how this technique enables the observation of efficient stimulated and spontaneous FWM in bichromatic cavities up to the parametric oscillation regime. A comparison with the theoretical model developed in Chapter 2 corroborates its validity to describe our system.

Thirdly, we continue our investigation with the demonstration of efficient stimulated FWM in our hybrid nanobeam structure.

The final discussion puts these results in the context of cavity integrated nonlinear optics.

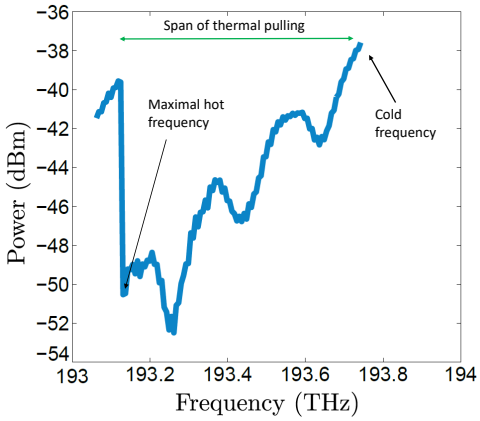

Figure 4.1: Thermal bistability of the pump mode. The frequency of the pump is thermally locked to the pump laser and red-detuned up to the point where the bistable jump happens. The oscillations are due to a Fabry-Perot with the collimator.

4.1 Thermal tuning for PhC cavity alignment

4.1.1 Thermal locking of a cavity resonance

The large density of energy inside the cavity causes a thermalization of the material via residual absorption. This induces a change in the refractive index known as the thermo-optic effect. As a result, the cavity resonance frequencies become dependent on the built-up optical field. The more optical power is injected, the more the cavity heats and the stronger is the thermo-refractive index. This is visible in the transmission spectrum of the cavity where a triangular shape appears during the scan of the cold resonance. As the laser frequency approaches the resonant frequency, the cavity heat up, which red shifts the resonance. It can be viewed as the laser "pushing" the resonance toward lower frequencies. The resonant frequency is said to be locked to the laser. The laser eventually catches up with resonance when the thermal absorption is maximal. Beyond this point, cavity can not be heated more. This means that if the laser keeps scanning, it will lose the resonance locking and will stop to couple light inside the cavity. Hence, the cavity goes back to thermal equilibrium and the resonance frequency goes back to its original value. This thermal bistability is illustrated in Fig.4.1. Here, a 1 GHz-wide resonance frequency in a bichromatic resonator is locked and shifted on more than 650 GHz. We clearly see the bistable jump happening at the pump frequency 193.15 THz. Thermal bistability has been extensively stud-

ied in micro-resonators[125, 126] where it cannot be ignored due to their small size.

4.1.2 Thermal tuning for inhomogenous modes

Tuning the resonant frequency in PhC cavity has been performed with various physical mechanisms such as gas condensation[127], chemical etching[128],carrier injection[129] or electrical heaters[130]. These techniques all aimed at adjusting the frequency of a single mode cavity. They all possess different advantages in terms of implementation, scalability or timescale. For example, the thermal effect is slower than carrier recombination which can be privileged for fast application such as all optical switching. But metallic heaters are driven electrically, which require less complexity than all optical control.

The main issue in our case is that we want to control each resonance of a single cavity individually. Individual control of the resonances of an array of coupled PhC cavity have been realized by projecting a laser beam[131] with specific spatial pattern. The illuminated section of the array is heated, which increases the refractive index of material and therefore decreases the resonant frequency of the supermode of the CROW. This tuning mechanism is limited by the spatial resolution of the optical setup of the projected beam. The important idea here is that it is possible to induce a local temperature of a PhC cavity at a shorter scale than the spatial distribution of the mode. This results into a relative inhomogenous frequency tuning of the resonances.

Conveniently, the cavity that we designed in analogy with the harmonic oscillator possess an inhomogenous mode distribution, with the energy being mainly inside two lateral lobes. When a pump is resonantly injected inside a mode, a temperature gradient that follows the spatial distribution of the mode is created. This temperature gradient overlaps differently with the other modes. As a result, the average temperature of each mode will be increased differently as well, leading to a inhomogenous spectral shift of the resonances of a single cavity. The goal is to inject the right amount of optical power so that the cavity becomes triply resonant. By sweeping the frequency of the pump, one can adjust this power by choosing the right detuning of the pump from its hot resonance.

Before showing experimental evidence of this mechanism, two remarks can be made. First, a parallel can be drawn with the continuous sweep of the laser source for soliton comb generation. The difference here is that the speed is not

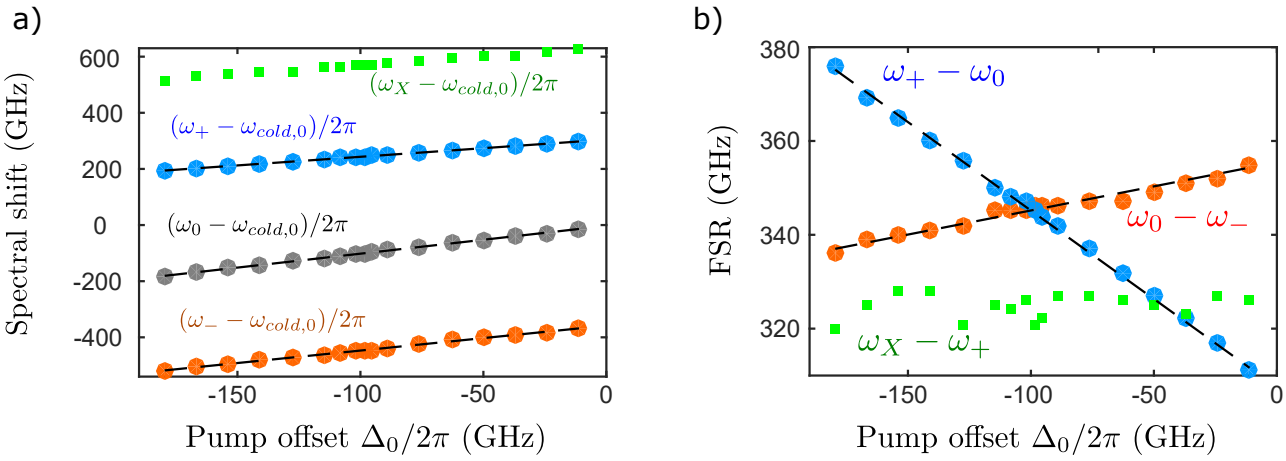

Figure 4.2: a) Evolution of the eigenfrequencies of a bichromatic cavity when a mode is locked and redshifted. The pump mode is black. The slopes of the curves are all different b) Evolution of the corresponding FSR, showing a crossing between the red and blue curves. The FSR in green, corresponding to higher order modes, is almost constant

critical as it can be anything below the thermal stabilization time of the cavity (microseconds typically), whereas it must be superior for solitons, in order to reach the thermally unstable side of the tuning range. Secondly, the swept source could be replaced by a fixed wavelength laser and thermal control of the sample, as reported in Ref. [132].

4.1.3 Thermal pulling measurement

As we just explained, the principle of this experiment is to measure the linear dispersion of the cavity when one resonance is thermally locked and pulled by a pump laser. To do so, the sample is placed in the same experimental condition as for the linear characterization (a box filled with N_2 with a thermally Peltier-regulated copper plate holder). We add to this setup a continuously swept laser. This laser source is combined with the optical signal of our OCT setup by means of a 90/10 coupler. The measurement consists in a series of OCT scan at different pump frequencies. It starts with a OCT scan with pump out of resonance. The pump is gradually red-detuned, with an OCT scan for each detuning. The procedure goes on until the thermal bistable jump occurs, when the detuning of the pump laser is larger than the thermo-optic induced frequency shift. This event corresponds to an effective detuning from the hot resonance exactly equal to zero.

The evolution of the resonance frequencies of a triplet can be see in Fig.4.2a). Following the notation of Chapter II, the pump is injected in the mode of cold frequency $\omega_{0,cold}$. The high and low energy mode are denoted $\omega_{+,cold}$ and $\omega_{-,cold}$. For each value of pump detuning offset Δ_0, the hot frequencies ω_0, ω_+ and ω_- are red-shifted differently. This can be seen on the slope of the different lines. These slopes corresponds to the thermo-optic coefficients α_0, α_+ and α_-. The evolution of the corresponding FSR $\omega_+ - \omega_0$ and $\omega_0 - \omega_-$ is shown in Fig.4.2b). The spectral misalignment of the cold cavity is 38 GHz, become null for a pump detuning of $\Delta_0 = -101GHz$ to reach the value of -37 GHz for a pump detuning of $\Delta_0 = -180GHz$.

It is then possible to extract the dependence of the dispersion , which is the misalignment of the hot cavity modes $2\Delta\omega_h = 2\omega_0 - \omega_- - \omega_+$ with the pump detuning. On the measurement shown in Fig4.2, this relation is $2\Delta\omega_h = 2\Delta\omega_{cold} + 0.48\Delta_0$ where $\Delta\omega_{cold}$ is the misalignment of the "cold" cavity and $\Delta_0 = \omega_p - \omega_{0,cold}$ is the pump offset. With this measurement, we are able to show that a cavity with the initial negative detuning can be tuned into a triple resonant configuration. If the pump offset is increased, it is possible to even inverse the sign of the dispersion for this specific triplet.

On the same figure, the green dots corresponds to the evolution of the next higher order mode, and its FSR $\omega_X - \omega_+$. We see that this value remains almost constant, showing that the thermal coefficients of the mode + and X are equal. As a result, the cavity is triply resonant with the triplet (0, +, X), corresponding to the crossing of the blue and green lines in Fig.4.2b) for a different pump detuning (-40 GHz) . This shows that the tuning mechanism allows to align only three resonances at a time, in contrast with ring resonators where multiple triplet have the same FSR.

4.2 Modeling the nonlinear cavity

4.2.1 Extraction of the on-chip power and the coupling losses

For linear characterization, the power level used is not critical as long as it does not trigger optical or thermal nonlinearities. On the opposite, it is crucial for nonlinear experiments to have a correct value of the power in order to estimate the efficiency of the FWM. The procedure for extracting the on-chip power is

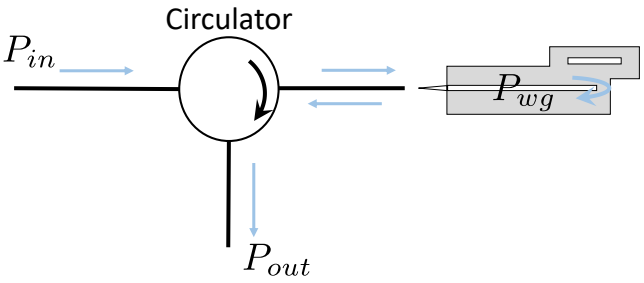

Figure 4.3: a) Schematic of the coupling configuration with a 3 port optical circulator, that allows to estimate the power inside the waveguide in a single ended configuration.

detailed here.

For the bichromatic cavities, the resonator is designed in a single ended configuration, meaning that the optical power is reflected back in the access waveguide. In our setup, the resonator is accessed through a microscope objective (Zeiss, N.A.=0.9, x 63) focusing on an inverse taper[69]. This inverse taper adapts the Gaussian beam to the Bloch mode of the PhC waveguide connecting the resonator, Fig.3.4c). The waveguide is terminated to ensure total reflection with minimized out of plane scattering. A circulator is used to separate the input of the output. An optical circulator is a three ports non reciprocal device that redirects light depending on its propagation direction. As a result, an unidirectional connection is ensured between two adjacent ports, as depicted in Fig4.3. Port 1 is the input and carries the pump and probe beams, previously combined with a coupler. The input is directed to port 2, with is connected to a fiber collimator. This fiber collimator is itself put on the focal distance of the microscope objective to ensure optimal coupling with the sample. When the light is reflected at the end of the sample, it is coupled back in the port 2 of the circulator and is redirected to the port 3, which is the output. An alternative but equivalent set-up also used here is based on tapered fiber instead of a microscope objective In order to estimate the on-chip power, that is the power at the end of the coupling waveguide, where the cavity is, two assumptions are made. First, the circulator is assumed to have identical coupling losses from port to port which makes the global system symmetric. The other assumption is that the waveguide is too short ($L = 250\mu m$) to induce significant losses (typically 1dB/mm[133]) . These approximations allow to take the same coupling coefficient κ_{in} for the input to the waveguide and for the output to the waveguide, and no other loss term than the coupling when the laser is off resonance. Hence, the different

power are linked by the relation:

$$P_{wg} = \kappa_{in} P_{in} \tag{4.1}$$

$$P_{out} = \kappa_{in} P_{wg} \tag{4.2}$$

The power inside the waveguide is then the geometric average of the power measured on port 1 and port 3:

$$P_{wg} = \sqrt{P_{in} P_{out}} \tag{4.3}$$

In order to estimate the power level, the insertion losses are measured once the setup is aligned on the cavity. The insersion losses are measured at low power off resonance through the relation:

$$2\kappa_{in} = 10log(\frac{P_{out}}{P_{in}}) \tag{4.4}$$

Typically, the value of κ_{in} is around -6.5 ± 0.5dB. The error margin corresponds to changes between samples or frequency dependence due to residual interference (Fabry-Perot effect, TE-TM modes).

4.2.2 Energy in the cavity and nonlinear absorption

The tuning mechanism is based on the thermal pulling of the pump resonance. From a physical standpoint, the spectral shift of the cavity is proportional to the fraction of the energy that is absorbed by the material and dissipated through heat. However, the dissipation rate is only a fraction of the total intrinsic losses because a fraction of the energy is also lost by diffusion. ($\Gamma = \Gamma_{abs} + \Gamma_{diff}$). The dissipated power associated with linear losses writes:

$$P_{diss} = \Gamma_{abs} |a|^2 \tag{4.5}$$

We now need to measure the coefficient Γ_{abs}. To do so, we measure the spectral shift of the resonance just before the bistable jump as a function of the power coupled in the cavity. At the bistable jump, we know that the laser is exactly resonant. From the CMT model of Chapter 2 (Eq.2.41 with $\delta = 0$), we know that the fraction of pump energy coupled in the mode is:

$$W = |a|^2 = \frac{4\kappa}{(\Gamma + \kappa)^2} P \tag{4.6}$$

This allows us to plot the maximum spectral shift as a function of the energy inside the cavity, represented in Fig.4.4a). Knowing the thermal capacitance of

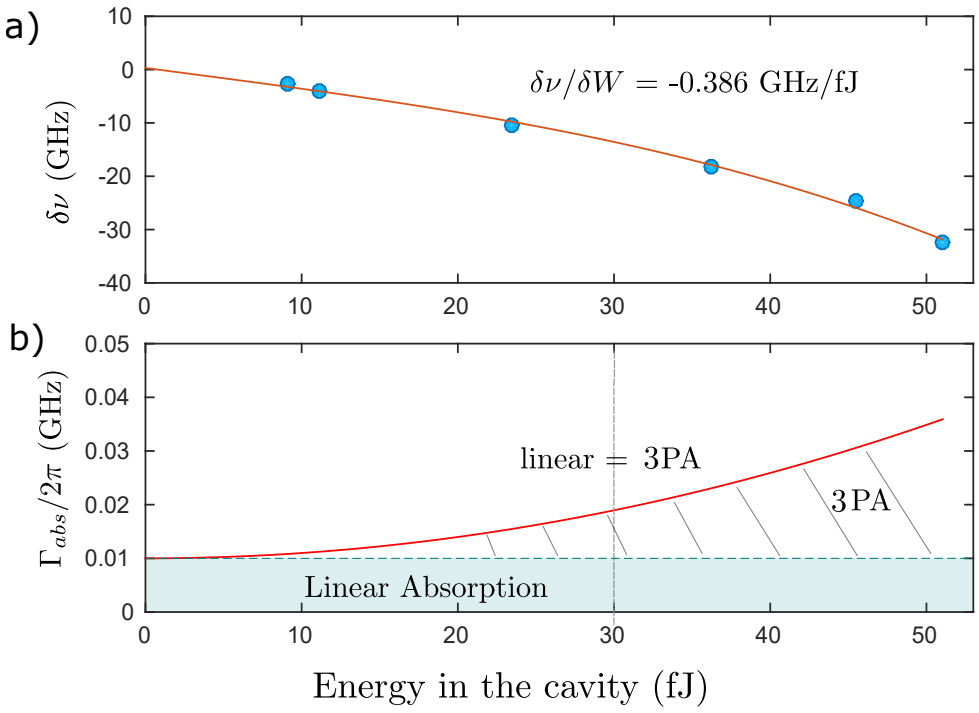

Figure 4.4: a) Measured spectral red-detuning as a function of the energy inside the cavity. b) Estimation of the corresponding absorption rate. We see a nonlinear dependence indicating nonlinear absorption that takes over when more than 30 fJ are injected in the cavity.

the resonator it is possible to infer the dissipated power, hence the absorption rate. By definition,

$$\Delta T = R_{th} P_{diss} \tag{4.7}$$

Hence, the dissipated power can be extrapolated through:

$$P_{diss} = \frac{\Delta T}{R_{th}} = \frac{1}{R_{th}} (\frac{\partial \nu}{\partial T})^{-1} \frac{\partial \nu}{\partial P} P \tag{4.8}$$

For suspended InGaP PhC membranes (same thickness of 190 nm) , $R_{th} = 21 W^{-1} K m$ (calculated in Ref.[121]) and the coefficient $\frac{\partial \nu}{\partial T} = -10.8 GHz/K$ (measured in Ref.[120]). This gives the relation:

$$\Gamma_{abs} = \frac{P_{diss}}{|a|^2} = \frac{1}{R_{th}} (\frac{\partial \nu}{\partial T})^{-1} \frac{\partial \nu}{\partial P} \frac{(\Gamma + \kappa)^2}{4\kappa} \tag{4.9}$$

The maximal spectral shift at different power level is plotted in Fig.4.4a). If the losses were linear, we would expect a straight line. We see a deviation indicating the presence of nonlinear absorption. The corresponding Γ_{abs} are shown in Figure 4.4b). It suggests that nonlinear absorption (three photon absorption 3PA) is taking over at some point. From the fit it is possible to infer the energy at which linear and nonlinear absorption are comparable, namely 30 fJ. This value agrees well with the model (Eq.2.86). Indeed, the 3PA coefficient for InGaP is 6×10^{-26}[133] and the 3PA volume is calculated to be $V_{3PA}^{-2} = 2 \times 10^{-37} m^6$. Hence the linear and nonlinear absorption are comparable when $\Gamma_{3PA} W^2 = \Gamma_{abs}$ which gives the value $W = 22 fJ$.

4.2.3 Effective temperature of the mode

As in Ref. [98], we introduce an effective mode temperature ΔT_{eff} that represents the temperature averaged over the mode profile in a cavity that is locally heated by an inhomogenous $\Delta T(r)$.

$$\Delta T_{eff} = \frac{\int \Delta T(r) \epsilon(r) |E(r)|^2 d^3 r}{\int \epsilon(r) |E(r)|^2 d^3 r}$$

which relates to the spectral shift of the resonance through the thermo-optic coefficient of the material with the relation:

$$\Delta \omega = \Delta T_{eff} \frac{d\omega}{dT} \tag{4.10}$$

ΔT_{eff} is specific of each mode, depending on the spatial overlap of the optical and temperature fields. This leads to a differential thermo-refractive effect which

is exploited to tune the mutual mode spacing. This effect can be estimated solving the heat equation considering $40 \times 20 \mu m^2$ InGaP membrane bordered by a thermal sink and N_2 atmosphere. An uniform averaged thermal conductivity κ is assumed.

$$\kappa(x, y, z)\nabla T + Q = 0 \tag{4.11}$$

The source term Q is defined by the dissipation in mode 0 (pump). We neglect the inhomogeneity due to the holes because the diffusion length is one order of magnitude larger than the photonic crystal lattice constant. The elevation of temperature in the longitudinal axis of the cavity is represented in Fig.4.5 when the first order mode is pumped, alongside the spatial repartition of the energy density of the 3 first modes. Assuming the dissipation rate Γ_{abs} is the same for all modes, the differential thermo-refractive effect, i.e. the relative thermal shift between mode i and the pump mode 0 is deduced as the ratio $\Delta T_{eff,i}/\Delta T_{eff,0}$, hence:

$$\begin{aligned} \frac{\alpha_{0,-}}{\alpha_{0,0}} &= 0.9 \\ \frac{\alpha_{0,+}}{\alpha_{0,0}} &= 0.75 \end{aligned}$$

These coefficients are defined in Chapter 2 as the cross-thermal coefficient. They corresponds to the slope of the mode shifting for modes (+,-) in Fig.4.2a). Experiments show slightly smaller values (0.9 and 0.62 respectively), which could be explained by the simplifications made in the model, in particular neglecting nonlinear absorption. Moreover, the difference between the two experimental values suggests that there is a nonlinear contribution to the absorption which depends on the operating conditions. The thermal model presented here is too simplistic to explain this phenomenon but it shows that it is possible to tune the modes.

4.2.4 Modeling FWM in the cavity

We have estimated the linear characteristics and the thermal coefficients. We can now use these parameters to simulate the stimulated FWM of a cavity . The master equation (2.36) is solved in the undepleted pump approximation e.g. Eq.(2.40), Eqs.(2.62) and (2.63) and the parameters used are listed in Table

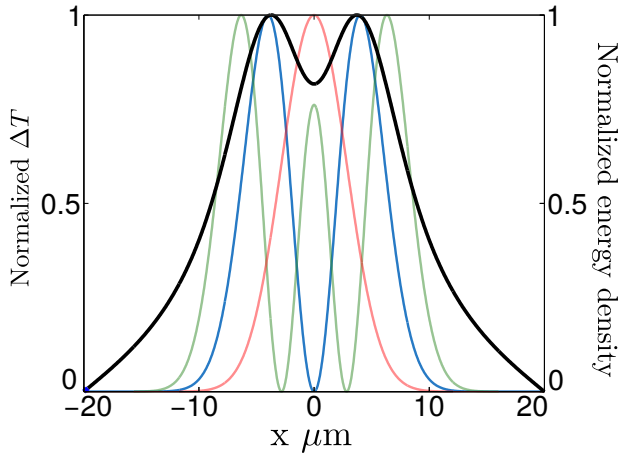

Figure 4.5: a) In black, normalized temperature profile along the longitudinal axis of the cavity when the first order mode (blue curve) is pumped. The spatial overlap with the mode 0 (red) and 2 (green) is different, leading to different effective mode temperature.

B.1 of Annex B. They correspond to the cavities that will be experimentally investigated.

The first one is labeled Cavity #27. It has an average $Q_{avg} = 64000$ and initial cavity dispersion $\Delta\omega_{cold}/2\pi = 25GHz$. The calculated map of the nonlinear efficiency as a function of the pump and probe detuning is represented in Fig.4.6a). When the pump detuning increases, we see two local maxima gradually merging into an absolute maximum corresponding to a perfectly aligned cavity. With these cavity parameters, and $\Delta_0/2\pi = -113GHz$, $\eta_{max} = -24.8dB$. Larger values of the pump detuning lead to the separation of this maxima again, meaning that FWM is no longer triply resonant. The cavity dispersion has been tuned too far from the frequency matching point. Consequently, the nonlinear efficiency drops rapidly. The second one is labeled Cavity #18. It starts with a larger initial detuning $\Delta\omega_{cold}/2\pi = 34GHz$, and with larger Q factors, $Q_{avg} = 120000$. The calculated nonlinear efficiency is shown in Fig.4.7a). We see that it requires a lot more pump detuning to align the cavity, which occurs at $\Delta_0/2\pi = -432GHz$. However, the larger Q factors allow to reach a much larger $\eta_{max} = -5.8dB$. The calculated spontaneous power is shown in Fig.4.7b). It represents the optical power radiated by the cavity. We see that the maximum reaches 150 pW for mode (+) and 50 pW for mode (-). This is due to different escape efficiencies, as defined in Eq.2.81. The maxima are reached for the same pump detuning as for the stimulated case, when the cavity is triply resonant.

These specific cavities do not possess Q factor high enough to reach parametric oscillation, but the model predicts that the thermal tuning enables to reach the maximal efficiency possible in each case. This will provide a basis to compare the experiment in order to validate the model.

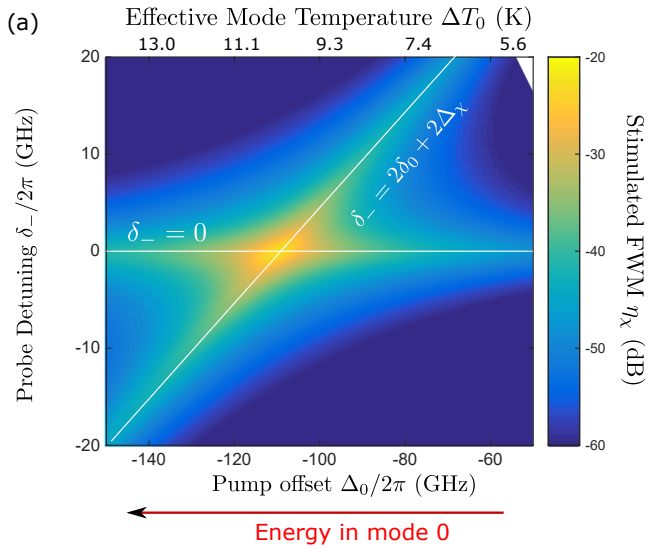

Figure 4.6: Cavity 27 a) Calculated map of the nonlinear efficiency of stimulated FWM as a function of the probe detuning and the pump detuning. The calculated rise of effective temperature of the pump mode is shown on the top axis.

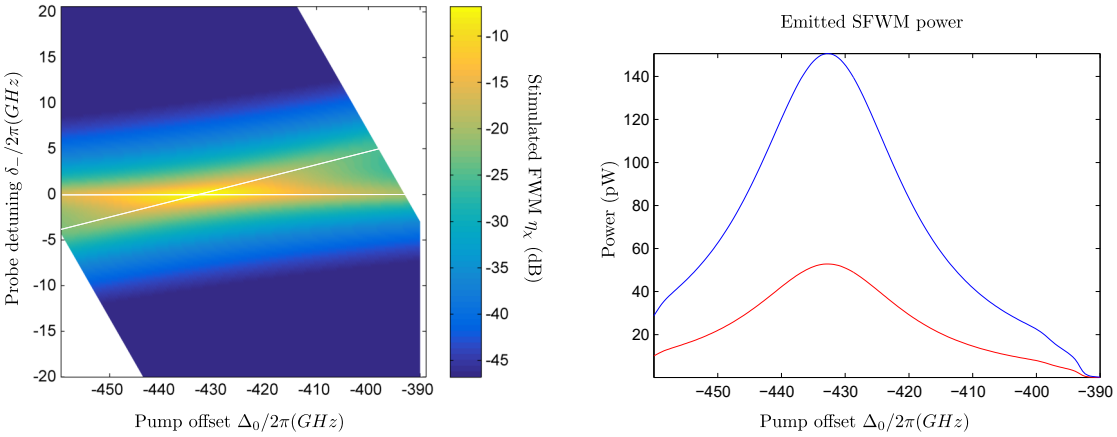

Figure 4.7: Cavity 18 a) Calculated map of the nonlinear efficiency of stimulated FWM as a function of the probe detuning and the pump detuning. b) Calculated spontaneous FWM power as a function of the pump detuning

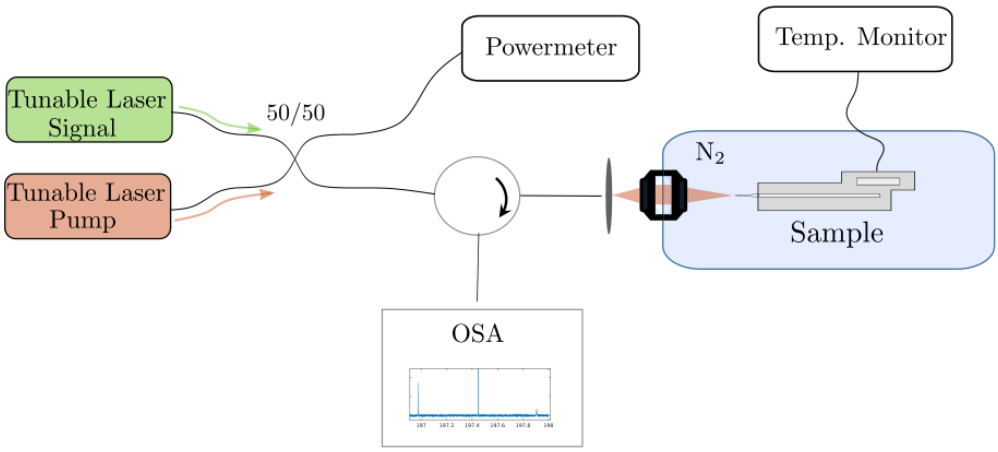

Figure 4.8: a) Experimental setup for stimulated FWM performed with two narrow linewidth ($< 0.1MHz$), mode-hop free tunable semiconductor lasers. They are combined before being injected in the sample. The output is sent in an Optical Spectrum Analyzer. All fiber components are polarization maintaining.

4.3 FWM in Bichromatic cavity

4.3.1 Experimental Setup

Once we have established that it is possible to bring the cavity into a triply resonant configuration, we now investigate experimentally the impact on the efficiency of FWM. We start with a setup for stimulated FWM, as it is easier to observe with low efficiency.

The experimental setup is pictured in Fig.4.8. Stimulated experiment are performed using two continuous wave tunable lasers, Santec TSL510 and Keysight 81606A. Here, the setup stays the same compared to the thermal pulling measurement, except that the OCT is replaced by a simple tunable laser. The sources are combined using a 90/10 coupler. The 10% output is used to monitor the power level as we described in the section above. The sample support is made of Copper and is thermally stabilized, same as for the linear measurements. The output of the circulator is connected to an optical spectrum analyzer (OSA, Yokogawa AQ6370). This OSA has a pW sensitivity with a noise floor of -80 dBm. In this particular setup, all the fiber components are polarization maintaining, which was not the case for the OCT. During all the measurements for the bichromatic cavities, the power level from the laser output is always below 10 mW CW, therefore FWM and other nonlinear effects are negligible both in the fibers and in the PhC waveguide. This power level is reachable directly with the output of the

laser. The absence of amplifier simplifies the experiment as no optical bandpass filters are used to ensure that the pump and probe have a narrow linewidth.

4.3.2 Extraction of the nonlinear efficiency

In the stimulated regime, the measure is separated in three steps. First, a low-power (few μW) scan is made to locate the cold cavity resonances. A symmetric dip in the reflection spectra is observed, consistently with the absence of thermal nonlinearity. This step gives the "cold" cavity dispersion.
Then, the pump power is switched into its nominal value of few mW. Its frequency is gradually red-detuned. The cavity frequency, locked to the laser frequency, is thermally pulled until the bistability jump occurs as can be seen in Fig.4.1. The recorded output power has a triangular shape, and this allows to locate the resonant frequency when the mode is pumped. This step gives the value of the "hot" pump frequency, and gives the maximum detuning for a given pump power.
Finally, the second tunable laser is turned on with a power at least 20 dB below the pump level. Starting form the "cold" resonance, the pump frequency is red-detuned step-by-step, and for each pump frequency, the signal is swept across the two sidebands. An optical spectrum is acquired for each combination of pump and probe settings. The measurement gives 3 power levels. The pump power is checked to see whether it is still resonant, as it is possible that mechanical vibrations kill the coupling. If the coupling is lost at some point , the whole procedure needs to be restarted, e.g. the thermal pulling from the "cold" values. We recall that the efficiency of the stimulated FWM is defined as:

$$\eta = 10log_{10}(\frac{P_{i,out}}{P_{s,in}}) \tag{4.12}$$

The power level are directly measured from the OSA spectra, assuming that coupling losses are equal for signal and idler. The minimal resolution of the OSA is 4 GHz, which is much larger than the laser linewidth or the cavity resonance linewidth. As a result, it is a good approximation to take the maximum peak power level, because it corresponds to an optical power that has already been integrated on a larger bandwidth than the signal itself. In these measurements, the OSA is used as a power-meter on frequency span equal to its resolution. Reducing the resolution of the OSA (down to 100 GHz for some measurements) gave the same value of η as expected, but allowed a much faster measurement.

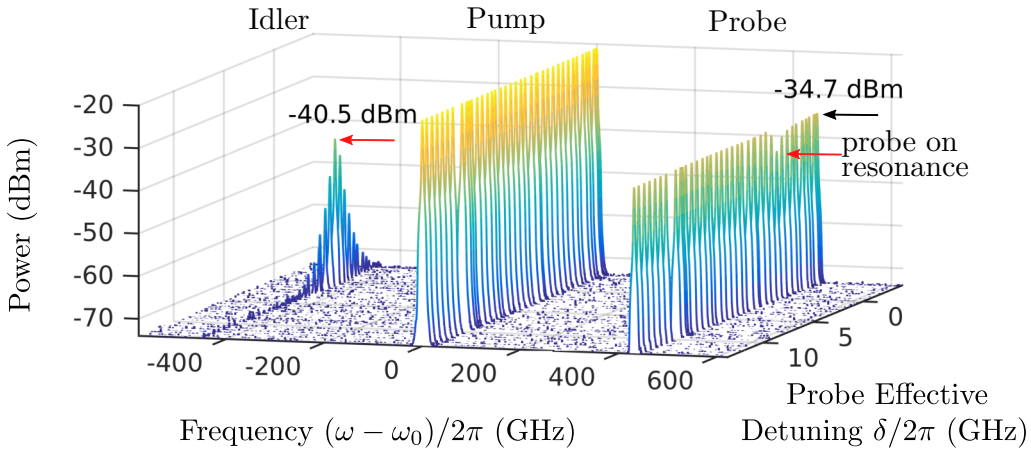

Figure 4.9: a) 3D map showing efficient stimulated FWM consisting in the concatenation of OSA trace for different probe detuning . The resonant nature of the FWM is highlighted. The power axis is expressed in dBm, and the frequency axis zeros are set by the detuning regarfding the pump ω_0 and the idler detuning to its hot frequency δ.

The signal power level is taken when the probe is off resonance, under the assumption that is light is totally reflected at the end of the access waveguide.
Observation of stimulated FWM is shown in Fig.4.9. On this example, the cavity has an average $Q = 1.2 \times 10^5$ and the pump power level is 80 μW. In this figure, the pump detuning is fixed and we see that the pump power level is constant, showing a stable coupling. The parameter varying here is the probe frequency that is swept across the higher order mode, ω_+. The off resonance power level is indicated by the black arrow, at -34.7 dBm. The red arrow on the probe side shows a dip in the power level, showing that the signal is at resonance. Simultaneously, the idler level is rising up to -40.5 dBm. This corresponds to a nonlinear efficiency $\eta = -5.8dB$.

4.3.3 Comparison with the theoretical model : scaling with the Q factor

The nonlinear efficiency shown in Fig.4.9 is already close to the oscillation threshold thanks to a relatively high Q-factor. Because the idler peak is built fast, a study of the cavity dynamics is difficult as each detuning step induces large changes.
Stimulated FWM is in this section, carried in the two different cavities that

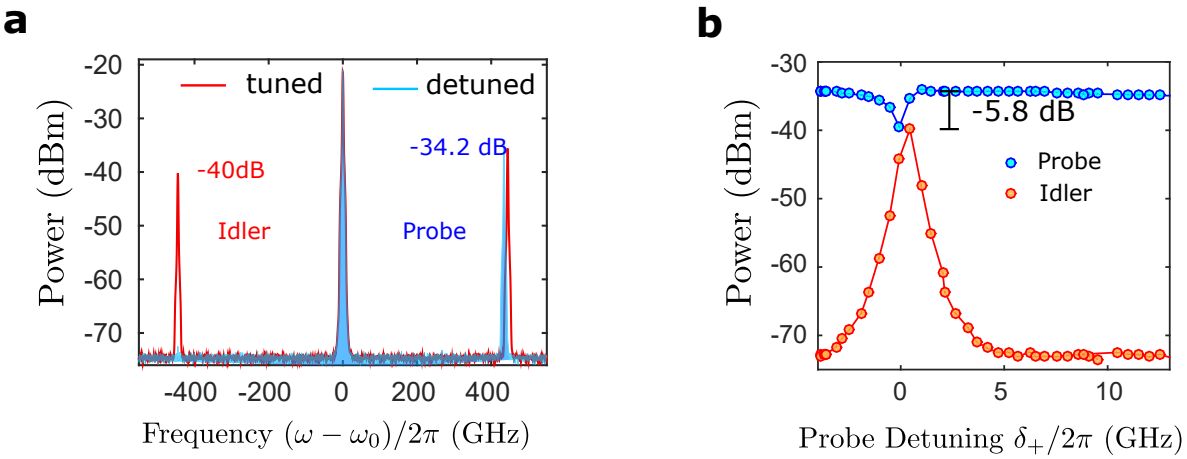

Figure 4.10: a) Superposition of two spectra extracted from 4.9. In blue, the probe is off resonant. In red, it is tuned into resonance, triggering FWM with an idler peak observed at -40 dBm. b) Evolution of the signal and idler power level as a function of the probe detuning δ when the cavity is aligned in a triply resonant configuration.

were simulated in Section 4.2.4. The cavity #27 has the lowest Q which corresponds to the highest FWM bandwidth. The original detuning of the cavity is $\Delta_\chi = 25.2GHz$ and the Q factor of the targeted modes (0, - , +) are respectively 67 000, 71 000 and 48 000. The on-chip pump power is set at 700 μW and the signal level is 20 dB lower. The measurement of the FSR of the modes from the OSA spectra are shown in the inset of Fig.4.11. We infer that the cavity is triply resonant when the pump mode is detuned by 110 GHz. The FSR are then equal to 345 GHz.

The extracted nonlinear efficiencies are shown in Fig.4.11a) as a function of the pump and probe detuning. The scaling is in % in order to illustrate the resonant enhancement. The colored curves of Fig.4.11a) are plotted in Fig.4.11b) in log scale. We are able to observe stimulated FWM when the pump is pulled on a span of about 40 GHz. At low efficiency, corresponding to the purple and green curves, η_χ has two peaks, which corresponds to the product of the Lorentzian function predicted in the model. It means that the cavity is not perfectly aligned and the resonances linewidths are large enough to permit FWM. These two peaks gradually merge up to one single maximum (red curve) corresponding to the maximum efficiency of $\eta_\chi = -25dB$, when the cavity is triply resonant. They are separated back when the pump is further

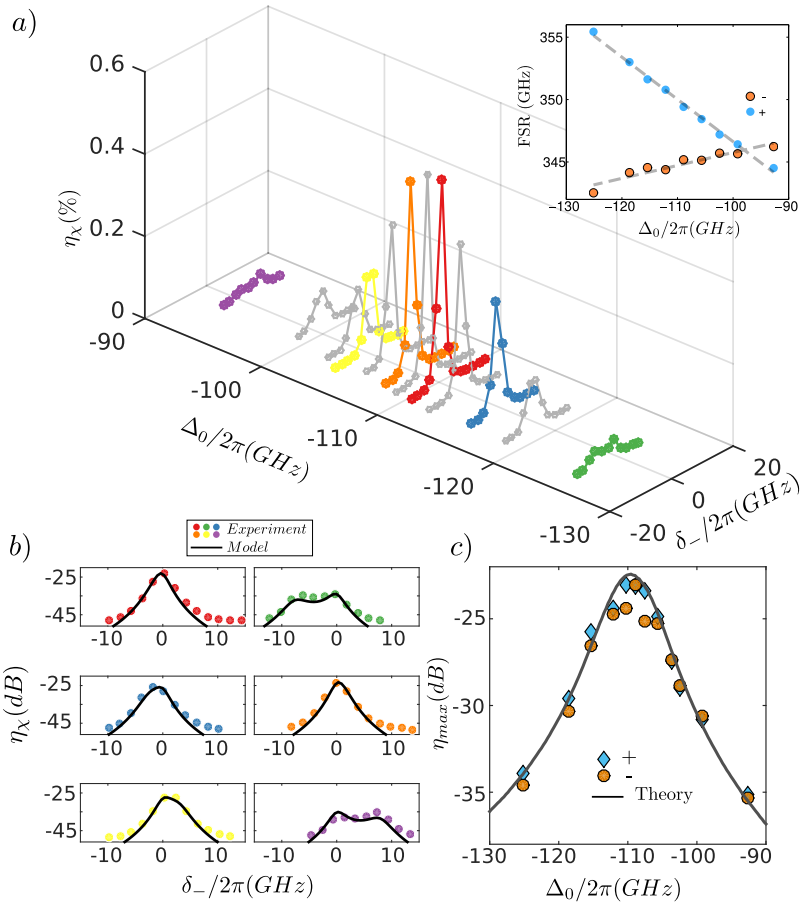

Figure 4.11: a) Nonlinear Efficiency as a function of the pump detuning Δ_0 and the probe detuning δ. The scale is linear to emphasize the impact of resonant enhancement. Inset: evolution of the corresponding FSR for the triplet of resonance. The slope of the dashed grey lines gives the thermo-optic coefficients of respectively 0.8972 and 0.6228 for the modes (-) and (+) . b) Comparison with the model, in black line, for the colored lines of the 3D plot. c) Maximum efficiency observed for each detuning of the pump, when the probe is either on the higher or lower order mode. The prediction of the model is showed with the black line.

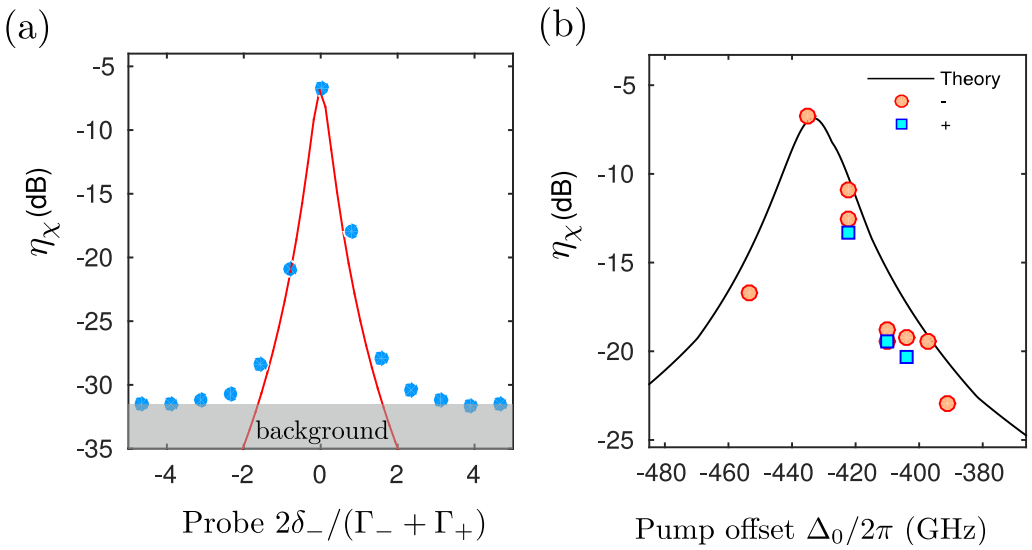

Figure 4.12: a) Measurement of the stimulated FWM efficiency for resonator with $Q_{avg} = 1.2 \times 10^5$ as a function of the probe detuning δ and b) the pump detuning Δ_0. The prediction of the model is represented in solid line. The background, higher than the noise floor indicates the presence of spontaneous FWM

detuned, up to skill the FWM process when $\Delta_0 = -130GHz$. The black lines on Fig.4.11b) are the prediction of the model where we have extracted the cavity parameters from the thermal pulling measurement represented in Fig.4.6. The only parameter adjusted in the model is the pump power which has been set to 800 μW in the model. The thermo-optic coefficient of the pump was set as a fitting parameter and the difference with the experimental value is about 3% . Fig.4.11c) shows the maximum value obtained for each pump detuning Δ_0 when the probe is tuned alternatively on the '-" and on the "+" eigenfrequency. From the model, we expected a symmetrical curve, that is effectively obtained here, in agreement with the theory prediction, represented in solid black line.

The procedure is repeated with the cavity #18. It has a larger average Q factor ($Q = 1.2 \times 10^5$) and initial mismatch $\Delta\omega_{cold} = 33.9GHz$. Again, quantitative agreement with theory is obtained as shown in Fig.4.12a) and b). The theoretical lines are extracted from the model presented in Fig.4.7a). As expected, we see a drastic improvement of the efficiency that rises up to 26 % (– 5.8 dB) with an on chip pump power of 80 μW. Fig.4.12b) also shows that the theory predicts well the efficiency level when the probe is switched on the mode (+) and (-). We note a higher background when the cavity is triply resonant as

presented in Fig.4.12a) which is induces a little discrepancy, due to the presence of spontaneous FWM.
From these experiments, we can conclude that we are able to exploit the thermal tuning technique to systematically reach the theoretical maximum value of η_χ allowed by the cavity, being only limited by its modal volume and Q factors. These experiments are also validating the approximation that we made to describe the cavity, in particular to neglect SPM and XPM over the thermo-optic effect.

4.3.4 Observation of spontaneous FWM

The properties of non-classical light generated through the spontaneous FWM process can be characterized indirectly from the measurement of the stimulated FWM[134]. In particular, the power level of the spontaneous emission has been calculated for ring resonators and shown to be related to the classical formula for the stimulated FWM. In the chapter 2, we adapted this relation for any type of cavity. We recall that one of the major modification was the introduction of a factor $\kappa/(\Gamma+\kappa)$ representing the fraction of internally generated pairs which are not lost due to internal losses. It implies that the emission rate from each mode is in general different.
Spontaneous FWM experiment are carried out by turning the probe laser off. A spectrum is recorded for each detuning of the pump Δ_0. For this measurement, the cavity #18 that was used to obtain $\eta_\chi = -5.8dB$ is studied. Linear measurements show that the mode "0" (pump) needs to be pulled by 430 GHz until $\Delta\omega_h = 0$ with an on-chip power level of 700 μW.
Fig.4.13a) ,b) shows the raw OSA traces when Δ_0 is varied. As the pump offset is adjusted close to -430 GHz, the spontaneous emission is easily measured from the "+" and "-" modes. Let us note that no optical band-pass filter is used here due to the absence of amplification stage. In addition, the spontaneous emission rate is large enough to be measured with the same OSA that was used for stimulated FWM. The pump level is here below 1 mW, which compatible with the dynamic range of the OSA. As a result, spontaneous and stimulated FWM can be compared with the same sources and detectors, which prevents the need for any relative calibration.
The power level of the spontaneous emission is extracted from the raw measurements and plotted as a function of the pump offsetΔ_0 in Fig. 4.13. The agreement

with the theory of Fig.4.7b), shown in black lines, is very good. The maximum spontaneous FWM power measured at the OSA from the mode "+" is about 30 pW (150 pW on chip when considering the insertion losses), corresponding to an on-chip rate of about 1 GHz. It is to be noted that spontaneous FWM is responsible for the high background in Fig. 4.13a). The predicted stimulated efficiency can be deduced from these spontaneous measurement. We approximated this relation in Chapter 2 Eq.2.72 where the spontaneous power is linked to the maximum efficiency η_{max}. Adjusting the pump power to 760μW gives a theoretical result of $\eta_{max} = -6dB$, which is very close to what we obtained experimentally. The corresponding generation rate for the outcoupled photons is 0.35 GHz for the mode (-) and 1.1 GHz for the mode (+). Remarkably, the pump power is only 60 dB higher than the generated pair power owing to the very high efficiency of the parametric process. This is of particular interest when on-chip filtering is needed.

Finally, let us note that we could observe spontaneous FWM in the cavity #27 with lower Q factors. However, the detected spontaneous power level was at the limit of sensitivity for the OSA so a comparison with the model was not possible.

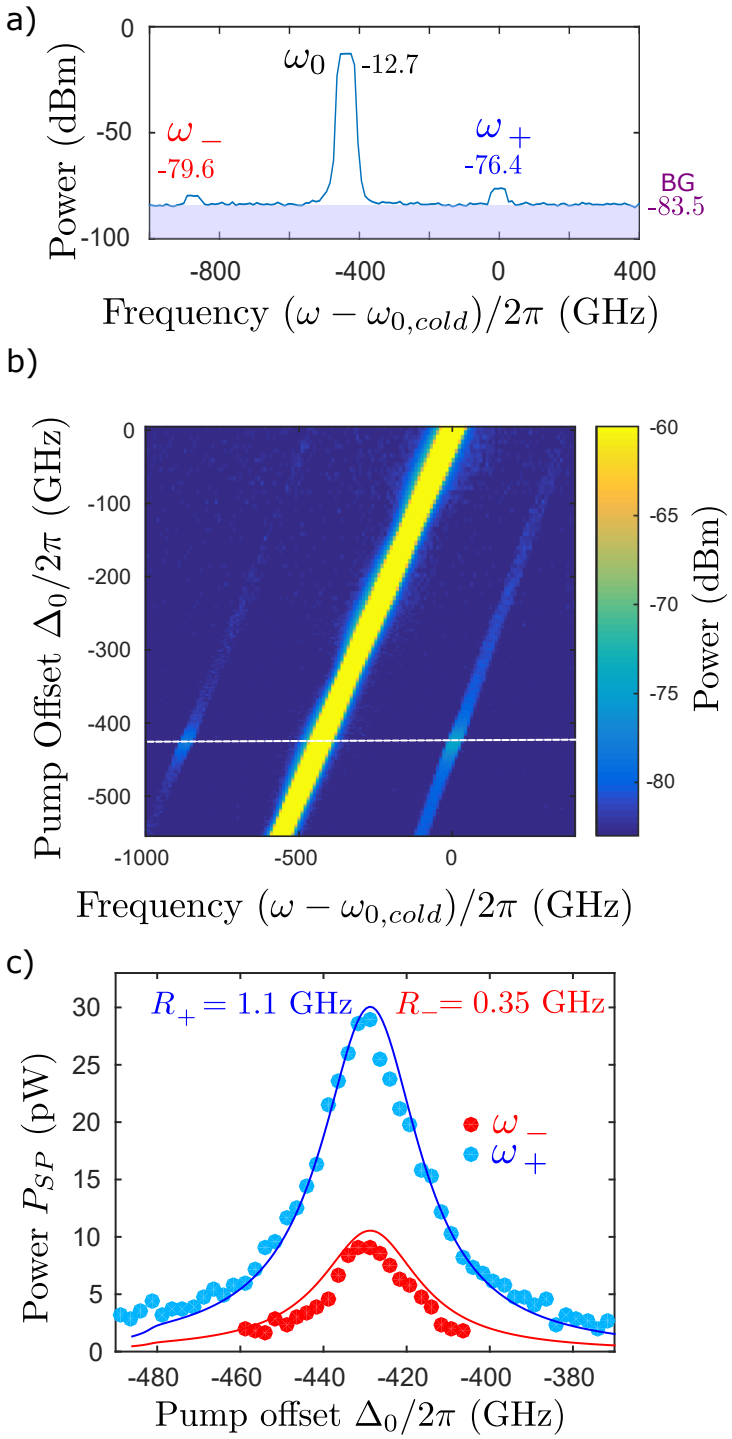

Figure 4.13: a) Raw spectrum (resolution is 100 GHz) of the spontaneous emission (+, -) the pump (0); the noise floor is represented by the shaded area (-83.5 dBm) (b) Raw spectra as a function of the pump offset represented by a false-color map. The dashed line corresponds to the plot in (a). The origin of the bottom axis is the cold resonance of the pump c) Spontaneous FWM on the Stokes and anti-Stokes side as a function of the pump offset. The solid lines are the theoretical predictions accounting 7dB insertion loss.

4.3.5 Observation of parametric oscillation in PhC

In the previous samples, parametric oscillation is not observed, meaning that the maximum realizable parametric gain is not sufficient to compensate for cavity loss. This value is entirely determined by the cavity optical properties (Q, mode volume, nonlinear cross-section, material nonlinearity) and the pump power level required to align the three modes. Its value is therefore unique for each triplet of modes. Eventually, parametric oscillation is demonstrated for a resonator with $Q_{avg} \approx 2.5 \times 10^5$. The sample is pumped with an on-chip power level below 200 μW, which is enough to align a triplet of adjacent resonances. The initial value of the pump frequency is 195.794 THz, and red-detuned to align the cavity. As the pump offset $\Delta_0/2\pi < -170$ GHz, the red ω_- and blue ω_+ signals emerge from noise (-73 dBm = 50 pW), as can shown in Fig.4.14. When approaching -175 GHz, they abruptly increase by four orders of magnitude, a clear indication of an oscillation threshold.

OPOs are generally characterized with the threshold power. This can be difficult in our case, as we cannot define a power injected in the cavity but an energy injected inside the cavity, with a constant pump power in the waveguide. It is nonetheless possible to define an equivalent power to the energy stored in the cavity. As we discussed, the pump offset is, to a good approximation directly proportional to the energy stored in the pump mode as the spectral shift is induced by linear absorption. The cavity resonance is then locked to the laser pump frequency, meaning that the relative detuning between the two is lower than the resonance linewidth. Because we pull resonances that are typically thinner than 1 GHz on a span ranging from tens to hundred GHz, we can make the approximation that the "hot" frequency of the cavity is equal the frequency of the pump laser:

$$\omega_h - \omega_{cold} \approx \omega_p - \omega_{cold} \tag{4.13}$$

The maximum energy inside the cavity corresponds to the case where the laser is resonant e.g. $\omega_p = \omega_h$ with a strict equality here. Experimentally, this is the frequency of the pump at which we observe the thermal bistability. Hence, we can approximate the energy of the cavity for any detuning of the pump by:

$$|a(\omega_h)|^2 = max(|a|^2)\frac{(\omega_h - \omega_{cold})}{(\omega_{bist} - \omega_{cold})} \tag{4.14}$$

The maximum $max(|a|^2) = \frac{4\kappa}{(\Gamma+\kappa)^2}P$. We can now define an equivalent power

circulating in the cavity as:

$$P_{c,0} = |a|^2 \frac{(\Gamma + \kappa)^2}{4\kappa} \tag{4.15}$$

With this, the result can be plotted in a more familiar representation by estimating an equivalent pump power circulating in the cavity $P_{c,0}$ in Fig.4.15. Above threshold $P_{c,0} > P_{th} = 175\mu W$, the on-chip generated power increases linearly with $P_{c,0} - P_{th}$. The threshold expected from our model is 170 μW.
The slope efficiency of each mode is respectively $dP^-/dP_0 = 0.2$ and $dP^+/dP_0 = 0.34$ More than 50% of the excess pump power is converted.
As the detuning is further increased, the parametric oscillation shuts off at $\Delta_0/2\pi$ = -183GHz, although the pump mode is still on resonance. The cavity is now misaligned. Cascaded FWM is unlikely to be resonant on all 4 cavity modes. No other mode appears to be involved in a parametric process, as we assumed in the theoretical model.
The energy inside the cavity is measured following the method described in Section 4.2.2, and estimated at $W = 48fJ$. 3PA is stronger than linear absorption at this level of energy, the limit case being measured at $W = 30fJ$. Because we could observe parametric oscillation at the expected power level, we infer that 3PA, in this case, displaced the point where frequency matching occurs, without degrading the Q factors of the cavity.

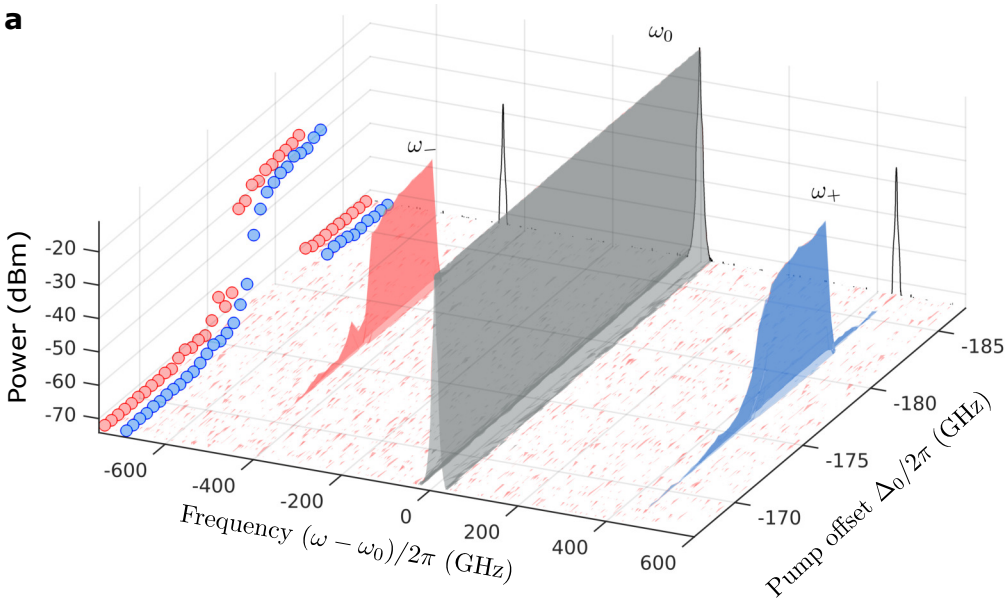

Figure 4.14: a) Parametric oscillation: raw optical spectrum (resolution 4 GHz, centered at the pump frequency) as the pump offset is changed. The threshold is overcome as the intra-cavity pump energy increases. Markers represent the raw power on the red and blue side, solid black line is the spectrum at maximum OPO emission;

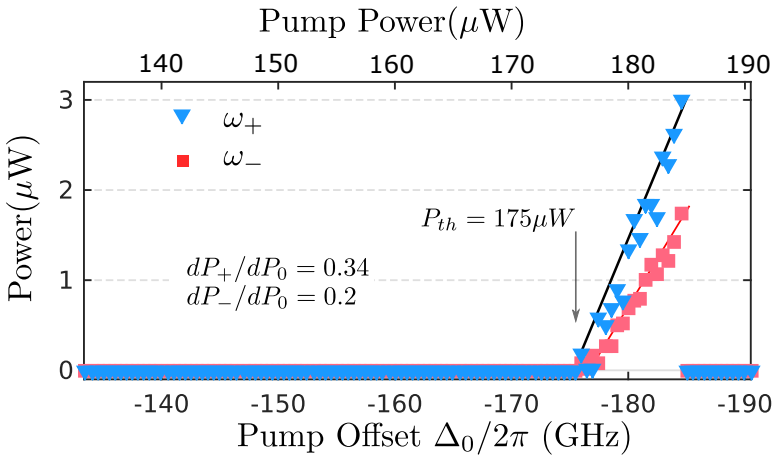

Figure 4.15: a) On-chip power in the blue ω_+ and red ω_-(markers) as a function of the pump offset and equivalent pump power in the cavity $P_{c,0} with a threshold of 175\mu$W. The solid lines indicate the slope efficiency of respectively 0.34 and 0.2 for the modes (+) and (-)

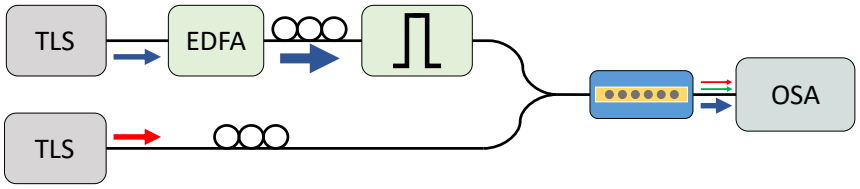

Figure 4.16: a) Experimental setup for nonlinear conversion measurements. TLS = Tunable Laser Source, EDFA = Erbium Doped Fiber Amplifier, OSA = Optical Spectrum Analyzer.

4.4 FWM in hybrid PhC on SOI

4.4.1 Experimental Setup

We now perform FWM experiment in our cavities on SOI. These cavities are accessed through a silicon waveguide, which is coupled to the outside via grating couplers. Hence, assuming same losses in the input and output gratings, the insertion losses are measured by dividing the total transmission by 2. Of course, the measurement is performed out of resonance. Due to an un-optimized grating design, the insertion losses typically reach a quite significant value of -17 dB to - 25 dB, meaning that each grating causes -8.5 to -12.5 dB.

The nonlinear measurements are performed using a cavity with a FWHM of 5 μm (total length of 60 μm). The interacting modes have a loaded Q factor of 97 000, 35 000 and 76 000 respectfully for the idler, pump and signal modes. It corresponds to an average Q, Q_{avg} = 55 000. The misalgnement of this triplet is 33.1 GHz. The pump has a lower Q factor because it is over-coupled to the waveguide, whereas the idler and pump are closer to the critical coupling. As shown in Fig. 4.16, the same two continuous (CW) tunable laser sources are used to provide the pump and signal, combined with a 90/10 coupler. The major difference compared to the suspended membranes is the need for amplification by an Erbium doped fiber amplifier (EDFA), followed by a bandpass filter. The insertion losses of this specific waveguide are estimated off resonance to be about -12.5 dB per grating coupler. At the output of the waveguide, we use again the same OSA to record the output spectrum.

4.4.2 Observation of stimulated FWM

We use the same thermal tuning as detailed for the suspended membranes. The main issue here is that the extent to what the pump mode can be pulled is limited by the bandwidth of the filter, hence the initial misalignment that can be compensated for. This technical limitation prevents a full thermal study as we did for the suspended membranes as well as it limits the range of cavities that are suitable for the experiment. The bigger thermal dissipation due to the bonding to silica tends to make the cross-thermo optic coefficients uniform which is another obstacle for the thermal tuning technique.

As seen in Fig4.17, when the signal is off-resonance, no idler peak is observed, disqualifying nonlinear generation in the Si waveguide. When the signal is tuned closer to resonance, we observe a dip in its transmitted power as expected. Simultaneously, an idler sideband is generated and reaches a maximum 13 dB above the noise floor when the signal is at resonance (see Fig. 4.17a)). From this observation, we can conclude that resonant wavelength conversion occurs in the nanobeam.

As we did for the suspended membrane, the nonlinear efficiency is estimated by taking the ratio of the maximum idler power over the transmitted signal power off resonance. However, because the cavity is symmetric with respect to the Si waveguide, the emission of the generated idler is supposed to be the same in the two direction of the waveguide. Thus, we must add 3 dB to the maximum idler power, which brings the total maximum on-chip efficiency up to – 12 dB for an estimated 3.16 mW pump power coupled in the SOI waveguide, as can be seen in Fig. 4.17b). By taking into account the nonlinear volume of the cavity, V_{FWM}= 40 $\left(\frac{\lambda}{n}\right)^3$, the maximum theoretical efficiency for the injected pump is calculated to be η_{th} = -3 dB. The discrepancy is about one order of magnitude in comparison to the measured value. This difference can be in part attributed to the nonlinear absorption (3PA) that could start to degrade the Q factors at such power level. This is not a certainty because we could not characterize the behavior of the cavity when it is thermally tuned. Hence we do not know yet if some specific effect occurs that would lower the nonlinear efficiency. This question is to be answered in future works on the nanobeam platform.

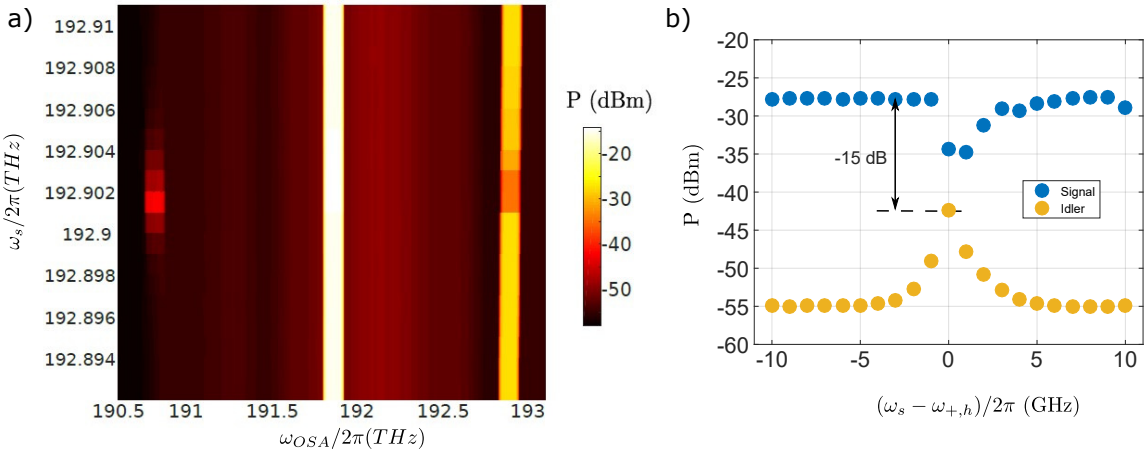

Figure 4.17: a) Map of the power intensity recorded for a fixed pump and a signal frequency $\omega_s/2\pi$ sweeping from 192.910 THz to 192.892 THz b) Extracted signal and idler power as a function of the position of the signal frequency $\omega_s/2\pi$ relatively to its resonance $\omega_{+,h}$.

4.5 Discussion of the results

4.5.1 Wavelength conversion in integrated platform

Before talking about parametric oscillation, we can place the result of both the nanobeam and bichromatic in the context of nonlinear frequency conversion in integrated devices and photonic crystals. For this, we add two new lines in the Table 1.2 of Chapter 1 comparing continuous FWM in PhC cavities. As can be seen in this updated Table 4.1, the results that we have obtained using the thermal tuning technique constitutes a record in term of absolute conversion efficiency compared to the previous record without tuning[92].

The study on the nanobeam cavity suffered from the poor coupling that we could obtain on the candidate cavities. We see that there is a lot of room for improvement here. Depending the application targeted, it still is a promising platform as it has two main advantages over the suspended membranes: the bonded structure can be more easily protected by dielectric encapsulation, and it can also withstand more optical power[135].

We can also see the advantage of a PhC structure when comparing to ring resonators in Table 4.2. The hybrid nanobeam cavity is comparable in terms of conversion efficiency with state of the art ring-based system, i.e. rings made in a thin AlGaAs layer bonded on SiO2/Si [32]. Despite a weaker nonlinear material ($n_2(AlGaAs) = 2.6 \times 10^{-18} m^2.W^{-1}$), the same efficiency is achieved with less

than twice the optical power on a much smaller footprint. It is a clear demonstration that PhC cavities can allow a larger conversion efficiency than in ring resonators for the same Q and input power due to their ability to confine light in a smaller volume.

Very importantly, the hybrid system also allows excellent insertion and collection of light in and out of the cavity as well as improved heat sinking compared to air bridged PhCs [135]. For these reasons, it is possible to insert higher power levels in the cavities that could induce a higher conversion efficiency. Indeed, in the other systems, the input power giving the maximum efficiency is limited by TPA in Si-based structures and/or by heat sinking in air-bridged ones. A more in-depth study of the impact of 3PA should be undertaken to see if this is the limiting factor for InGaP nanobeam. The performance of our device is reported on Table 4.2 together with that of ring resonators. The hybrid nanobeam cavity is comparable in terms of conversion efficiency with state of the art ring-based system, i.e. rings made in a thin AlGaAs layer bonded on SiO2/Si [32], but the result is obtained for a weaker pump power within a footprint which is 30 times smaller. It is a clear demonstration that PhC cavities can allow a larger conversion efficiency than in ring resonators for the same Q and input power due to their ability to confine light in a smaller volume.

Geometry	Material	Q_{avg}	On Chip power (μW)	η_{NL} (dB)	Ref.
1D PhC (3 coupled cavities)	Si	4000	60	-55	[90]
2D PhC CROW	Si	600 000	100	-35	[91]
2D PhC CROW	InGaP	70 000	36	-24	[92]
Nanobeam	InGaP	55 000	3160	-12	*This work*
Bichromatic	InGaP	120 000	80	-5.8	*This work*

Table 4.1: *Comparison of continuous wave FWM nonlinear efficiency conversion in PhC cavities. (CROW: Coupled Resonators Optical Waveguide)*

Geometry	Material	Q_{avg}	On Chip power (μW)	η_{NL}(dB)	Footprint (μm^2)	Ref.
Ring	Hydrex	10^6	6160	-26	5730	[136]
Ring	Si - graphene	9000	8000	-37	314	[137]
Ring-CROW	Si	x	100 000	-21	4140	[138]
Ring	AlGaAsOI	44 000	7000	-12	929	[32]
PhC on SOI	InGaP	55 000	3160	-12	39	*This work*

Table 4.2: *Comparison of continuous wave FWM nonlinear efficiency conversion in integrated devices. (CROW: Coupled Resonators Optical Waveguide)*

4.5.2 Parametric oscillation in integrated platform

In a similar way, the performance of the PhC OPO is already comparable to that of recently demonstrated semiconductor microring and racetrack OPOs which exhibits power thresholds between 30 μW and 25 mW, as shown in Fig.4.18. The very low power threshold of the PhC OPO results from the strong confinement of the interacting modes, the large nonlinearity of semiconductors and a moderately large Q factor. The mode volumes of about $0.2\mu m^3$, are 150 times smaller than in ring resonators with comparable FSR [1]. So far, lower power thresholds were observed very recently[35] in AlGaAs based microring (36 μW), thanks to a larger nonlinearity of the material, much higher Qs and a larger FSR. Lower values (down to 5 μW) are only reported in non-integrated and non-semiconductor resonators that require highly optimized fabrication process[139] and second order nonlinearity. Considering that current state-of-the art PhC cavities[77] exhibit $Q > 10^7$, OPOs with power thresholds below the μW level can be realistically considered.

[1] $V_m = 30\mu m^3$ for FSR = 500 GHz[34] Considering the interaction volume $V_\chi = 5.7\mu m^3$, this is still an order of magnitude smaller than $V_{\chi,ring} = 1.54 \times 2\pi A_{eff} L = 50\mu m^3$.

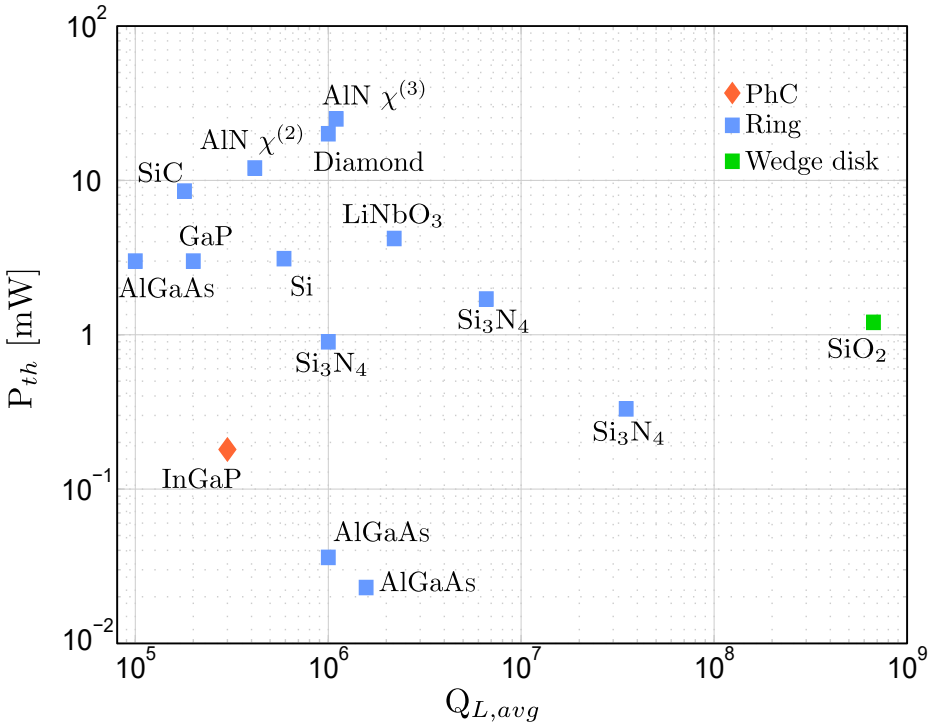

Figure 4.18: a) OPO pump threshold as a function of the averaged Q factor Q_{avg} measured in this work compared with state the art in microring and racetrack resonators made of different materials

As we discussed in Chapter 1, the power threshold is not the only figure of merit that needs to be considered in an OPO. The slope efficiency and the overall energy efficiency transfer from the pump to the side modes are crucial when it comes to practical application. In our case, the estimated total generated power, when considering out-coupling loss (7dB) is about 5 μW leading to a conversion efficiency which is about 2.5% of the coupled pump power. This value can be compared to the one of 17 % very recently reported in AlN ring resonators[37], which are operated at much larger power (10 mW) and exploit the $\chi^{(2)}$ nonlinearity. However, the PhC OPO measured slope efficiency (signal+idler) is above 50%. It is limited by the escape efficiency, indicating that a much better overall efficiency is possible by optimizing the coupling to the feeding waveguide without changing the low threshold.

4.5.3 Consideration on the footprint

Comparing the size and the scaling of a device can be difficult. Indeed, Footprint, Mode Volume and Interaction volume are related but different concepts. The footprint of the bichromatic resonator is here $20 \times 6\mu m^2$, including coupling waveguide. The minimal size of the PhC is set by the radiation losses limit, namely the capacity of the PhC to block radiation leak such that the Q factor is as large as the material and the fabrication allows. With this size, the radiation limit for the first 3 modes is above $Q > 10^6$. We note that multiple resonators could be packed to a minimal distance which is about half the footprint (hence 3μm on the side and 10 μm on the axis) without suffering from cross talk. This should be compared with the footprint of a microring with corresponding FSR, namely 430 GHz, which (scaling up the AlGaAs on Oxide ring in ref. [35]) leads to diameter = $24\mu m \times$ 1 THz/430 GHz = $55\mu m$.
However, as far as light-matter and nonlinear interaction are concerned, the mode volume and the nonlinear interaction volume V_χ should be considered. In this case, the nonlinear volume of our cavity is 5.7 μm^3, whereas $V_{\chi,ring} = 1.54 \times 2\pi A_{eff} L = 50\mu m^3$ for a ring with same FSR (500 GHz). The nonlinear volume is deduced from the formula relating the oscillation power threshold to Q factor and nonlinearity of the material. The interaction volume is one order of magnitude smaller here. This explains why, despite a smaller nonlinearity, $n_2(InGaP)/n_2(AlGaAs) = 0.7/2.6 = 0.27$, and smaller Q, (250k vs 1 M). A fair comparison would entail the same Q factor, same material and same FSR. For instance, a PhC cavity with FSR = 1 THz, the same as reported in Ref [35], would be $10 \times 5\mu m^2$ large approximately and the interaction volume will be reduced accordingly, and so the power threshold.

Conclusion

In this chapter, we have tackled the issue raised of structural disorder induced by PhC the PhC fabrication flow with the introduction of a thermal tuning technique. This tuning takes advantage of the Hermite-Gauss-like modal structure of our cavities to adjust the dispersion of the cavity. It is realized by thermally pulling the pump with a thermo-refractive phenomenon up to the point where the cavity is aligned. Due to the sign of the thermo-optic coefficient in InGaP, the tuning method can only compensate for negative dispersion. Local heating of the cavity could be used to replace the need for a tunable laser.
We then characterized the properties of our cavities to determine the thermo-optic coefficients and the injected energy. These parameters, together with the linear properties of the cavity determined in Chapter 3, allowed the modelling of the thermal and nonlinear efficiency according to the model derived in Chapter 2.
FWM experiments were then conducted in both bichromatic and nanobeam cavities with record high efficiencies. The measurements agree extremely well with the simulation, and parametric oscillation was reached in the bichromatic cavity with a threshold of 170μW, a value on par with state-of-art integrated ring resonators. In the nanobeam platform, a nonlinear efficiency of -12 dB was demonstrated. In this specific platform, there is a lot of room for improvement, in particular regarding the coupling efficiency of the gratings. Indeed, silicon gratings with coupling efficiency below -1 dB were recently demonstrated[140]. This could remove the need for amplification and considerably facilitate any further study. However, this issue does not rule out the nanobeam as a viable option because all these devices are meant to be integrated on chip together with a source delivering few mW. Hence the out-coupling power of the signal and idler is more interesting to improve, although we have seen that the PhC OPO performs already very well regarding this aspect.

Conclusion

The emergence for integrated photonics has largely been driven by the growing demand for energy efficiency and compactness. Incidentally, this has greatly favoured the renewal of consideration for nonlinear optical processes as essential functions in on-chip signal processing and integrated quantum optics involve such effects. Nonlinear interactions are triggered when a certain level of energy density inside the device is reached. This threshold has become easier to attain thanks to the progresses in material growth and micro-fabrication techniques and the achievement of diffraction limited confinement. Whether in waveguides or cavities, on-chip parametric processes have been widely studied and their efficiency improved. When it comes to compare the different platforms, two distinct aspects are to be taken care of. First, the performances of the material, and second, the performances of the confining structure. In this work, we limited the study to resonant $\chi^{(3)}$ effects, and specifically Four Wave Mixing with the aim to reach parametric oscillation. The trade-off here consists in benefiting the enhancement of light-matter interaction provided by the cavity with more flexibility in the design than it would have been with stronger but more complicated to implement $\chi^{(2)}$ effects (due to the much larger frequency difference between pump and signal/idler) .

Silicon has very interesting optical properties, including a large refraction index and nonlinear coefficient. However, they come with large nonlinear losses (TPA, FCA) at telecom wavelength that compel sophisticated workaround when it comes to parametric light generation (in a similar fashion as when it comes to lasing). A variety of wide bandgap materials have been considered and III-V materials are amongst the most promising one. Indeed, they combine large linear and nonlinear index which allow strong confinement and strong parametric interaction. InGaP was the material used in this work, but the same approach could be adapted to other semiconductors.

The vast majority of parametric interaction in cavities is carried out in ring

and race track resonators due to the easy dispersion control and high quality factor they provide. Photonic crystals are an alternative solution for strong light confinement in volumes close the the diffraction limit. Their confinement mechanism based on multiple constructive reflections in a patterned lattice allows extremely high Q/V ratio, but the same mechanism is very sensitive to defect in the periodicity of the lattice. As a result, it has be very challenging to engineer the dispersion of the cavity. The reported results prior to this work yielded poor efficiencies. Yet the objectives of this thesis were to investigate the possibility to overcome these limitations and exploit the promising properties of PhC cavities.

The first step of this work was to correctly model the system using nonlinear temporal coupled mode theory. The main difference with other resonators here, is that the coupling and the thermo-optic coefficient of all the modes can be very different. We also made the choice to neglect any other contribution than the thermo-optic effect in the shifting of the dispersion of the cavity. Finally, a correspondence between spontaneous and stimulated emission was proposed, later on experimentally confirmed. With the range of parameters already accessible in sate-of the-art PhC fabrication technology, parametric oscillation was found to be already reachable on paper.

The second step was to actually design and fabricate a PhC cavity that supports equally spaced mode and a high Q/V ratio. We proposed a solution based on a parabolic potential for the electromagnetic field, in analogy wit the quantum harmonic oscillator. The eigenfrequencies are equally distributed while the Q factors remain radiation limited. This was realized in suspended membranes concurrently to the beginning of this work, with the adaptation of the Bichromatic design to multi-modal cavity, which I could replicate. A different approach toward greater integrability was proposed with the realization of hybrid structure: the nanobeam on SOI. Although arising from a different reason, a parabolic potential also allows to have the right dispersion in these cavities. Fabrication and characterization of the samples evidenced the control over the coupling on these structures by varying the width and distance of the silicon waveguide. We also showed that despite the design, fluctuations on the targeted resonant frequencies were one order of magnitude larger than the four wave mixing bandwidth authorized by the linewidth of the resonances. As things stand, the fabricated devices could not be directly used for nonlinear experiment.

The last step before the aforementioned nonlinear experiment consisted in tuning the dispersion of the cavity so that at least three modes became equally spaced. The mechanism of dispersion tuning studied relies on the non-homogeneous distribution of energy of the modes. It allows a differential thermo-optic effect of the side modes when the pump mode is thermally locked and detuned. As a result, we showed systematic alignment of three (and only three) resonances provided that the original dispersion is anomalous (FSR increasing with the frequency). Using this thermal technique, we were able to validate the theoretical model describing the system in stimulated experiment that already constituted a record high nonlinear conversion value (up to - 6 dB in bichromatic and - 12 dB in nanobeam). When the Q factor was increased, parametric oscillation was eventually reached with a sub-mW threshold (170 μW) already comparable with state-of-the art ring resonators., with a slope efficiency above 50%.

The results presented in this thesis are the outcome of many research years of works on PhC technology in the group. Several points of further investigation could be addressed, among which we can mention:

- demonstrating OPO on a hybrid structure. The weak coupling efficiency in the SOI waveguide compels the use of an EDFA, which complicates the thermal tuning tuning (gain bandwidth of the EDFA, necessity to filter the pump) but is not impossible. The better heat sinking of bonded structure can also increase the power level for alignment. Hybrid bichromatic cavities can also be considered.

- reduction of the losses in the hybrid structure. As we already mentioned, the sputtered silicon dioxide layer is the current limit for Q factors in hybrid structures. We investigated different solutions and baked HSQ provided much better results. PhC cavities are still to be fabricated but we expect a drastic improvement Q factors, that could be comparable to suspended membranes.

- quantum light generation. In this work, we could only observe spontaneous generation. A more detailed study on squeezing, heralded or entangled photons would be interesting. The brightness of the source and large pump rejection already observed, together with a possible engineered collection rate, are as many factors that make PhC a good quantum source.

- alternative tuning scheme. We have used the pump-induced heat to change the dispersion of the cavity. A scheme with a fixed pump laser and local electrical heaters could be imagined.

- can the system of coupled cavities tuned by a holographic pattern as in [99] reach a triply resonant configuration? Here, the dispersive nature of evanescent coupling in PhC cavities might be an issue for achieving a perfectly aligned triplet[141].

Be that as it may, the thermal tuning technique opens exciting new possibilities to fully exploit the capacities of PhC nonlinear microcavities, and a PhC based parametric source of light provides an interesting tool for future and fruitful studies.

Annexes

Appendix A

Linear characterization with OCT

In this annex, we describe the Optical Coherent Tomography (OCT) setup that is used for the linear characterization of the samples. This set-up has been continuously improved at Thales[142] and was used to characterize PhC waveguides[143] or cavities[120]. We start by detailing the optical setup, then how to extract and analyze the complex spectrum. Finally, we will explain how to correct the measurement of frequencies with a gas cell reference.

A.1 Principle of measurement

An OCT measurement is an interferometric measurement. Indeed, the quantity that we aim to extract is the complex spectrum of the device and not only the intensity. If we have access to the complex field, we can perform a Fourier analysis that, supported by the adequate CMT model, allows us to retrieve both the coupling and the intrinsic losses of the cavity.

A.2 OCT setup

The experimental setup is shown in Fig.A.1. It relies on a continuous wave laser source (TSL Santec 510C) which is swept without mode hops to probe the sample. The input is first separated in 2 channels by a 90/10 coupler: one to the sample and one to a reference interferometer. The connections are made to match the level of signal required at the detection end. In most cases, only 10% of the input power (corresponding to approximately 100 nW coupled to the sample) is necessary. The Michelson reference interferometer has a fixed unbalanced arm ($\delta = 5$ m). Its purpose is the measurement of the instantaneous

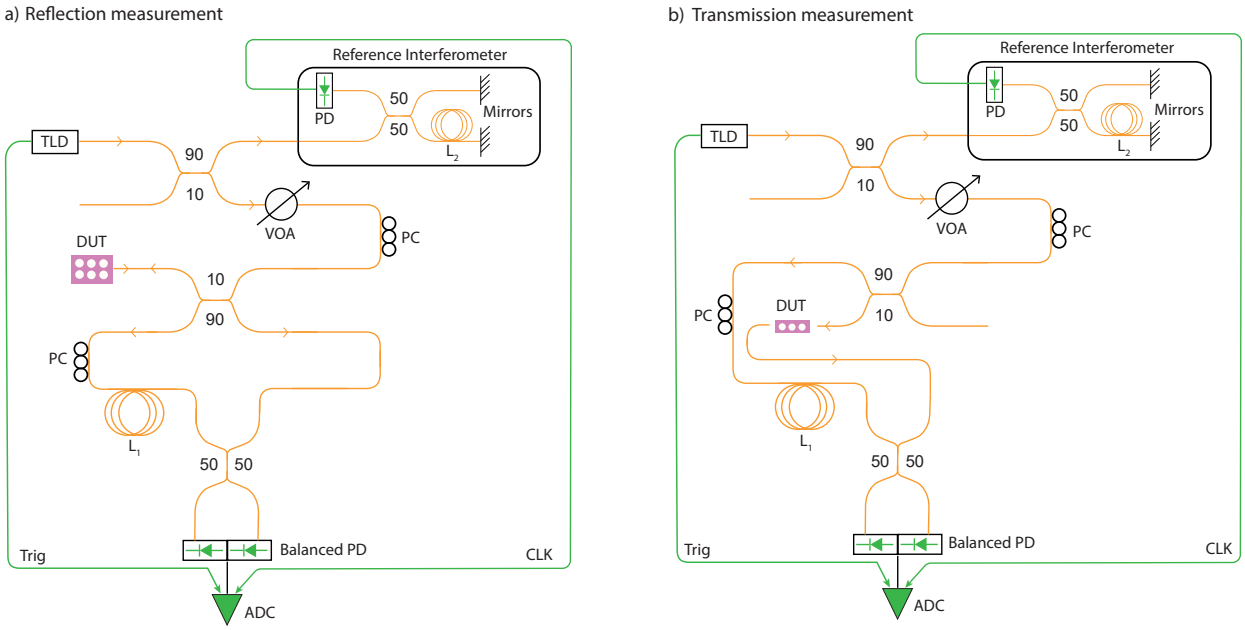

Figure A.1: a) OCT setup for the measurement of the complex reflection spectrum of the cavity b) OCT setup for the measurement of the complex transmission spectrum of the cavity. TLD: Tunable Laser Diode VOA: Variable Optical Attenuator PC: Polarization Controller DUT: Device Under Test PD: Photodetector ADC: Analog To Digital Converter. The mirrors of the reference interferometer are Faraday Mirrors. The respective length of fiber are $L_1 = 8$ m and $L_2 = 5$ m

wavelength of the source generating as a clock signal for the acquisition of the sample spectrum.

The interferometer that measures the sample characteristics is configured as a Mach-Zender for transmission measurements and a Michelson for reflection measurements. A variable optical attenuator is used at the output of the 90/10 coupler to adjust the power level. A second 90/10 coupler is used to split the OCT probe to the sample and the reference arm. Both signals are recombined thought a 50/50 beam splitter and connected to a balanced photodetector for homodyne detection. The resulting signal is acquired by an ADC card (AlazarTech 460).

A.3 Fourier analysis of the signal

The light from the TSL constitutes the input for the system. Assuming a linear frequency sweep $\nu(t) = \nu_0 + \gamma t$, the laser output can be written:

$$E(t) = E_0 e^{\imath 2\pi[\nu_0 + \gamma/2t]t]} \tag{A.1}$$

We consider only the signal in the main interferometer. This signal is split in the two arms (labeled 1 and 2) of respective delay τ_1 and τ_2. In the second arm, the signal is also multiplied by the transfer function of the cavity $H(\nu) = d(\nu)e^{\imath\phi(\nu)}$ where $\phi(\nu)$ is the complex phase and $d(\nu)$ is the complex amplitude that can be, depending on the measurement:

$$d(\nu) = \begin{cases} t(\nu) & \text{if transmission measurement (side-coupled cavity only)} \\ r(\nu) & \text{if reflection measurement (side-coupled and single-ended cavity)} \end{cases}$$

After recombination of the two arms, and assuming a perfect 50/50 beam splitter, the detected signal is :

$$\begin{aligned} S(t) &= |\frac{E(t-\tau_1)}{\sqrt{2}} + H(\nu)\frac{E(t-\tau_2)}{\sqrt{2}}|^2 \\ &= \frac{E_0^2}{2}(1 + |H(\nu))|^2 + 2Re[H(\nu)e^{\imath 2\pi\gamma\tau t + \psi}]) \end{aligned} \tag{A.2}$$

where $\tau = \tau_1 - \tau_2$ is the delay between the two arms and $\psi = 2\imath\pi(\nu_0\tau + \gamma/2(\tau_1^2 - \tau_2^2))$ is a phase constant.
The offset term $1+|H(\nu))|^2$ does not convey any information about the complex spectrum, and is removed during the homodyne detection. Using the relation $t = (\nu-\nu_0)/\gamma$, one can express the fringes equation as a function of the instantaneous frequency:

$$S(\nu) = E_0^2 d(\nu) cos(2\pi\tau\nu + \phi(\nu) + \psi') \tag{A.3}$$

with $\psi' = \psi - 2\pi\nu_0\tau$ the new phase constant. The fringes are modulated both in amplitude and phase by the complex transfer function of the cavity. The recorded interferogram is then inverse Fourier transform. A Hilbert transform is then performed to remove the negative temporal components, which corresponds to the mathematical operation:

$$R(t) = S(t) + sign(t)S(t) \tag{A.4}$$

A temporal filter is then applied, to remove the artifacts and the noise generated by the detector. Finally, the result is put back in the spectral domain via another Fourier transform, which gives the complex transfer function of the cavity. Let us note that the Hilbert and filter could be applied in the spectral domain as well, but we chose the mathematically equivalent procedure explained above, because it is easier to identify the artifacts in the temporal domain.

A.4 Interpretation of the measurement

Once we have extracted the complex transfer function, we have now to link it to the characteristics of the cavity. To do so, we use the linear TCMT model introduced in the Chapter 2. The transfer function expression depends on the coupling scheme, side-ended or side-coupled.

A.4.1 Single-Ended cavity

In the single-ended scheme, there is no transmitted wave, the coupling in and out is realized through the same waveguide portion. Hence, $d(\nu) = r(\nu)$ is the complex reflectivity of the cavity. It corresponds to exactly the same model as in Eq.(2.15) recalled here:

$$\partial_t a = (-\imath\delta - \frac{\Gamma_0 + \kappa}{2})a + \imath\sqrt{\kappa}s \tag{A.5}$$

The reflected wave is:

$$s_r = s + \imath\sqrt{\kappa}a \tag{A.6}$$

The transfer function in reflection $H(\nu) = s_r/s$ is expressed at steady state. The complex amplitude is equal to :

$$a = \frac{\imath\sqrt{\gamma}}{\imath\delta + \frac{\Gamma_0+\kappa}{2}}s \tag{A.7}$$

which yields:

$$\begin{aligned} H(\nu) &= \frac{s_r}{s} \\ &= 1 + \frac{\imath\sqrt{\kappa}a}{s} \\ &= \frac{2\imath\pi\nu - z}{2\imath\pi\nu - p} \end{aligned} \tag{A.8}$$

where $z = 2\pi\imath\nu_0 + \frac{\Gamma_0-\kappa}{2}$ and $p = 2\pi\imath\nu_0 + \imath\frac{\Gamma_0+\kappa}{2}$ are the zero and the pole of $H(\nu)$. As we expected, the dip in the amplitude spectrum is maximal at resonance in

the critical coupling regime ($\kappa = \Gamma_0$) when the reflectivity reaches 0.
By definition, the group delay is linked to the phase of the complex transfer function by the relation:

$$\tau_g = -\frac{1}{2\pi}\frac{d\phi(\nu)}{d\nu} = -Im\left[\frac{1}{2\pi H(\nu)}\frac{dH(\nu)}{d\nu}\right] \tag{A.9}$$

With a zero/pole expression like (Eq.(A.8)), the group delay yields

$$\tau_g = Im(p-z)\frac{(2\pi\nu)^2 - Im(p)Im(z)}{|2\pi\nu - p|^2|2\pi\nu - z|^2} \tag{A.10}$$

This result can be applied with any transfer function written with a zero/pole model.
In the single-ended case that we consider here, this expression at resonance ($\nu = \nu_0$) is:

$$\tau_g = \frac{4\kappa}{\kappa^2 - \Gamma_0^2} \tag{A.11}$$

It is interesting to note that depending on the coupling regime of the resonator, the sign of the group delay is different: positive when $\kappa > \Gamma_0$ and negative when $\kappa < \Gamma_0$. At critical coupling, when $\kappa = \Gamma_0$, the group delay diverges.

A result of the measurement can be seen in Fig.A.2. In the top panel, we see the reflectogram of a bichromatic cavity (commensurability parameter a'/a = 0.98). Around 190 THz (1580 nm), we see the dispersion of the PhC waveguide near the band edge. Starting around 193 THz and up to 195 THz, we see the resonance lines of the cavity. The dynamic of the measurement is 50 dB. The first 4 resonances are shown in the bottom panel. The amplitude spectrum allows to extract the total losses (loaded Q). Due to the dispersive nature of the coupling with a PhC waveguide, the coupling regimes changes with the frequency, from undercoupled (red) to overcoupled (orange) with a crossing to the critically coupled resonance (green). The coupling regime is well predicted by the CMT model and we observe the predicted change in the sign of the group delay.

A.4.2 Side-Coupled cavity

In the side-ended scheme, the cavity can emit light in both side of the waveguide. Thus, both a transmission or reflection measurement are possible. If we assume a symmetric system, the coupling/emission rate in each direction is $\kappa/2$ and the

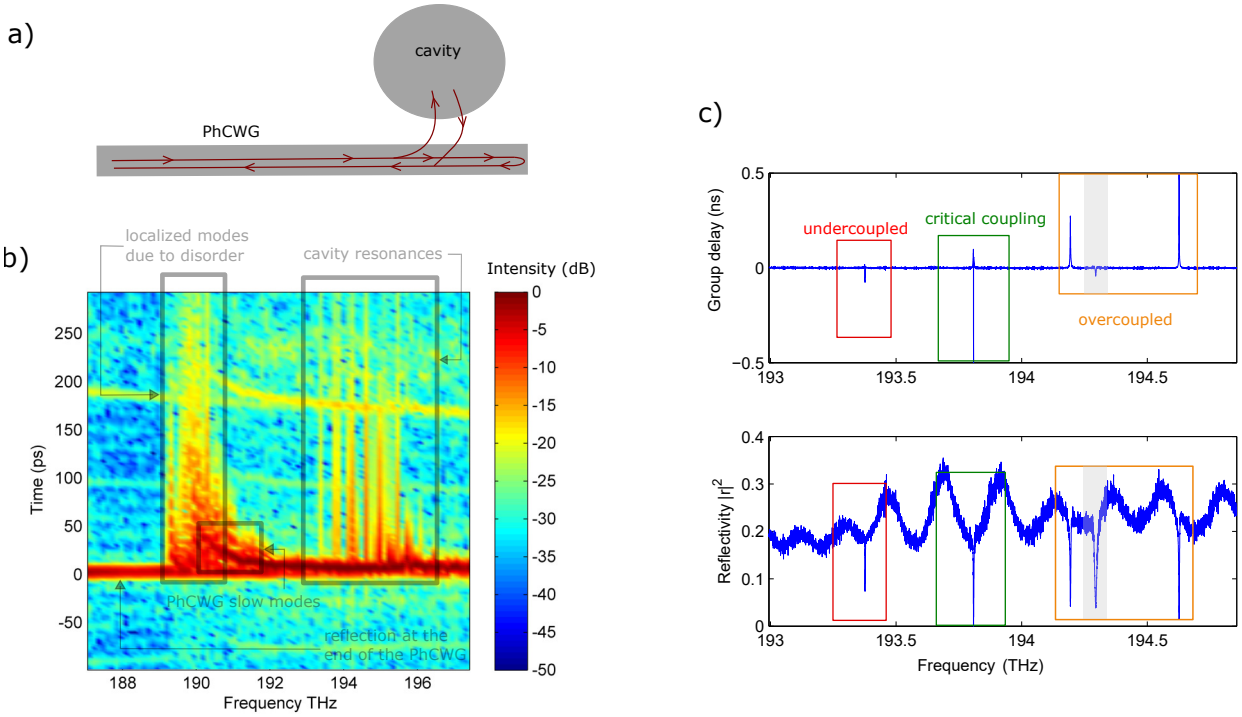

Figure A.2: a) Schematic of the bichromatic coupling configuration (reflection) b) Spectrogram of the reflected signal of a bichromatic cavity and c) the complex spectrum with the group delay and amplitude showing the transition from undercoupled to overcoupled regime. The grey shaded area is a defect in the sample and not a cavity resonance.

total coupling rate is still κ. The TCMT equation are modified accordingly:

$$\partial_t a = (-\imath\delta - \frac{\Gamma_0 + \kappa}{2})a + \imath\sqrt{\frac{\kappa}{2}}s \tag{A.12}$$

The reflected and transmitted waves, respectively labeled s_r and s_t are:

$$s_t = s + \imath\sqrt{\frac{\kappa}{2}}a \tag{A.13}$$

$$s_r = \imath\sqrt{\frac{\kappa}{2}}a \tag{A.14}$$

The transfer function can be either in transmission (noted $H_t(\nu)$) or in reflection (noted $H_r(\nu)$).

$$\begin{aligned} H_t(\nu) &= \frac{s_t}{s} = 1 + \frac{\imath\sqrt{\frac{\kappa}{2}}a}{s} = \frac{2\imath\pi\nu - z}{2\imath\pi\nu - p} \\ H_r(\nu) &= \frac{s_r}{s} = \frac{\imath\sqrt{\frac{\kappa}{2}}a}{s} = \frac{\imath\kappa/2}{2\imath\pi\nu - p} \end{aligned} \tag{A.15}$$

with $z = 2\pi\nu_0 + \imath\frac{\Gamma_0}{2}$ and $p = 2\pi\nu_0 + \frac{\imath(\Gamma_0+\kappa)}{2}$. The minimum amplitude is once again reached at critical coupling but the dip does not go to 0 but to 25% of the transmitted signal.

The group delay at resonance is :

$$\begin{aligned} \tau_g(t) &= \frac{-2\kappa}{\Gamma_0(\Gamma_0 + \kappa)} \\ \tau_g(r) &= \frac{2}{\Gamma_0 + \kappa} \end{aligned} \tag{A.16}$$

In the side-coupled configuration, the group delay is always of the same sign regardless of the coupling regime for both the transmission and reflection measurement.

An example of measurement in transmission of a hybrid nanobeam is shown in Fig.A.3. We do not see the dispersion of the waveguide here, and the coupling is not dispersive. We can see the transmission window of the grating that starts around 186 THz. The complex phase and amplitude spectrum are displayed in A.3b) and we see that the group delay is always negative. An example of fit with the zero/pole model is shown in A.3c), where the resonance frequency is identified at 190.5715 THz. The loss rates are $\kappa/2\pi = 7.5GHz$ and $\Gamma_0/2\pi = 5.8GHz$ ($Q_0 = 207000$ and $Q_c = 163000$). This cavity is slightly overcoupled, near the critical regime.

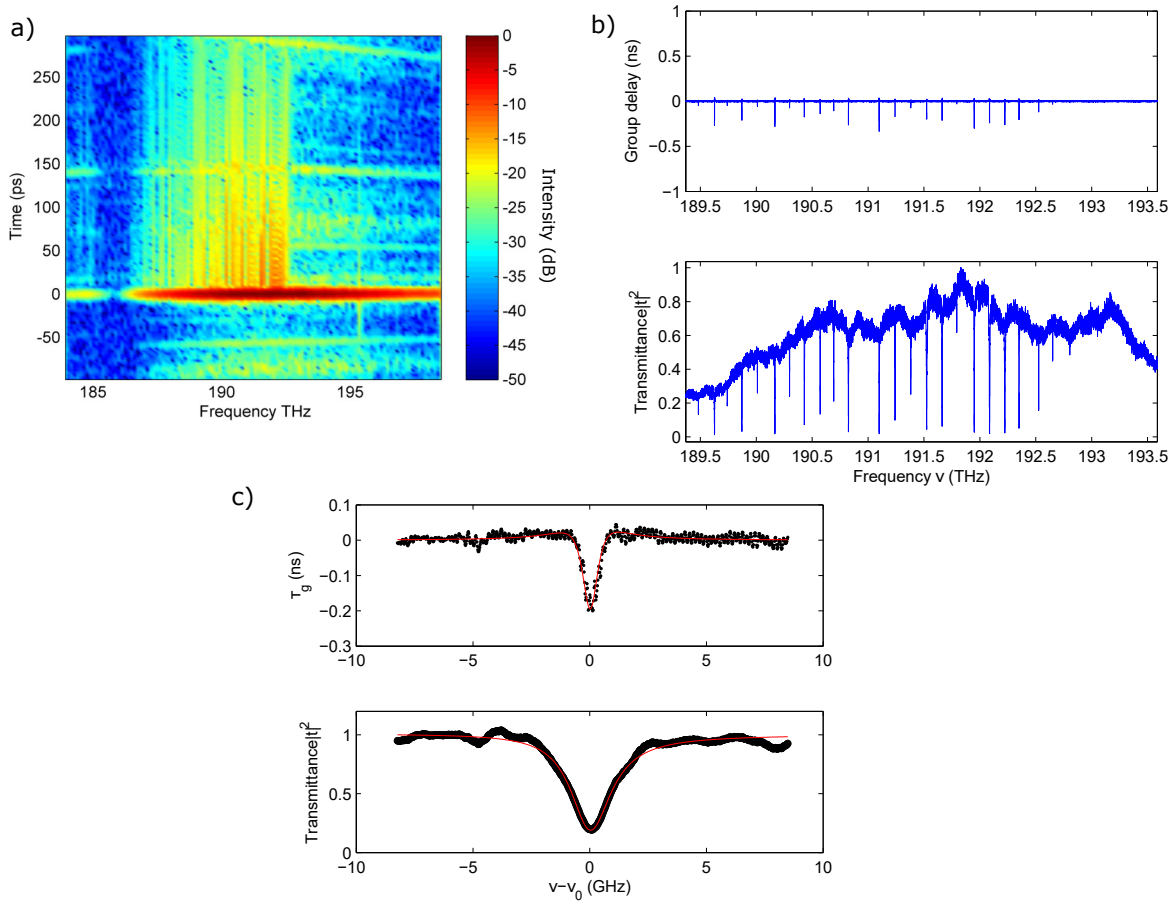

Figure A.3: a) Spectrogram of the transmitted signal of a 12 μm-FWHM nanobeam on a 550 nm-wide waveguide and b) the complex spectrum with the group delay and amplitude. c) Zero/pole model fit (red line) of the raw data (black dots) for a resonance measured at ν_0 =190.5715 THz, Q_0 = 207 000 and Q = 90 000

A.5 Precision of the frequency measurement

The relative and absolute precision of the measurement depends on several factors. First, the reference interferometer defines the spectral resolution because it is used as a trigger signal for sampling the main interferometer pattern. In our case, the spectral resolution is related to the count of fringes in the reference interferometer:

$$\delta\nu = \frac{c}{2n\delta} = 20MHz \tag{A.17}$$

where δ is the length of additional fiber in the unbalanced arm (δ = 5 m).
Fluctuations of the polarization may also occur. This is why the interference contrast is optimized by means of polarization controller before the measurement. As a temperature drift could also cause a change in the measurement, the sample is thermally controlled by a Peltier module. The sweeping speed of the laser is typically of 7 nm/s and a full range scan over 150 nm lasts 22 seconds. This measurement time is short enough to avoid the effects of a potential thermal drift.
The sampling resolution is the lower limit to the relative precision (laser frequency accuracy), which is the one important when measuring the dispersion of the cavity. However, the dispersion in the fibered reference arm induces a distortion in the frequency scale. Besides, the frequency axis is given by the laser setpoint which is accurate within 5 pm (600 MHz at telecom frequency). We can increase the absolute precision of the measurement with an very well known frequency reference. This is realized using a reference cyanide gas cell whose absorption lines are known with a 0.2 pm absolute accuracy (25 MHz at telecom frequency) as in Ref.[99]. The measured spectrum is shown in Fig.A.4a). This measure is repeated ten times, and the average error on the detected lines is shown in Fig.A.4b). We see a linear dependence that is likely to originate from the dispersion of the photonic components of the OCT. Thus, a linear interpolation can be used to redefine the frequency axis afterwards. We then verify the accuracy of our correction with a new measurement. It leads to a absolute error comprised between -50/+50 MHz, as can be seen in Fig.A.4c).

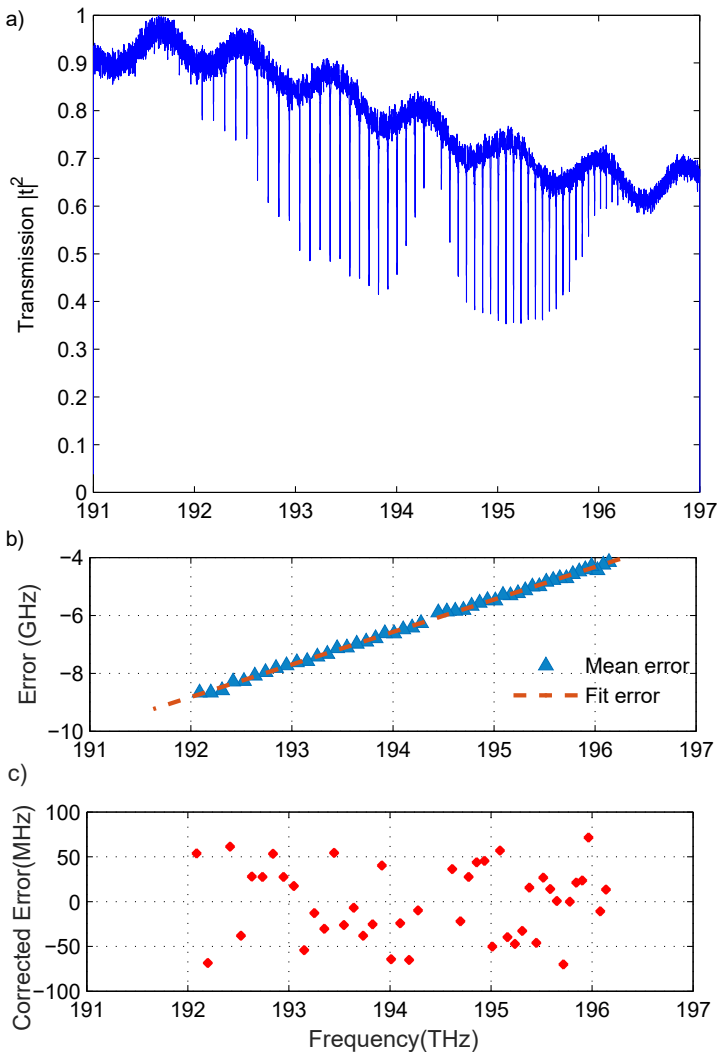

Figure A.4: a) Transmission spectrum of a cyanide reference cell b) Error between the absolute frequency and the average of 10 OCT measurements, fitted by a linear regression c) Residual error after correcting the frequency scale in the OCT measurements

Appendix B

Parameters used in the numerical simulations

parameter	units	cavity #27	cavity #18
$\omega_{-,cold}/2\pi$	THz	196.9989	193.1785
$\omega_{0,cold}/2\pi$	THz	197.3544	193.619
$\omega_{+,cold}/2\pi$	THz	197.6594	193.9916
$\Gamma_-/2\pi$	GHz	2.77	1.57
$\Gamma_0/2\pi$	GHz	2.95	2.13
$\Gamma_+/2\pi$	GHz	4.12	3.59
$\kappa_-/2\pi$	GHz	0.43	0.39
$\kappa_0/2\pi$	GHz	1.86	0.97
$\kappa_+/2\pi$	GHz	0.67	2.52
$\Delta\omega_{cold}/2\pi$	GHz	25.2	33.9
$\alpha_{0,-}/\alpha_{0,0}$		0.8972	0.991
$\alpha_{0,+}/\alpha_{0,0}$		0.6228	0.85
$\alpha_{0,0}$	$\mathrm{fJ}^{-1}\mathrm{GHz}$	-0.28	-0.32
symbol	units	value	reference
$\partial_T\omega/2\pi$	$\mathrm{GHz\ K}^{-1}$	-10.8	[120]
$\Gamma_{abs}/2\pi$	MHz	20	[144]
V_χ	μm^3	5.7	
V_m	μm^3	≈ 0.2	.
ε_r		≈ 10	
n_2	$10^{-18}m^2W^{-1}$	6	[11]
κ_{in}	dB	-7	

Table B.1: Numerical values for the parameters used in the model for Fig.4.6 and Fig.4.7. The linear and thermal properties have been directly measured, the others taken in the literature.

Bibliography

1. Maiman, T. H. Stimulated optical radiation in ruby. *Physical review letters* (1960).
2. Franken, e. P., Hill, A. E., Peters, C. & Weinreich, G. Generation of optical harmonics. *Physical Review Letters* **7,** 118 (1961).
3. Askaryan, G. A. Effect of the field gradient of an intense electromagnetic beam on electrons and atoms, 1567–1570 (Jan. 1991).
4. Hercher, M. Laser-induced damage in transparent media. *Journal of the Optical Society of America* (1964).
5. Giordmaine, J. A. & Miller, R. C. Tunable Coherent Parametric Oscillation in $LiNbO_3$ at Optical Frequencies. *Phys. Rev. Lett.* **14,** 973–976 (24 June 1965).
6. Stolen, R. & Bjorkholm, J. Parametric amplification and frequency conversion in optical fibers. *IEEE Journal of Quantum Electronics* **18,** 1062–1072 (1982).
7. O'brien, J. L., Furusawa, A. & Vučković, J. Photonic quantum technologies. *Nature Photonics* **3,** 687–695 (2009).
8. Boyd, R. W. *Nonlinear optics* (Academic press, 2019).
9. Ueno, Y., Ricci, V. & Stegeman, G. I. Second-order susceptibility of Ga 0.5 In 0.5 P crystals at 1.5 μm and their feasibility for waveguide quasi-phase matching. *JOSA B* **14,** 1428–1436 (1997).
10. Zanotti, S., Minkov, M., Fan, S., Andreani, L. C. & Gerace, D. Doubly-Resonant Photonic Crystal Cavities for Efficient Second-Harmonic Generation in III–V Semiconductors. *Nanomaterials* **11,** 605 (2021).
11. Husko, C. *et al.* Ultrafast all-optical modulation in GaAs photonic crystal cavities. *Applied Physics Letters* **94,** 021111 (2009).

12. Herr, T. *et al.* Temporal solitons in optical microresonators. *Nature Photonics* **8,** 145–152 (2014).

13. Ji, X. *et al.* Ultra-low-loss on-chip resonators with sub-milliwatt parametric oscillation threshold. *Optica* **4,** 619–624 (2017).

14. Xie, W. *et al. Ultrahigh-Q AlGaAs-on-insulator microresonators for integrated nonlinear photonics* 2020. arXiv: `2004.14537 [physics.optics]`.

15. Payne, F. & Lacey, J. A theoretical analysis of scattering loss from planar optical waveguides. *Optical and Quantum Electronics* **26,** 977–986 (1994).

16. Leuthold, J., Koos, C. & Freude, W. Nonlinear silicon photonics. *Nature photonics* **4,** 535–544 (2010).

17. Foster, M. A., Moll, K. D. & Gaeta, A. L. Optimal waveguide dimensions for nonlinear interactions. *Optics Express* **12,** 2880–2887 (2004).

18. Combrié, S., Tran, Q. V., De Rossi, A., Husko, C. & Colman, P. High quality GaInP nonlinear photonic crystals with minimized nonlinear absorption. *Applied Physics Letters* **95,** 221108 (2009).

19. Sheik-Bahae, M., Hagan, D. J. & Van Stryland, E. W. Dispersion and band-gap scaling of the electronic Kerr effect in solids associated with two-photon absorption. *Physical review letters* **65,** 96 (1990).

20. Koos, C., Jacome, L., Poulton, C., Leuthold, J. & Freude, W. Nonlinear silicon-on-insulator waveguides for all-optical signal processing. *Optics Express* **15,** 5976–5990 (2007).

21. Griffith, A. G. *et al.* Silicon-chip mid-infrared frequency comb generation. *Nature communications* **6,** 1–5 (2015).

22. Turner-Foster, A. C. *et al.* Ultrashort free-carrier lifetime in low-loss silicon nanowaveguides. *Optics express* **18,** 3582–3591 (2010).

23. Lenz, G. *et al.* Large Kerr effect in bulk Se-based chalcogenide glasses. *Optics Letters* **25,** 254–256 (2000).

24. Aitchison, J. S., Hutchings, D., Kang, J., Stegeman, G. & Villeneuve, A. The nonlinear optical properties of AlGaAs at the half band gap. *IEEE Journal of Quantum Electronics* **33,** 341–348 (1997).

25. Dave, U. D. *et al.* Nonlinear properties of dispersion engineered InGaP photonic wire waveguides in the telecommunication wavelength range. *Optics express* **23,** 4650–4657 (2015).

26. Dave, U. D. *et al.* Dispersive-wave-based octave-spanning supercontinuum generation in InGaP membrane waveguides on a silicon substrate. *Optics letters* **40,** 3584–3587 (2015).

27. Lalanne, P., Sauvan, C. & Hugonin, J. P. Photon confinement in photonic crystal nanocavities. *Laser & Photonics Reviews* **2,** 514–526 (2008).

28. Notomi, M. Manipulating light with strongly modulated photonic crystals. *Reports on Progress in Physics* **73,** 096501 (2010).

29. Kristensen, P. T., Van Vlack, C. & Hughes, S. Generalized effective mode volume for leaky optical cavities. *Optics letters* **37,** 1649–1651 (2012).

30. Sauvan, C., Hugonin, J.-P., Maksymov, I. & Lalanne, P. Theory of the spontaneous optical emission of nanosize photonic and plasmon resonators. *Physical Review Letters* **110,** 237401 (2013).

31. Agrawal, G. P. *Nonlinear fiber optics* 195–211 (Springer, 2000).

32. Pu, M. *et al.* Ultra-Efficient and Broadband Nonlinear AlGaAs-on-Insulator Chip for Low-Power Optical Signal Processing. *Laser & Photonics Reviews* **12,** 1800111 (2018).

33. Absil, P. *et al.* Wavelength conversion in GaAs micro-ring resonators. *Optics letters* **25,** 554–556 (2000).

34. Pu, M., Ottaviano, L., Semenova, E. & Yvind, K. Efficient frequency comb generation in AlGaAs-on-insulator. *Optica* **3,** 823–826 (2016).

35. Chang, L. *et al.* Ultra-efficient frequency comb generation in AlGaAs-on-insulator microresonators. *Nature communications* **11,** 1–8 (2020).

36. Wilson, D. J. *et al.* Integrated gallium phosphide nonlinear photonics. *Nature Photonics,* 1–6 (2019).

37. Bruch, A. W., Liu, X., Surya, J. B., Zou, C.-L. & Tang, H. X. On-chip $\chi^{(2)}$ microring optical parametric oscillator. *Optica* **6,** 1361–1366 (2019).

38. Liu, X. *et al.* Integrated high-Q crystalline AlN microresonators for broadband Kerr and Raman frequency combs. *ACS Photonics* **5,** 1943–1950 (2018).

39. Hausmann, B., Bulu, I., Venkataraman, V., Deotare, P. & Lončar, M. Diamond nonlinear photonics. *Nature Photonics* **8,** 369 (2014).

40. Suh, M.-G. & Vahala, K. Gigahertz-repetition-rate soliton microcombs. *Optica* **5,** 65–66 (2018).

41. Guidry, M. A. *et al.* Optical parametric oscillation in silicon carbide nanophotonics. *arXiv preprint arXiv:2004.13958* (2020).

42. He, Y. *et al.* Self-starting bi-chromatic LiNbO 3 soliton microcomb. *Optica* **6,** 1138–1144 (2019).

43. Razzari, L. *et al.* CMOS-compatible integrated optical hyper-parametric oscillator. *Nature Photonics* **4,** 41–45 (2010).

44. Kippenberg, T., Spillane, S. & Vahala, K. Kerr-nonlinearity optical parametric oscillation in an ultrahigh-Q toroid microcavity. *Physical review letters* **93,** 083904 (2004).

45. Savchenkov, A. A. *et al.* Low Threshold Optical Oscillations in a Whispering Gallery Mode C a F 2 Resonator. *Physical review letters* **93,** 243905 (2004).

46. Del'Haye, P. *et al.* Optical frequency comb generation from a monolithic microresonator. *Nature* **450,** 1214–1217 (2007).

47. Savchenkov, A., Matsko, A. & Maleki, L. On frequency combs in monolithic resonators. *Nanophotonics* **5,** 363–391 (2016).

48. Braje, D. A. Tiny resonators generate a large optical spectrum. *Physics* **3,** 75 (2010).

49. Bogaerts, W. *et al.* Silicon microring resonators. *Laser & Photonics Reviews* **6,** 47–73 (2012).

50. Yang, K. Y. *et al.* Bridging ultrahigh-Q devices and photonic circuits. *Nature Photonics* **12,** 297–302 (2018).

51. Levy, J. S. *et al.* CMOS-compatible multiple-wavelength oscillator for on-chip optical interconnects. *Nature photonics* **4,** 37–40 (2010).

52. Shaw, M. J., Guo, J., Vawter, G. A., Habermehl, S. & Sullivan, C. T. *Fabrication techniques for low-loss silicon nitride waveguides* in *Micromachining Technology for Micro-Optics and Nano-Optics III* **5720** (2005), 109–118.

53. Helt, L. G., Liscidini, M. & Sipe, J. E. How does it scale? Comparing quantum and classical nonlinear optical processes in integrated devices. *JOSA B* **29,** 2199–2212 (2012).

54. Xu, Q., Fattal, D. & Beausoleil, R. G. Silicon microring resonators with 1.5-μm radius. *Optics express* **16,** 4309–4315 (2008).

55. Yablonovitch, E. Inhibited spontaneous emission in solid-state physics and electronics. *Physical review letters* **58,** 2059 (1987).

56. John, S. Strong localization of photons in certain disordered dielectric superlattices. *Physical review letters* **58,** 2486 (1987).

57. Cheng, C.-C. & Scherer, A. Fabrication of photonic band-gap crystals. *Journal of Vacuum Science & Technology B: Microelectronics and Nanometer Structures Processing, Measurement, and Phenomena* **13,** 2696–2700 (1995).

58. Krauss, T. F., Richard, M. & Brand, S. Two-dimensional photonic-bandgap structures operating at near-infrared wavelengths. *Nature* **383,** 699–702 (1996).

59. Crosnier, G. *et al.* Hybrid indium phosphide-on-silicon nanolaser diode. *Nature Photonics* **11,** 297 (2017).

60. Gavartin, E. *et al.* Optomechanical Coupling in a Two-Dimensional Photonic Crystal Defect Cavity. *Phys. Rev. Lett.* **106,** 203902 (20 2011).

61. Sakoda, K. *Optical properties of photonic crystals* (Springer Science & Business Media, 2004).

62. Joannopoulos, J. D., Johnson, S. G., Winn, J. N. & Meade, R. D. *Photonic Crystals: Molding the Flow of Light (Second Edition)* 2nd ed. ISBN: 0691124566 (Princeton University Press, 2008).

63. Yablonovitch, E., Gmitter, T. & Leung, K.-M. Photonic band structure: The face-centered-cubic case employing nonspherical atoms. *Physical review letters* **67,** 2295 (1991).

64. Velha, P. *et al.* Ultra-high Q/V Fabry-Perot microcavity on SOI substrate. *Optics express* **15,** 16090–16096 (2007).

65. Akahane, Y., Asano, T., Song, B.-S. & Noda, S. High-Q photonic nanocavity in a two-dimensional photonic crystal. *nature* **425,** 944–947 (2003).

66. Song, B.-S., Noda, S., Asano, T. & Akahane, Y. Ultra-high-Q photonic double-heterostructure nanocavity. *Nature materials* **4,** 207–210 (2005).

67. Kuramochi, E. *et al.* Ultrahigh-Q photonic crystal nanocavities realized by the local width modulation of a line defect. *Applied physics letters* **88,** 041112 (2006).

68. Deotare, P. B., McCutcheon, M. W., Frank, I. W., Khan, M. & Lončar, M. High quality factor photonic crystal nanobeam cavities. *Applied Physics Letters* **94,** 121106 (2009).

69. Tran, Q. V., Combrié, S., Colman, P. & De Rossi, A. Photonic crystal membrane waveguides with low insertion losses. *Applied Physics Letters* **95,** 061105 (2009).

70. Baba, T. Slow light in photonic crystals. *Nature photonics* **2,** 465–473 (2008).

71. Hamachi, Y., Kubo, S. & Baba, T. Slow light with low dispersion and nonlinear enhancement in a lattice-shifted photonic crystal waveguide. *Optics letters* **34,** 1072–1074 (2009).

72. Martin, A., Sanchez, D., Combrié, S., De Rossi, A. & Raineri, F. GaInP on oxide nonlinear photonic crystal technology. *Optics Letters* **42,** 599–602 (2017).

73. Yablonovitch, E. *et al.* Donor and acceptor modes in photonic band structure. *Physical Review Letters* **67,** 3380 (1991).

74. Foresi, J. *et al.* Photonic-bandgap microcavities in optical waveguides. *nature* **390,** 143–145 (1997).

75. Sauvan, C., Lalanne, P. & Hugonin, J.-P. Slow-wave effect and mode-profile matching in photonic crystal microcavities. *Physical Review B* **71,** 165118 (2005).

76. Sauvan, C., Lecamp, G., Lalanne, P. & Hugonin, J.-P. Modal-reflectivity enhancement by geometry tuning in photonic crystal microcavities. *Optics Express* **13,** 245–255 (2005).

77. Asano, T., Ochi, Y., Takahashi, Y., Kishimoto, K. & Noda, S. Photonic crystal nanocavity with a Q factor exceeding eleven million. *Optics Express* **25,** 1769 (2017).

78. Li, M. *et al.* Photon-level tuning of photonic nanocavities. *Optica* **6,** 860–863 (2019).

79. Takahashi, Y. *et al.* A micrometre-scale Raman silicon laser with a microwatt threshold. *Nature* **498,** 470–474 (2013).

80. Rivoire, K., Lin, Z., Hatami, F., Masselink, W. T. & Vučković, J. Second harmonic generation in gallium phosphide photonic crystal nanocavities with ultralow continuous wave pump power. *Optics express* **17,** 22609–22615 (2009).

81. Rivoire, K., Lin, Z., Hatami, F. & Vučković, J. Sum-frequency generation in doubly resonant GaP photonic crystal nanocavities. *Applied Physics Letters* **97,** 043103 (2010).

82. Buckley, S. *et al.* Nonlinear frequency conversion using high-quality modes in GaAs nanobeam cavities. *Optics letters* **39,** 5673–5676 (2014).

83. Buckley, S. *et al.* Second-harmonic generation in GaAs photonic crystal cavities in (111) B and (001) crystal orientations. *ACS Photonics* **1,** 516–523 (2014).

84. Mohamed, M. S. *et al.* Efficient continuous-wave nonlinear frequency conversion in high-Q gallium nitride photonic crystal cavities on silicon. *APL Photonics* **2,** 031301 (2017).

85. Galli, M. *et al.* Low-power continuous-wave generation of visible harmonics in silicon photonic crystal nanocavities. *Optics express* **18,** 26613–26624 (2010).

86. Jiang, H. *et al.* Nonlinear frequency conversion in one dimensional lithium niobate photonic crystal nanocavities. *Applied Physics Letters* **113,** 021104 (2018).

87. Yamada, S. *et al.* Second-harmonic generation in a silicon-carbide-based photonic crystal nanocavity. *Optics letters* **39,** 1768–1771 (2014).

88. Song, B.-S. *et al.* Ultrahigh-Q photonic crystal nanocavities based on 4H silicon carbide. *Optica* **6,** 991–995 (2019).

89. Clementi, M. *et al.* Cavity-enhanced harmonic generation in silicon rich nitride photonic crystal microresonators. *Applied Physics Letters* **114,** 131103 (2019).

90. Azzini, S. *et al.* Stimulated and spontaneous four-wave mixing in silicon-on-insulator coupled photonic wire nano-cavities. *Applied Physics Letters* **103,** 031117 (2013).

91. Matsuda, N. *et al.* Slow light enhanced optical nonlinearity in a silicon photonic crystal coupled-resonator optical waveguide. *Optics express* **19,** 19861–19874 (2011).

92. Martin, A. *et al.* Triply-resonant Continuous Wave Parametric Source with a Microwatt Pump. *arXiv preprint arXiv:1602.04833* (2016).

93. Kuramochi, E. *et al.* Disorder-induced scattering loss of line-defect waveguides in photonic crystal slabs. *Physical Review B* **72,** 161318 (2005).

94. Gerace, D. & Andreani, L. C. Effects of disorder on propagation losses and cavity Q-factors in photonic crystal slabs. *Photonics and Nanostructures-fundamentals and applications* **3,** 120–128 (2005).

95. Hagino, H., Takahashi, Y., Tanaka, Y., Asano, T. & Noda, S. Effects of fluctuation in air hole radii and positions on optical characteristics in photonic crystal heterostructure nanocavities. *Physical Review B* **79,** 085112 (2009).

96. Taguchi, Y., Takahashi, Y., Sato, Y., Asano, T. & Noda, S. Statistical studies of photonic heterostructure nanocavities with an average Q factor of three million. *Optics express* **19,** 11916–11921 (2011).

97. Kurihara, J. *et al.* Detrimental fluctuation of frequency spacing between the two high-quality resonant modes in a Raman silicon nanocavity laser. *IEEE Journal of Selected Topics in Quantum Electronics* **26,** 1–12 (2019).

98. Sokolov, S. *et al.* Local thermal resonance control of GaInP photonic crystal membrane cavities using ambient gas cooling. *Applied physics letters* **106,** 171113 (2015).

99. Sokolov, S. *et al.* Tuning out disorder-induced localization in nanophotonic cavity arrays. *Optics express* **25,** 4598–4606 (2017).

100. Conti, C., Di Falco, A. & Assanto, G. Optical parametric oscillations in isotropic photonic crystals. *Optics express* **12,** 823–828 (2004).

101. Ramirez, D. M. *et al.* Degenerate four-wave mixing in triply resonant Kerr cavities. *Physical Review A* **83** (2011).

102. Haus, H. A. *Waves and fields in optoelectronics* (Prentice-Hall, 1984).

103. Haus, H. A. & Huang, W. Coupled-mode theory. *Proceedings of the IEEE* **79,** 1505–1518. ISSN: 1558-2256 (Oct. 1991).

104. Suh, W., Wang, Z. & Fan, S. Temporal coupled-mode theory and the presence of non-orthogonal modes in lossless multimode cavities. *IEEE Journal of Quantum Electronics* **40,** 1511–1518 (2004).

105. Kristensen, P. T. & Hughes, S. Modes and mode volumes of leaky optical cavities and plasmonic nanoresonators. *ACS Photonics* **1,** 2–10 (2014).

106. Lin, Z., Alcorn, T., Loncar, M., Johnson, S. G. & Rodriguez, A. W. High-efficiency degenerate four-wave mixing in triply resonant nanobeam cavities. *Physical Review A* **89,** 053839 (2014).

107. Helt, L. G., Liscidini, M. & Sipe, J. E. How does it scale? Comparing quantum and classical nonlinear optical processes in integrated devices. *JOSA B* **29,** 2199–2212 (2012).

108. Chembo, Y. K. Quantum dynamics of Kerr optical frequency combs below and above threshold: Spontaneous four-wave mixing, entanglement, and squeezed states of light. *Physical Review A* **93,** 033820 (2016).

109. Moille, G., Combrié, S. & De Rossi, A. Modeling of the carrier dynamics in nonlinear semiconductor nanoscale resonators. *Physical Review A* **94,** 023814 (2016).

110. Palamaru, M. & Lalanne, P. Photonic crystal waveguides: Out-of-plane losses and adiabatic modal conversion. *Applied Physics Letters* **78,** 1466–1468 (2001).

111. Peyrade, D., Silberstein, E., Lalanne, P., Talneau, A. & Chen, Y. Short Bragg mirrors with adiabatic modal conversion. *Applied Physics Letters* **81,** 829–831 (2002).

112. Sauvan, C., Lalanne, P. & Hugonin, J.-P. Tuning holes in photonic-crystal nanocavities. *Nature* **429,** 1–1 (2004).

113. Alpeggiani, F., Andreani, L. C. & Gerace, D. Effective bichromatic potential for ultra-high Q-factor photonic crystal slab cavities. *Applied Physics Letters* **107,** 261110 (2015).

114. Roati, G. *et al.* Anderson localization of a non-interacting Bose–Einstein condensate. *Nature* **453,** 895–898 (2008).

115. Simbula, A. *et al.* Realization of high-Q/V photonic crystal cavities defined by an effective Aubry-André-Harper bichromatic potential. *APL Photonics* **2,** 056102 (2017).

116. Sipe, J. E. & Winful, H. G. Nonlinear Schrödinger solitons in a periodic structure. *Optics letters* **13,** 132–133 (1988).

117. Sumetsky, M. & Fini, J. Surface nanoscale axial photonics. *Optics express* **19,** 26470–26485 (2011).

118. Oreshnikov, I. & Skryabin, D. Multiple nonlinear resonances and frequency combs in bottle microresonators. *Optics express* **25,** 10306–10311 (2017).

119. Dobbelaar, M., Greveling, S. & van Oosten, D. Large area photonic crystal cavities: a local density approach. *Optics express* **23,** 7481–7499 (2015).

120. Combrié, S., Lehoucq, G., Moille, G., Martin, A. & De Rossi, A. Comb of high-Q Resonances in a Compact Photonic Cavity. *Laser & Photonics Reviews* **11,** 1700099 (2017).

121. Martin, A., Combrié, S., Willinger, A., Eisenstein, G. & de Rossi, A. Interplay of phase-sensitive amplification and cascaded four-wave mixing in dispersion-controlled waveguides. *Physical Review A* **94,** 023817 (2016).

122. Bazin, A., Raj, R. & Raineri, F. Design of silica encapsulated high-Q photonic crystal nanobeam cavity. *Journal of Lightwave Technology* **32,** 952–958 (2014).

123. Crosnier, G. *et al.* High Q factor InP photonic crystal nanobeam cavities on silicon wire waveguides. *Optics letters* **41,** 579–582 (2016).

124. Halioua, Y. *et al.* Hybrid III-V semiconductor/silicon nanolaser. *Optics express* **19,** 9221–9231 (2011).

125. Il'chenko, V. S. & Gorodetskii, M. L. Thermal Nonlinear Effects in Optical Whispering Gallery Microresonators. *Laser Physics* **2,** 1004–1009 (1992).

126. Carmon, T., Yang, L. & Vahala, K. J. Dynamical thermal behavior and thermal self-stability of microcavities. *Optics express* **12,** 4742–4750 (2004).

127. Mosor, S. *et al.* Scanning a photonic crystal slab nanocavity by condensation of xenon. *Applied Physics Letters* **87,** 141105 (2005).

128. Hennessy, K. *et al.* Tuning photonic crystal nanocavity modes by wet chemical digital etching. *Applied Physics Letters* **87,** 021108 (2005).

129. Laucht, A. *et al.* Electrical control of spontaneous emission and strong coupling for a single quantum dot. *New Journal of Physics* **11,** 023034 (2009).

130. Faraon, A. & Vučković, J. Local temperature control of photonic crystal devices via micron-scale electrical heaters. *Applied Physics Letters* **95,** 043102 (2009).

131. Yüce, E. *et al.* Adaptive control of necklace states in a photonic crystal waveguide. *ACS photonics* **5,** 3984–3988 (2018).

132. Joshi, C. *et al.* Thermally controlled comb generation and soliton modelocking in microresonators. *Optics letters* **41,** 2565–2568 (2016).

133. Husko, C. *et al.* Non-trivial scaling of self-phase modulation and three-photon absorption in III–V photonic crystal waveguides. *Optics express* **17,** 22442–22451 (2009).

134. Liscidini, M. & Sipe, J. Stimulated emission tomography. *Physical review letters* **111,** 193602 (2013).

135. Bazin, A. *et al.* Thermal management in hybrid InP/silicon photonic crystal nanobeam laser. *Optics express* **22,** 10570–10578 (2014).

136. Ferrera, M. *et al.* Low power four wave mixing in an integrated, micro-ring resonator with Q= 1.2 million. *Optics express* **17,** 14098–14103 (2009).

137. Ji, M. *et al.* Enhanced parametric frequency conversion in a compact silicon-graphene microring resonator. *Optics express* **23,** 18679–18685 (2015).

138. Ong, J., Kumar, R. & Mookherjea, S. Triply resonant four-wave mixing in silicon-coupled resonator microring waveguides. *Optics letters* **39,** 5653–5656 (2014).

139. Fürst, J. *et al.* Low-threshold optical parametric oscillations in a whispering gallery mode resonator. *Physical Review Letters* **105,** 263904 (2010).

140. Marchetti, R. *et al.* High-efficiency grating-couplers: demonstration of a new design strategy. *Scientific reports* **7,** 16670 (2017).

141. Lian, J. *et al.* Dispersion of coupled mode-gap cavities. *Optics letters* **40,** 4488–4491 (2015).

142. Gottesman, Y. *et al.* Time-frequency analysis for an efficient detection and localization of side-coupled cavities in real photonic crystals. *Journal of Lightwave Technology* **28,** 816–821 (2010).

143. Parini, A. *et al.* Time-wavelength reflectance maps of photonic crystal waveguides: a new view on disorder-induced scattering. *Journal of lightwave technology* **26,** 3794–3802 (2008).

144. Ghorbel, I. *et al.* Optomechanical gigahertz oscillator made of a two photon absorption free piezoelectric III/V semiconductor. *APL Photonics* **4,** 116103 (2019).

université PARIS-SACLAY | ÉCOLE DOCTORALE Ondes et Matière (EDOM)

Titre: Mélange à quatre ondes dans des cavités à cristaux photoniques en semiconducteur III-V

Mots clés: Cristaux Photoniques, Semiconducteurs à grand gap, Optique non linéaire, Mélange à quatre ondes, Oscillateur Paramétrique

Résumé: Un traitement tout optique du signal pourrait réduire considérablement la consommation d'énergie et augmenter le débit de données par rapport à son analogue électronique. Cette approche nécessite l'intégration de multiples systèmes photoniques sur une puce. Les composants qui exploitent les interactions paramétriques peuvent réaliser différentes fonctions comme la conversion de longueur d'onde, l'amplification, l'échantillonnage et la commutation. Les micro-résonateurs non-linéaires sont intéressants car ils permettent la réduction de l'empreinte sur puce du composant et de la puissance nécessaire pour activer les effets non-linéaires. Parmi eux, les cavités à cristaux photoniques (PhC) paraissent être particulièrement prometteuses du fait de leur capacité à confiner la lumière dans un volume proche celui permis par la limite de diffraction. Pourtant, la difficulté de contrôler la dispersion de leurs modes résonants explique que les efficacités non-linéaires observées sont restées bien inférieures aux maxima théoriques prévus pour ces structures. Partant des travaux réalisés précédemment au sein de l'équipe de recherche, l'objectif de ce travail de thèse consiste à exploiter pleinement le potentiel des cavités PhC non-linéaires. Les cavités étudiées dans ce travail ont été conçues pour générer un potentiel parabolique pour les photons afin d'obtenir des modes résonants équispacés en fréquence, pour convenir à la règle de conservation de l'énergie requise pour les interactions paramétriques. Cependant, la caractérisation linéaire des résonateurs montre que le désordre structurel induit une déviation par rapport aux fréquences visées qui nécessite une technique de compensation. Pour résoudre ce problème, un procédé d'ajustement thermique qui exploite la répartition inhomogène de la distribution spatiale des modes électromagnétiques est introduit. Il permet de mettre de façon systématique la cavité en configuration triplement résonnante. Ce procédé d'ajustement est employé pour observer du mélange à quatre ondes stimulé et spontané avec des efficacités record. L'oscillation paramétrique dans une cavité PhC est démontrée pour la première fois dans un échantillon avec des facteurs de qualité plus élevés. Une seconde plateforme est développée, basée sur l'intégration hybride d'une cavité PhC sur un circuit en silicium, avec une empreinte sur puce réduite et une excellente capacité d'intégration. Un mélange à quatre ondes efficace est encore une fois observé en utilisant le même procédé d'ajustement que précédemment.

Title: Four Wave Mixing in III-V semiconductor Photonic Crystal Cavities

Keywords: Photonic Crystals, Wide Gap Semiconductors, Nonlinear Optics, Four Wave Mixing, Parametric Oscillator

Abstract: All optical signal processing could drastically reduce the power consumption and increase the data rates allowed by its electronic counterpart. This approach requires the integration of multiple photonics systems on a chip. Components exploiting parametric interactions can perform various tasks such as wavelength conversion, amplification, sampling and switching. Nonlinear micro-resonators are attractive in order to reduce the footprint of the component and the power required to activate the nonlinear effects. Photonic crystals (PhC) cavities seem to provide a very interesting platform due to their ability to strongly confine light in a close to diffraction-limited volume. However, due to the difficulty to engineer the dispersion of the photonic crystal cavity modes, the nonlinear efficiencies have remained well below the theoretical maximum allowed by these structures. Based on the previous work realized by the research group, the aim of this thesis is to harness the potential of nonlinear PhC cavities. The cavities studied in this work are by design the optical analogous of the quantum harmonic oscillator. When the photons are submitted to a parabolic electromagnetic potential, the modes of the cavity are equally spaced in frequency, which matches the energy conservation requirement for parametric interactions. However, the linear characterization of these resonators shows that the structural disorder induces a deviation on the targeted frequency that requires a compensation technique. To tackle this issue, a thermal tuning process that exploits the inhomogeneous spatial distribution of the electromagnetic modes is introduced. It allows to systematically put the cavity in a triply resonant configuration. This tuning technique is used to observe stimulated and spontaneous four wave mixing with record efficiency. Parametric oscillation in a PhC cavity is demonstrated for the first time in a sample with higher quality factors. A second platform is also developed, based on the hybrid integration of a PhC cavity on a silicon circuitry, with a very low footprint and high integration capability. Efficient four wave mixing is again observed using the same tuning technique.

Université Paris-Saclay
Espace Technologique / Immeuble Discovery
Route de l'Orme aux Merisiers RD 128 / 91190